MICROSTRUCTURAL AND MECHANICAL INTEGRITY OF 3D PRINTED 316L STAINLESS STEEL

ALI ELIASU

A THESIS SUBMITTED TO THE FACULTY OF GRADUATE STUDIES IN PARTIAL FULFILLMENT OF THE REQUIREMENTS FOR THE DEGREE OF MASTER OF APPLIED SCIENCE

GRADUATE PROGRAM IN MECHANICAL ENGINEERING

YORK UNIVERSITY

TORONTO, ONTARIO

December 2019

ABSTRACT

Hindrance to the advancement of materials processing and components using metal-based additive manufacturing is a result of numerous challenges due to the complex mechanisms that occur such as multiple modes of heat, mass, and momentum transfers induced by localized laser scanning. This results in processing defects such as gas entrapment, unmelted and over-melted powders, aggregation of constituent phases and microcracks that affect the integrity of the printed parts. To avoid defects/flaws in parts and establish relationships between process parameters and part quality, it is critical to understanding the effect of processing parameters on the evolution of microstructural heterogeneities which influence the properties and quality of parts fabricated via AM. In this study, the effect of DMLS parameters on part quality and microstructural evolution is studied as a baseline for tailoring the microstructure of parts for a specific application. Various printing parameters are combined to create fifteen samples, which are then studied extensively to find parameters that create good microstructure and mechanical behavior. It was observed that during the processing of 316L stainless steel using Direct Metal Laser Sintering (DMLS), parts with good microstructural integrity as well as high performance were obtained when Volumetric Energy Densities (VEDs) between 45 and 110 J/mm^3 are used. The volume fraction of surface porosities, unmelted powders, over-melted regions and consequently part quality and performance were compromised when VEDs below this range were chosen but above the range, more gas pores are introduced into the sample. The range above the suitable can be used for the part required in biomedical application, components for heat exchangers or parts placed in front of car bumpers for energy absorption. For structural application, the total elimination of pores is required hence using a higher laser power in combination with large hatch spacing, or a combination of low power with a small hatch spacing is going to yield a better microstructure. The scan speed is the most sensitive parameter of the three individual parameters even though how sensitive the scan speed depends on the other parameters. The evolution of microstructure features is also very dependent on the printing parameters. Within the range of acceptable VEDs that produced parts with good microstructural integrity and performance, it was observed that the laser power, scanning speed and hatch spacing had a significant effect on the evolution of columnar and cellular sub-grain structures. Increasing the laser power and scan speeds resulted in thicker and well-defined cellular and columnar subgrains with relatively lower hardness while an increase in hatch spacing leads to less developed substructures. Laser power, scan speed, and hatch spacing also affect the wear resistance of the sample. Increasing power improves the wear behavior of the

sample if the hatch spacing of 100 µm and above but tends to reduce the wear performance if using small hatch spacing. Thus, samples within the acceptable range also exhibit better mechanical properties in terms of higher hardness values and good wear properties. These mechanical properties are compromised when the heat accumulation in the sample during fabrication is very high.

ACKNOWLEDGMENTS

My sincere thanks go firstly to my Professor and advisor, Solomon Boakye-Yiadom for the rare opportunity to be part of his research team. His constant guidance and never-ending support helped me through this research. I am equally grateful to Professor Alex Czekanski for his enormous contribution towards this research and the opportunity to be part of the IDEA lab as well. I am also grateful to the Natural Sciences and Engineering Research Council of Canada (NSERC) for the financial support they provided to the lab. I would like to also extend my thanks to the Mechanical Department at The Lassonde School of Engineering for providing the facilities and numerous financial assistance, especially the York Graduate Fellowship, to help me complete this research. The success in this research is also partly due to the help from my colleagues in the MTAM lab who provided various assistance including advice during my work. I am very lucky to find myself part of two great labs in the Mechanical Engineering Department. My gratitude also goes to the lab technicians, David Marcinkiewicz, Calvin Pettinger and Adams Mclean from the department of mechanical engineering and James Freemantle from the department of Earth Science who saw me through several extensive training sessions and their added support during my experimentations. I would like to thank the whole student body of the Mechanical Graduate Student Association of York University for the various encouragement and help when I needed it to see me through to the end of this work. Finally, my sincere thanks go to Sylvia Boakye-Yiadom, Nana Kwame Boakye Yiadom, James Agyemang, James and Evelyn Osei, Robert Kowfie for their utmost support through my entire stay in Canada. I am grateful to my family who continues to show their unwavering support all the way back home

To God be the Glory.

CONTENTS

ABSTRACT....ii
ACKNOWLEDGMENTS....iv
CONTENTS....v
LIST OF TABLES....vii
LIST OF FIGURES....viii
LIST OF ABBREVIATIONS....xi
1 INTRODUCTION....1
1.1 Background....1
1.2 Problem Statement and Research Objectives....1
1.3 Research Methodology....3
1.4 Summary of Findings....4
1.5 Thesis Organization....5
2 LITERATURE REVIEW....7
2.1 Metal-Additive Manufacturing....7
2.2 Types of Metal-Additive Manufacturing....7
2.2.1 Powder Bed Fusion (PBF)....8
2.2.2 Direct Energy Deposition (DED)....10
2.2.3 Binder Jetting....12
2.2.4 Sheet Lamination....13
2.3 Advantages and Applications of Metal-Additive Manufacturing....15
2.3.1 Intricate and light-weight part fabrication....16
2.3.2 Defense applications....17
2.3.3 Medical Applications....19
2.3.4 Prototyping and research purposes....20
2.4 Challenges of Metal-Additive Manufacturing....20
2.4.1 Printing Parameters....20
2.4.2 Porosities....22
2.4.3 Residual Stresses....24
2.4.4 Non-equilibrium Microstructures....24
2.5 316L Stainless Steel Alloy....28
2.1 Printing Parameters effect on Laser Sintered 316L Microstructure....29
2.2 Mechanical Properties of 3D Printed 316L Steel....31
2.2.1 Hardness....31
2.2.2 Tribological Behaviour of 316L Stainless Steel Alloy....32

2.2.3 Friction and Coefficient of friction 32
2.2.4 Wear 33
2.2.5 Wear Mechanisms 33
3 METHODOLOGY 36
3.1 Introduction 36
3.2 Sample Processing 37
3.3 Surface Preparation and Microstructural Characterization 39
3.4 Determining the Surface Porosities and Density 42
3.1 Hardness Testing 44
3.2 Roughness Measurement 45
3.3 Wear Testing 46
4 RESULTS 48
4.1 Effect of Printing Parameters on Surface Porosities 48
4.1.1 Effect of Parameters on Pore Size and Distribution 54
4.1.2 Parameter Sensitivity on Porosity 58
4.2 Effect of Printing Parameters on Part Density 62
4.3 Effect of Printing Parameters on The Hardness and Evolved Microstructure of the Printed Samples 63
4.4 Surface Roughness and Wear Rate 70
4.4.1 Influence of Printing Parameters on Wear 72
5 DISCUSSION 76
6 CONCLUSION AND FUTURE WORK 80
6.1 Summary and Conclusion 80
6.2 Future Work 81
7 REFERENCES 82
RESEARCH CONTRIBUTIONS 91
8 APPENDIX A- Coefficient of friction 92
9 APPENDIX B- Raw data 95
10 APPENDIX C-Chemical Analysis 96
11 APPENDIX D- Scan Pattern 97

LIST OF TABLES

Table 2-1: Printing parameter combinations for getting optimized parameters for printing [52] 21
Table 2-2: Various MAM techniques and the different kinds of phases it induces in the final parts made of Iron Alloys [5].....26
Table 2-3: Chemical Composition of 326L Stainless Steel Powder from EOS 28
Table 3-1: Printing parameters for AISI 316L Alloy.....38
Table 4-1: Porosity level from Image processing (ImageJ).....49
Table 4-2: Micro-hardness measurements of samples.....63
Table 4-3: Roughness of samples prior to Wear Testing.....71
Table 4-4: Wear results data 75

LIST OF FIGURES

Figure 2-1: Schematic of the Laser Powder Bed Fusion process [28].....9
Figure 2-2: Schematic of Electron beam Melting Technology [29].....10
Figure 2-3: Schematic of a wire DED technology [23].....11
Figure 2-4: Schematic of Power Bed DED [24].....11
Figure 2-5: Schematic of LENS technology[38].....12
Figure 2-6: Schematic of Binder Jetting [29].....13
Figure 2-7: Steps involved in brazing sheet metals together [24].....14
Figure 2-8: Schematic of UAM Sheet Lamination technique [24].....15
Figure 2-9: Airfoil with embedded cooling channels[1].....16
Figure 2-10: Lightweight applications of MAM a) GE fuel nozzle tip b)bracket for Airbus 350 [28].....17
Figure 2-11: a)Turbine blade with cooling channels b) Bell rotorcraft mixing nozzle made by EBM[1].....18
Figure 2-12: Hip stems designed with controlled porosities using a)EBM b)LENS[1].....19
Figure 2-13: Lack of fusion pores a)at low magnification b)at high magnification revealing unmelted powders[30].....23
Figure 2-14: Spherical gas pore in a) 316L-SLM part[55] Ti-6Al-4V-EBM part[35].....23
Figure 2-15 Cracking between layers in M2 Tool Steel[62].....24
Figure 2-16: Microstructure of 316L Steel fabricated with DED showing cellular dendritic structures[5].....26
Figure 2-17: Presence of ferrite in Austenitic Stainless Steel produced with LENS (316L)[38].....27
Figure 2-18: Sigma and delta ferrite in 316L produced with Arc AM[74].....27
Figure 2-19: Schematic representation of the Vickers hardness process.....31
Figure 2-20: Schematic of friction on a sliding body.....32
Figure 2-21: Schematic representation of wear mechanisms (a) adhesive (b) abrasive (c) fatigue wear (d) corrosive wear[95].....34
Figure 3-1: Microstructural Analysis of 3D-printed Samples.....36
Figure 3-2: Mechanical Behaviour Testing of 3D printed Samples.....36
Figure 3-3: M280 DMLS Printer from EOS[101].....37
Figure 3-4: Stripe Scan pattern.....38
Figure 3-5: Hatch spacing with an overlap of a) 20 μm b) 0 μm.....39

Figure 3-6: Hatching spacing with an offset of a) 20 μm b)40 μm 39
Figure 3-7: Nomenclature of Samples for Identification.....39
Figure 3-8: a) Sample Coupons after printing b)Dimension of sample coupon.....40
Figure 3-9: Cut part from the bottom of the sample.....40
Figure 3-10: a) Hot- Mounting press b) Grinding and polishing station.....41
Figure 3-11: a) Mounted sample b) Sample after grinding.....41
Figure 3-12: a) Micrograph size b) Approximate areas where images were taken 42
Figure 3-13: Branson Ultrasonicator 43
Figure 3-14: Mettler Toledo Balance.....44
Figure 3-15: Vickers Hardness Tester 44
Figure 3-16: Optical Profilometer [102].....45
Figure 3-17: Universal Mechanical Tester Tribolab[103].....47
Figure 3-18: Schematic of the wear test 47
Figure 4-1: Effect of increasing V.E.D on surface porosity with (a) high level of porosity at 28.57 J/mm3 (b) moderate level of porosity at 39.68 J/mm3 (c) low level of porosity at 66.67 J/mm3 (d) very low level of porosity at 111.11 J/mm3 (e) re-emergence of pores.....48
Figure 4-2: Porosity levels as a function of V.E.D.....51
Figure 4-3: Micrographs showing low v.e.d samples impregnated with lack of fusion pores at increasing v.e.d of (a) 20.41, (b)28.57, (c)34.01, (d)39.68, (e)44.44 and (f)55.56 J/mm^3 52
Figure 4-4: Micrographs showing high v.e.d samples impregnated with circular gas pores at increasing v.e.d of (a) 66.67, (b)79.37, (c) 83.33, (d) 88.89, (e)111.11 and (f) showing keyholes at 142.86 J/mm^3 53
Figure 4-5: Effect of Laser Power and Scan Speed on Porosity size and distribution using a constant hatch spacing of 80 μm a) G1B2 b) G1C2 c) G1C3 54
Figure 4-6: Effect of Laser Power and Scan Speed on Porosity size and distribution using a constant hatch spacing of 100 μm a) G2D1 b) G2B1 c) G2B2 55
Figure 4-7: Effect of Laser Power and Scan Speed on Porosity size and distribution using a constant hatch spacing of 120 μm a) G3D3 b) G3C3 c) G3C2 56
Figure 4-8: Effect of Laser Power and Scan Speed on Porosity size and distribution using a constant hatch spacing of 140 mm a) G4D3 b) G4B3 c) G4B2 57
Figure 4-9: Effect of Scan Speed on Porosity size and distribution using a constant hatch spacing of 140 μm a) G4C1 b) G4A1 c) G4D1 58
Figure 4-10: Sensitivity of scan speeds to part porosity.....59
Figure 4-11: Sensitivity of Laser Power to part porosity.....60

Figure 4-12: Sensitivity of hatch spacing to part porosity 61
Figure 4-13: Part Density as a function of V.E.D 62
Figure 4-14: The hardness of samples as V.E.D Increases 64
Figure 4-15: Effect of v.e.d on the amount of un-melted powders showing (a) high amount of unmelted powders at 44.44 J/mm^3 (b) moderate level of unmelted powders at 63.49 J/mm^3 and (c) powder depression at 66.67 J/mm^3 65
Figure 4-16: Effect of power on sub-grain structures a),b) Sample G4B2 with P=200W, h=0.14mm and v=750mm/s c),d) Sample G4B3 with P=200W,h=0.14mm and v=750mm/s 66
Figure 4-17: Effect of scanning speed on sub-grain structures a), b) Sample G1B2 with P=200W, h=0.08 mm and v=750mm/s c), d) Sample G1C2 with P=200W, h=0.08 mm and v=1250mm/s 67
Figure 4-18: Effect of hatch spacing on sub-grain structures a), b) Sample G1C2 with P=200W, h=0.08 mm and v=1250mm/s c), d) Sample G3C2 with P=200W, h=0.12 mm and v=1250mm/s 68
Figure 4-19: Effect of Speed on crack formation a) Sample G1B2 with P=200W, h=0.08 mm and v=750mm/s b) Sample G1C2 with P=200W, h=0.08 mm and v=1250mm/s 69
Figure 4-20: Effect of hatching space on crack formation a) Sample G1C2 with P=200W, h=0.08 mm and v=1250mm/s b) Sample G3C2 with P=200W, h=0.12 mm and v=1250mm/s 69
Figure 4-21: Effect of power on crack formation a), b) Sample G4B2 with P=200W, h=0.14 mm and v=750mm/s c), d) Sample G4B3 with P=250W, h=0.14 mm and v=750mm/s..... 70
Figure 4-22: Roughness 3D representation of sample a) G1B2, b)G2B1 c)G4B2 d)G1C3 71
Figure 4-23: Wear tracks of samples after wear a)G3C2 b)G4B3 c)G2B2 d)G1C3 72
Figure 4-24: Mass loss for all samples 73
Figure 4-25: Effect of Power on mass loss using hatch spacing of a) 80 μm b)140 μm 73
Figure 4-26: Effect of Speed on mass loss..... 74
Figure 4-27: Effect of Hatch spacing on mass loss using speeds of a) 750 mm/s b)1250 mm/ 74

LIST OF ABBREVIATIONS

AM-Additive Manufacturing

MAM-Metal Additive Manufacturing

SEM-Scanning Electron Microscope

OM-Optical Microscope

UMT-Universal Mechanical Tester

VED-Volumetric Energy Density

COF-Coefficient of Friction

SS-Stainless Steel

GMA- Gas Metal-Arc

OP-Optical Profilometer

ANN- Artificial Neural Network

PBF-Powder Bed Fusion

L-PBF-Laser Powder Bed Fusion

EBM- Electron Beam Melting

SLS-Selective Laser Sintering

SLM-Selective Laser Sintering

EDS-Electron Dispersive spectroscopy

ASTM- American Society for Testing and Materials

EDM- Electrical Discharge Machining

1 INTRODUCTION

1.1 Background

Metal-based Additive Manufacturing (MAM) is gaining a lot of traction in the manufacturing industry mainly due to its ability to create parts with complex geometries or intricate shapes. Such attractive capabilities have been adopted by the medical field for customization of orthopedics to fit each individual patient, with the added advantage of tailoring the microstructure of these implants to mimic the stiffness of bone to prevent stress-shielding [1]–[4]. MAM can be used in the production of lightweight components in the Aerospace and Transportation Industry to increase part safety and fuel efficiency [5]–[7] However, there is a major hindrance to this manufacturing process which has limited further applications in these fields. Parts processed using this manufacturing technique are confronted with many defects and discontinuities which affect the integrity of the printed part. Defects such as porosity, that compromises the load-bearing capacity and cracks resulting from residual stresses, are induced during the printing of the parts [1][8]–[12]. Also, the presence of non-equilibrium phase changes, due to the irregular and repetitive thermal cycles during the printing process makes it very difficult to predict mechanical and material properties of the printed parts [8], [12]–[14].

1.2 Problem Statement and Research Objectives

The full capability of these techniques is not realized due to a lack of consensus on the methods, material, and design that will help manufacturers better compare parts. The performance of parts from different printers of the same technology and even different manufacturing processes can be compared as well [15]. An optimized parameter for one material will not necessarily result in the same superb performance of another material, even when the same 3d printer is used [16], [17]. This gives the need to extensively study the effect of the printing parameters on the microstructural integrity of the printed part to understand the exact contribution of these parameters to the microstructure. Studies on MAM have shown that there are over 130 printing parameters that affect the structure of the final part, which include laser power, scanning speed, laser spot size, layer thickness, scan pattern, etc [18]–[20]. These parameters are found in the printing machines that have adopted the laser powder bed fusion technology for metal additive processing. However, detailed studies on how these printing processes and parameters affect the final microstructure and other printing-induced defects are still being carried out. The most common parameters of the laser powder bed fusion technology that requires little to medium level of expertise to manipulate include laser power, scan speed

and hatch spacing between the scan lines. Also, these are the parameters that can easily be changed without voiding the warranty of a Metal 3D printer which is very expensive.

A few researchers have explored the effect of individual parameters on the microstructure of the final printed part. The hardness of laser-sintered 316L steel parts was attributed to the hatch spacing in the research conducted by Debak et al [5]. This study also found no relation between the micro-hardness and the part density. Kasuma concluded that the balling effect is a result of extremely high laser scanning speeds whereas instability zones are brought about by low speeds [20]. MAM techniques such as the SLS is currently being used to produce complex metallic and high-performance parts for use in high-stress applications in the aerospace and automotive industries. However, there is no widespread use of AM processes for direct part production in these industries because of various concerns including gaps in performance metrics, standards to improve the accuracy of AM parts and lack of consensus on properties of produced parts [21]. Also, processing parameters and constituent powder materials produce microstructural heterogeneities which influence the properties and quality of parts fabricated via AM [21], [22].

What researches have been doing over the years is to combine the critical printing parameters and coming up with different iterations. These combinations are then used sets of printing parameters to fabricate the parts, which are extensively characterized to determine optimized parameters for printing. Optimized parameters that are beyond the limitations of a 3D printer results in the entire process of finding optimized printing parameters being repeated. Because of this, a single expression is needed that is going to depict the combined effect of these crucial printing parameters. In this case, giving an optimized expression will make it easier for others to work their way back to spitting out parameters based on their printer's limitations or resource limitations.

This single expression employed here is the Volumetric Energy Density (VED) which combines these critical printing parameters. In order to find an optimized VED which produces parts with good microstructure and mechanical integrity, parts need to be created with different parameters that need to be extensively studied to find the influence of the parameters on the final parts. This leads to the objectives of this study:

- Process 316L Stainless Steel Alloy with varying parameters (Laser power, Scan speed, and Hatch spacing) using Direct Metal Laser Sintering
- Assess the effect of the printing parameters on the microstructural Integrity of 316L Stainless Steel Alloy
- Evaluate the effect of the printing parameters on the hardness and wear behavior of 316L Stainless Steel Alloy

1.3 Research Methodology

For this study, we are focused on L-PBF technology because of the ease of use of these technologies and their widespread use in the manufacturing field. L-PBF has undergone a variety of iterative improvements over the years making it exceptionally useful for a variety of engineering applications. This technology can be used to create a fully dense part that offers close to or better properties than conventionally manufactured parts. Stainless Steel 316L is the material of choice for this study because this material is known to have high strength and high corrosion resistant properties. Also, this material has gone through numerous certifications to be used on most 3d printers without special permission from the manufacturing in fear of voiding warranty of the machines. The first part of the project was printing the stainless-steel coupons using a variety of printing parameters using the DMLS M280 equipment. The parameters are grouped based on the hatch spacing used starting with 80 µm as the least and 140 µm as the largest. The other parameters mainly the laser power and the scan speeds are also varied to create 15 different iterations for each sample coupon.

The second part of the experimentation is trying to access the printed sample to determine the effect of the parameters on microstructural integrity. The densification of the parts is accessed by determining the mass of the sample in air and then the mass in the air as stated in the ASTM standard B962 – 17 that outlines the method determining the density of compacted or sintered powder metallurgy (PM) products using Archimedes' Principle. The samples are characterized based on the parameters that give a good microstructure. Techniques used include sample preparation using various metallography processes (grinding, polishing, etching). Firstly, the samples are studies under optical microscopy to study the morphology of the sample surface. The surface porosity is done using Image J software. Ten images are taken through image binarization and thresholding and the pores are then easily identifiable and analyzed to find the fraction the surface of the samples that are covered by pores. The optical micrographs are used to investigate the effect the printing parameters have on the size, shape and distribution of the

pores. The second part of the microscopy analysis involved the use of a scanning electron microscope to get detailed information about the particles that are present on the sample surface. The spatial distribution of these particles which were on a submicron range as well as to conduct a chemical analysis of the particle to ascertain if they are any chemical changes that occur during the printing process.

The final part of this study accesses the contribution of these parameters on the mechanical behavior of the samples. The hardness values of the samples as a function of the printing parameters are also accessed. The hardness properties of the samples are studied using Vickers Hardness Tester which gives the hardness values on the micro-scale in HV. The other mechanical performance behavior that was investigated was the wear resistance of the sample as the printing parameters are changing. The wear resistance of the samples is analyzed using Universal Mechanical Tester (UMT) Tribolab.

1.4 Summary of Findings

The effect of printing parameters on the bulk material properties such as porosity, cracks, density and amount of unmelts seen in the printed sample has been established by numerous researches which have also confirmed with this study. It is easier to combine the printing parameters into a single expression to study the combined effect of these parameters on the bulk material properties. This expression is referred to as the Volumetric Energy Density (VED) which combined the Power, Speed, Hatching Distance, and Layer thickness. Increase in the VED shows a considerable reduction in the porosity, density, amount of unmelts and Lack of fusion (LOF) cracks but extremely high VED less to these discontinuities re-emerging on the sample surface. The stable VED range that produces a quality part with good microstructure integrity is 40-100J/mm^3.

Although, the VED shows a direct correlation to the bulk material properties but no observable trend with the evolution of the microstructure features and properties such as the morphology, size and spatial distribution of the sub substructures that form as a result of the rapid solidification of the 3D printing process. A better understanding is derived by looking at the effect of the individual parameters have on the microstructure features, which was evident as the increase in power and speed independently cause the subgrain structures to increase in size and spatial density.

The hatching distance is the parameter that influences the extent to which scanning speed, the most sensitive parameter among the three affects the microstructure as well as the mechanical properties. For whichever application, choosing a hatch spacing will determine the range of values of the other printing parameters required to create a better microstructure. To use a low hatch spacing, a moderate level speed and power are required to maintain the microstructure integrity as well as the mechanical properties. Structure application components require either a high laser power in combination with a hatch spacing or a small hatch spacing with a moderate level of power. In all these scenarios the scan speed should also is moderate. For creating porous parts with stable pores, high laser power in combination with low hatch spacing is desired as well as a combination of low laser power and low scan speed. The change in the individual parameters and the effect on pore size and count appear to be random and perhaps a volumetric analysis will give better insight.

The hardness values of the printed samples are higher than conventionally manufactures 316L stainless steels due to rapid heating and cooling which leads segregation of the grains creating fine cellular and lathe/columnar substructures. The hardness values for VED above 40 J/mm3 were averaging at 235 HV. The mass loss recorded shows better wear properties obtained when considerable energy input is delivered to the sample which is mostly dictated by the hatch spacing used. In all when the energy is too much the microstructure begins to deteriorate and with low energy input, the properties are lower than expected.

1.5 Thesis Organization

This dissertation is structured into six chapters. The following are summaries of the chapters:

- Chapter 1 introduces metal additive manufacturing, the need for such technology, the hindrance to the advancement of this technology, and why an extensive study on the processing is going to help improve the technology specifically for 316L stainless steel alloy.
- Chapter 2 reviews studies done on the various types of Metal Additive Manufacturing, the advantages, and challenges with the field.
- Chapter 3 describes the material and experimental procedures used in this research. A detail description of the equipment and procedure used for characterization, including metallographic and microscopic examinations used.
- Chapter 4 provides comprehensive observations of the results from the metallographic studies and the properties.

- Chapter 5 discusses the main findings in this research based on the results of the microstructural observations of the specimens.
- Chapter 6 presents a summary of the results and conclusions from this study. In addition, references and research contributions are presented at the end of this thesis.

2 LITERATURE REVIEW

2.1 Metal-Additive Manufacturing

The numerous advantages the 3D can offer have led to the studies in advancing this sector of manufacturing most of which will be discussed in detail in chapter 2.3. 3D printing started with plastic and polymeric materials that are insulated and do not possess the mechanical properties to be used in functional components and later research began with metal feedstock [23]. In 1983, the first-ever 3D printer saw the light of day with Chuck Hull creation. Since then, the industry has been dominated by studies of the 3D printing process and technology. Metal 3D printing was born out of experimentation with laser on polymer powders with was later replaced with metal powders[24], the powder bed process was born. The first-ever metal 3D printer part made by Manriquez-Frayre and Bourell in 1990 using the Laser Sintering technique [24]. Five years later, EOS started to get into the market and came out with the first commercially available metal 3D printer which uses the Selective Laser Melting technique (SLM) and then went on to license Selective Laser Sintering rights from 3D systems with the sole purpose of developing the powder bed technology aspect of the license [25]. In the same year, Laser Engineering Net Shaping was developed by Sandia National Laboratories which was had a different delivery mechanism to get the metal powder to the build platform [26]. Another powder bed technology was invented in 2000, which uses an electron beam (EBM) as the heat source instead of a laser. Arcam AB industries licensed and then developed the EBM technology to the market. Metal 3D printing has seen a lot of iteration and evolutions over the years to what it is now, although these technologies and processes have not gotten to the level that we perceive them to get to at this stage. This is mainly the reason why there has been a growing interest among the scientific and technological in these areas.

2.2 Types of Metal-Additive Manufacturing

There are various metal AM technologies that are currently being adopted in the industries. These are grouped under two main types, based on the feed material and the way the materials are bounded, Powder Bed Fusion (PBF) and Direct Energy Deposition (DED) [27], [28]. For PBF technology, the source of the power or heat is supplied by either a laser (L-PBF) or Electron Beam (E-PBF) and the feedstock material is powder bed, hence the name, Selective Laser Sintering (SLS) or a variation of that, Direct Melting Laser Sintering (DMLS) and Selective Laser Melting (SLM) [12]. SLS technique involves solid-state fusion, where the powders are heated to approximately half of their melting temperature to achieve a solid-state

fusion. Generally, SLS involves the use of a binding agent to aid in particle consolidation. DMLS is used when there are no binding agents required and the laser is used to directly heat up the powders for sintering. SLM is liquid state fusion where the material or powders are heated to their melting temperature, so the solution forms a liquid pool. The distinguishing factor between these technologies is the temperature at which each is achieved but lately, even SLS systems can reach high enough temperature to induce melting making the lines between these two blurry. EBM is the powder bed technology that uses a high energy electron beam as the energy source.

2.2.1 Powder Bed Fusion (PBF)

Powder Bed Fusion technology involves using a high energy laser or electron beam to either partially melt or fully melt metal powers to help them sulfidation into a solid model. This separates the technology into Laser PFB (L-PFB) and Electron Beam Melting or Electron-PF (EBM/E-PBF). L-PBF is further categorized into two main processes; when the powders are partially melted, to approximately half of the melting temperature of said material, the process is called Laser Sintering (LS) or Selective Laser Sintering (SLS). Selective Laser Melting (SLM) is another process of L-PBF that involves the complete melting of the metal powder which at this instance involves attaining the same or above the melting point temperature. Lately, the printers used for both types of Laser powder bed fusion technologies are equipped with very high lasers that can achieve full metal powder melting, making the difference between them blurry. A typical L-PBF includes of a powder bed which has the substrate serving as the platform for the part being printed, a powder tanks containing the reserve metal powder, a re-coating blade or roller that moves the metal powder from the tank to the powder bed, a laser source and sets of mirrors that work together to move the lasers [29]. The schematic of the L-PBF is shown in Figure 2 1 below. The process involved fusing of metal powders using a laser beam.in a chamber. The same temperature is maintained in the as that of the powder bed for better thermal distribution. The first layer of powder is fused first with the laser beam and then the piston lowers the bed the same distance as the layer thickness. The roller arm then is used to push more metal powder onto the bed and then the next layer of the part is fused. This is repeated a number of times until the part is completely built [30]. EBM employs the use of high energy electrons as the heat source to achieve full melting of the powder bed feedstock. Both L-PBF and EBM use the same principle but have a difference in the setup of hardware [24]. Manufacturers who have jumped into this aspect of manufacturing includes EOS, Arcam, Farsoon, Realizer, SLM Solutions, Sisma, Concept laser, Trumpf [24], [31]–[35].

The EBM uses similar components as the Scanning Electron Microscope like the filaments to generate the electrons, the collimator to help position the electron beam, all shielded in a giant column [24].

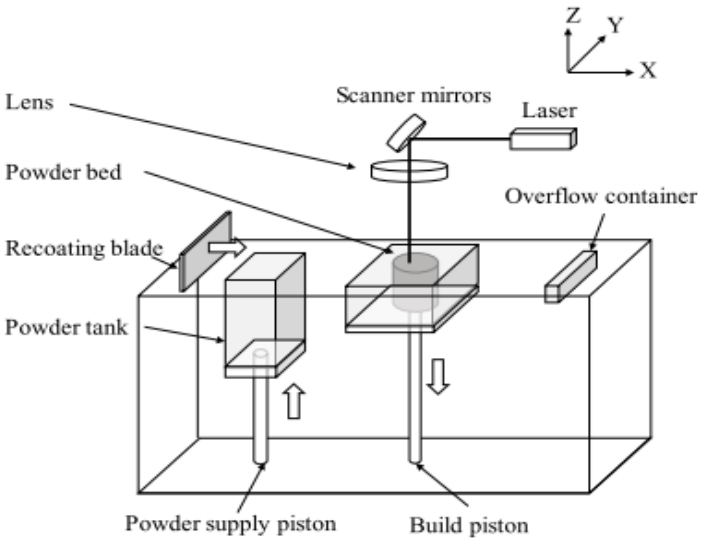

Figure 2-1: Schematic of the Laser Powder Bed Fusion process [28]

This technology consists of electron Beam gun providing the focus electrons, powder hoppers to deliver powder to the bed, and a rake to spread the powder supply unto the bed [29]. This process is very similar to SLS/SLM processes but uses an electron beam as its energy source. In this cutting edge PBF technology, a high electron beam with 30-60 KV is used to melt the powder feedstock. The chamber is vacuum-sealed to prevent oxidation from occurring. This technology is favored for different types of metal and compositions and is earmarked to be used in making functional components in outer space in the near future [7]. The schematic of the EBM is shown in Figure 2 3. PBF is characterized by a scan pattern and strategy and laser control parameters. The powders that are not used in creating the 3D printed part is recycled and used later in another print by sifting to get rid of any sintered clusters. EBM powder recycling goes through a recovery system for it to be used again. Some of the PBF parts stick to the substrate and need to be cut off using a method that does not introduce deformation or heat that can affect the microstructure of the As-printed part. The best form of machining to remove parts from the substrate is the Wire Electrical Discharge Machining (Wire EDM). Using material combinations with poor adherence such as a Titanium alloy print against a stainless-steel substrate does not require cutting, because the prints fall off the substrate right after printing. 3D printed W-Co parts are usually stuck to the stainless-steel substrate and

require wire EDM cutting to take them off, and most of the time lose some of the material in the process. With the DED technique, the fusion of the metal feedstock (powder/wire) happens as they are being deposited. DED involves the use either wire or powder metal feedstock, and use either a laser, arc or electron beam[24].

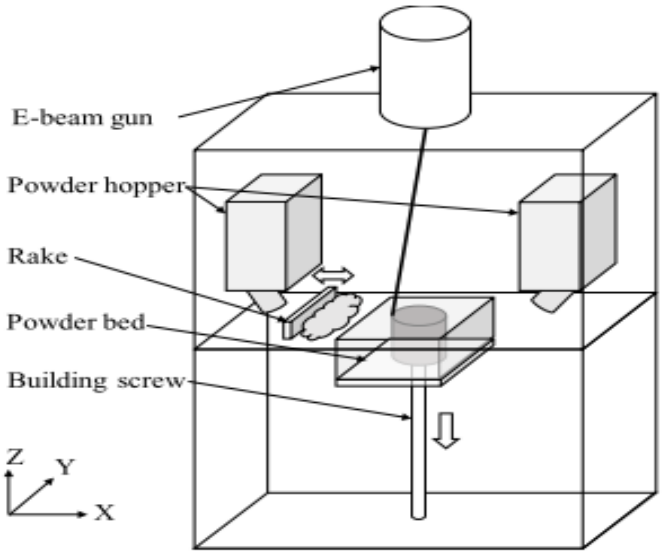

Figure 2-2: Schematic of Electron beam Melting Technology [29]

2.2.2 Direct Energy Deposition (DED)

A wire DED and Powder Bed DED schematics are shown in Figure 2 4 & 2 5. This technology originated from the old fashion welding technology where the feedstock which is outside the build environment is delivered coaxially with the source of heat, either laser or electron, into a melt pool [5], [24]. Direct Metal Deposition (DMD), Laser Engineering Net Shaping (LENS) and Electron Beam Free Form Fabrication (EBFFF) are the most common DED techniques. DMD is favored for adding features to already existing parts. EBFFF is used in a vacuum and employs a metal substrate. Laser Engineering Net Shaping (LENS) is the most studied type of DED technology and patented by the Sandia National Laboratories [36].

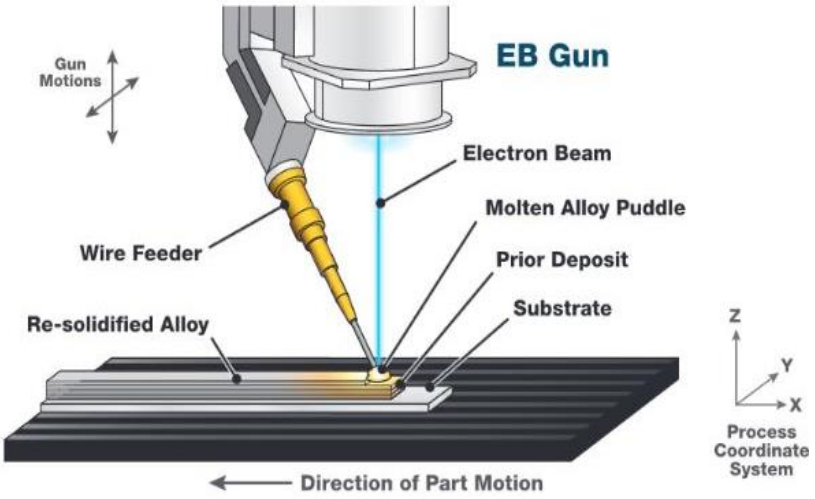

Figure 2-3: Schematic of a wire DED technology [23]

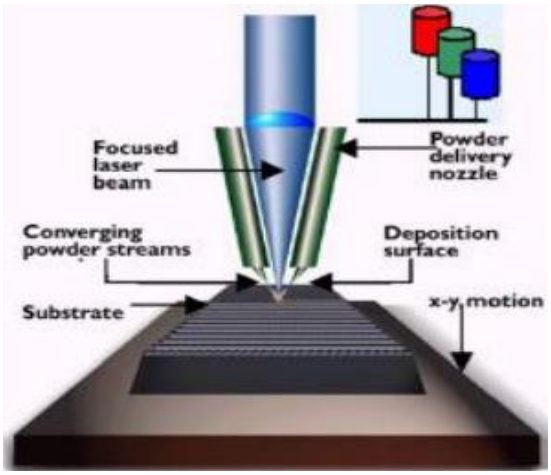

Figure 2-4: Schematic of Power Bed DED [24]

LENS has to do with building parts with molten metal powder injected at a location. The molten metal solidifies after cooling down. The chamber used for this type of technology is purged with argon gas to get rid of trapped oxygen. Due to the inert atmosphere created by the argon gas, the types of metals that can be used here are numerous like stainless steel, nickel-based alloys, titanium-6 aluminium-4 vanadium, tooling steel, copper alloys, etc. This technology suffers from high amounts of residual stresses as a present in most types of metal 3D printing technologies. LENS technique is being adopted to be used in parts repair that will cost an arm and leg to do with other techniques. An illustration of the LENS technology is shown in Figure 2 6. DED is not as popular as PBF technologies due to its lower level accuracy and the less amount of research done in these areas of study [9][27], [37].

The DED setup is also like the PBF in a way such as having a build plate/substrate and hopper filled with feed material. The build plate can have a 3-degree of freedom for a stationary system and when it employs a rotary build plate, 5-degree of freedom. The rotary platform gives more freedom to design very intricate shapes or parts [24]. The build chamber is filled with an inert gas only if the material used to produce the parts is reactive, but an inert gas is not necessary for non-reactive material since the shield generated by the gas aimed at the melt pool is more than enough to shield the process from oxidation. Reactive material such as titanium requires purges the chamber with either argon or nitrogen to reduce the amount of oxygen in the chamber thereby reducing oxidation to an acceptable amount [24]. Post-processing usually required to relieve the material of any residual stress resulted from the high thermal gradient associated with these types of technologies. The use of techniques such as severe plastic deformation, to improve the mechanical behavior is sometimes used after the part has been printed and based on the specific application required. Again excess powder may be recycled by collecting them with a vacuum [24].

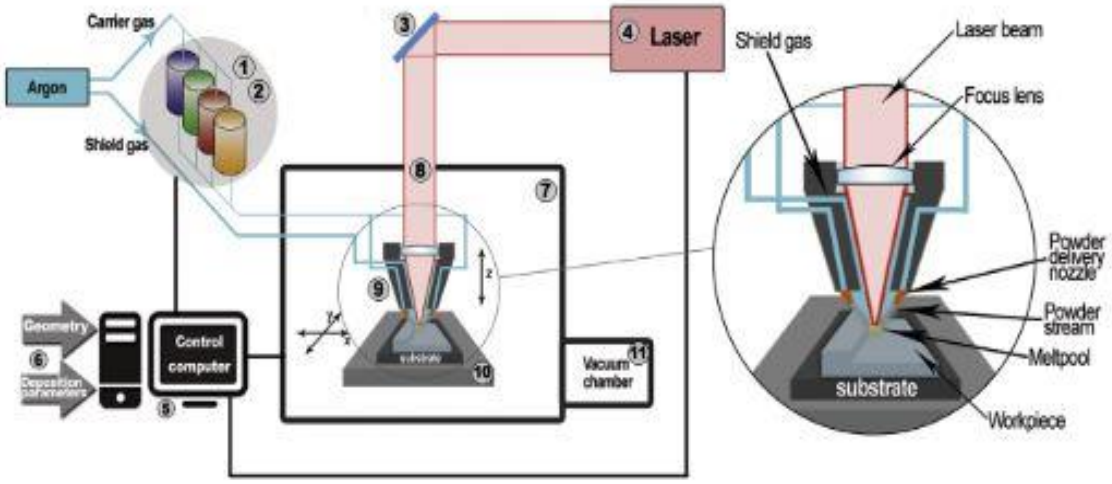

Figure 2-5: Schematic of LENS technology[38]

2.2.3 Binder Jetting

Binder Jetting (BJ) basically uses a binder, which in some cases is another metal, to help hold the metal powders together. The binder is usually made of materials that have a low melting temperature. Porosity is a huge impedance to this metallurgical process as it is in most sintering processes. An illustration of the BJ techniques is shown in Figure 2 7. This technology is developing based on several studies conducted on powder metallurgy and ceramics in the past.

The manufacturer that has jumped on this additive manufacturing technique is ExOne who developed the BJ printers used mostly for this process of manufacturing. Mostly, the use of boron as a binder for the iron sintering process is common with this technological process. After the sintering process, the output, referred to as the 'green state' must cure for a period of a quarter to half a day, then sintered for 1-1.5 days at a temperature close to 1100^{o}C to obtain a 60% dense material. The sintering process burns off the binder, so the parent material is the only one left after the process. To obtain higher densification, the binder material used is a metal that does not burn off but infiltrates the parent material and eventually fills the spaces between the powders left after sintering. A typical bronze binder can achieve up to 95% densification and annealing is done to remove residual stress and improve the ductility of the material at the end. BJ is not as researched as PBF or DED techniques and as such not very detailed schematic is readily available in the public domain [24].

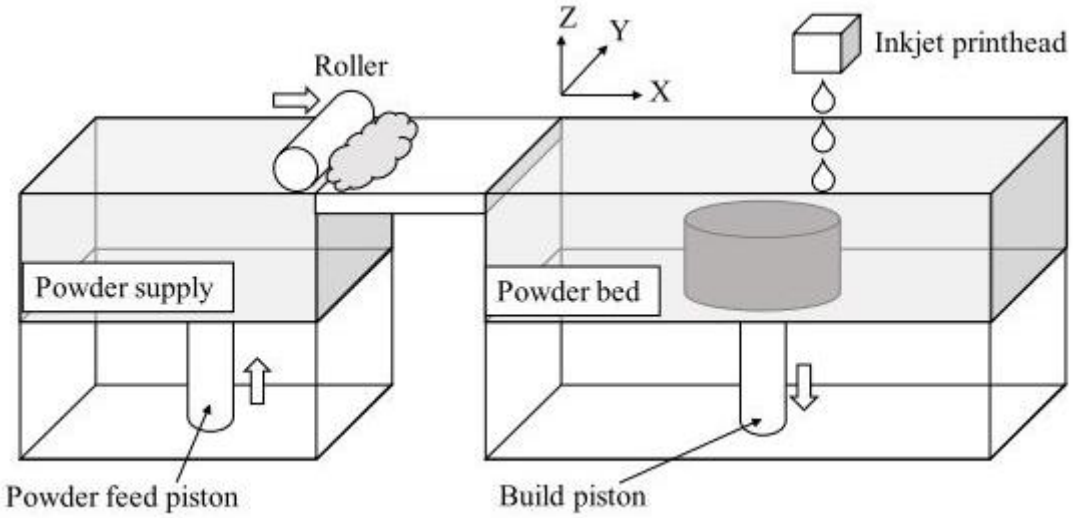

Figure 2-6: Schematic of Binder Jetting [29]

2.2.4 Sheet Lamination

Sheet Lamination involved using numerous techniques including brazing, welding, diffusion bonding, or ultrasonic consolidation to stack 2D metal sheets in a 3D object[39]. Welding techniques employed here are laser and resistance welding, and the sheets used are either cut according to the required dimension before stacking them together or the stacking is done and then the geometries are machined unto the 3D object [24]. This technology has several advantages; the metal sheets retain their initial properties, there are less geometric variation in

the final part, better surface finish, and extremely cheaper to make. This type of production creates parts that are considered strong in the stacking direction but cannot withstand shear or tensile loading due to the way they are made causing anisotropic behavior in the final part just like most 3D printed objects. The detail steps to brazing in this type of manufacturing technique are shown in Figure 2 8. Here brazing is achieved by coating the sheet with flux and serves as a brazing alloy between the joining sheets [24]. For resistance welding techniques, fixtures are required to produce the resistive force need for the sheets to adhere to each other. The presence of this severe limitation in joining sheet metal together, other avenues of joining sheet metal is being explored to come up with a better and more resilient joining process. This brought about the Ultrasonic Seam Welding process referred to as the Ultrasonic Additive Manufacturing technology (UAM) which is the method mostly used in this type of manufacturing process and therefore studied more into detail [40]. The process for UAM is as follows; mill and blow tailing off the substrate to obtain a flat and polish substrate, deposit metal tapes with the ultrasonic welding and trim off excess tapes from the edges of the sheet, repeat until the desired object is achieved, and finish the process off by machining any remaining features into the part where necessary [41]. The illustration of this technique is shown in Figure 2 9.

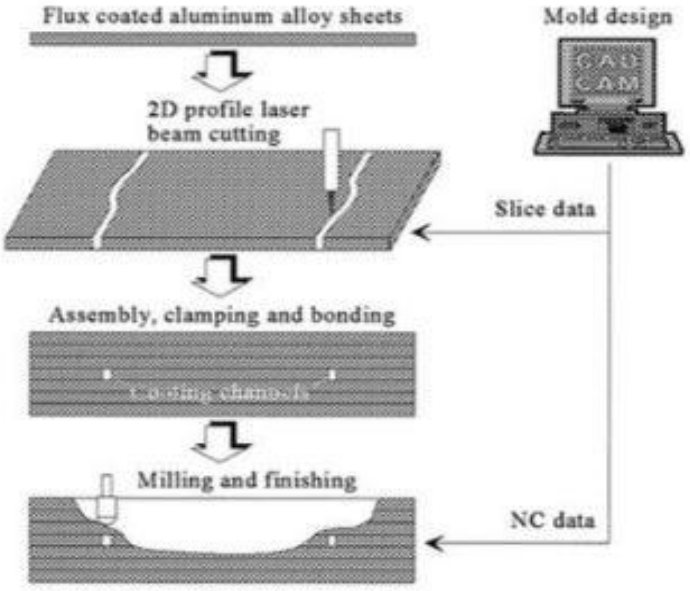

Figure 2-7: Steps involved in brazing sheet metals together [24]

How the material is joined at the interfaces is the bases for understanding how this material is going to behave. Also, since there are no support structures employed in this type of manufacturing technology, creating parts with overhang feature will prove problematic and therefore is best used to create metal composites. This manufacturing technique is always in conjunction with the machining process to produce the finished product. Tooling or machining can also be hindered depending on their location on the object [24].

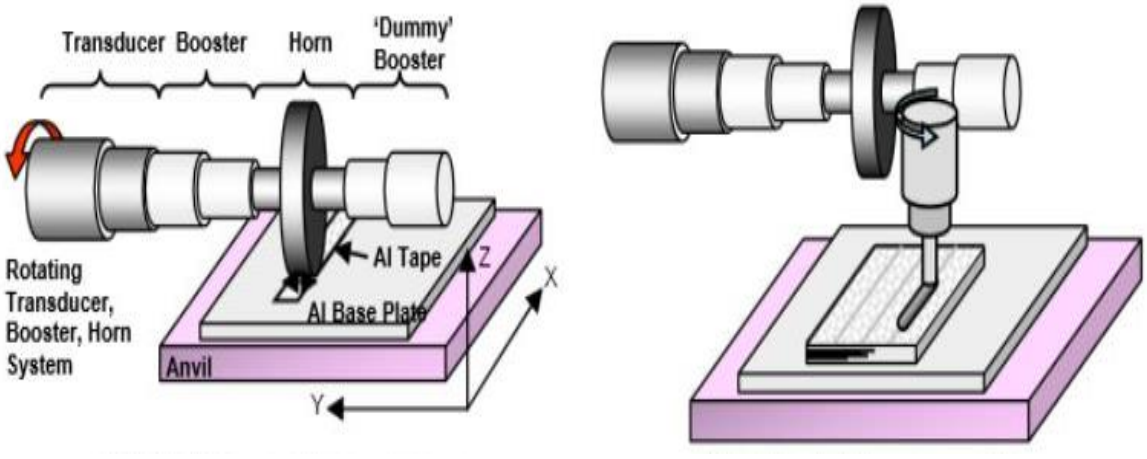

Figure 2-8: Schematic of UAM Sheet Lamination technique [24]

2.3 Advantages and Applications of Metal-Additive Manufacturing

Since the 1990s, demand for advances in additive manufacturing has developed from the advantages of additive manufacturing over traditional manufacturing processes. Parts of any desired mechanical and chemical property, with a continuously growing list of printable metals, metallic composites and alloys enable manufacturers to produce a wide range of materials. Processes such as DMLS can manufacture convoluted units or structures without the need for tools. Sectors such as the Military, Aerospace, Medical, Dental, and Automotive industries benefit from the use of additive manufacturing technologies. Additive manufacturing has many benefits in terms of cost savings, shorter time to market, product quality, innovation/transformation and societal significance over current manufacturing methods [41][42]. Traditional production methods cannot be entirely replaced by additive manufacturing but are expected to reduce in many niche areas [42]. Customization can easily be achieved with additive manufacturing techniques. Designs can be easily be shared digitally, thereby aiding the adjustment and customization of products.

2.3.1 Intricate and light-weight part fabrication

The challenge with making lightweight components in the transport industry is making sure that they have the same if not better mechanical properties. MAM has introduced the capability for the manufacturing of open cellular foam type designs with cut-outs that greatly reduces the weight of the part whiles maintain the same strength [1], [43]. The capability with MAM on creating an optimized design with less material than traditionally being achieved is endless. Traditional methods are limited in the intricacies that they can manage nut with MAM, the limit is with imagination. Any pre-alloy material has the potential to be additively fabricated for optimized performance and weight reduction which is not only going to improve efficiency but also reduce cost since less material is involved in the manufacturing process [7].

Environmentally friendly procedures are possible using AM techniques. The flexibility of AM enables manufacturers to improve product designs for lean production and little to no waste production. Reduced raw material usage contributes to the continuously growing need for the world to go environmentally friendly and reduce net carbon emissions. The reduced raw material used helps lessen energy consumption which in turn affects the environment less. Additionally, the advanced designs that AM realizes increase the range of capabilities, hence reducing fuel, energy or natural resources required for the process[44]. AM could make efficient use of raw materials to produce little or no waste while arriving at decent geometric efficiency.

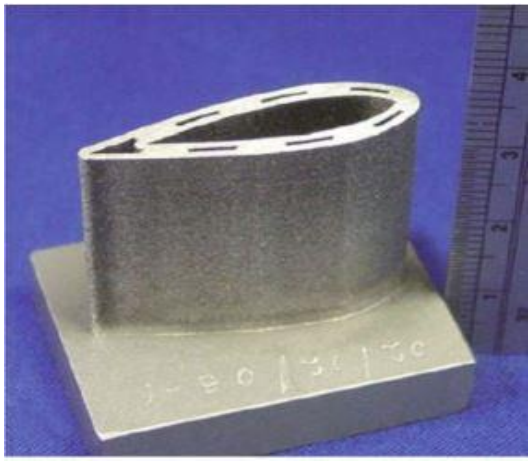

Figure 2-9: Airfoil with embedded cooling channels[1]

A typical example is the fuel nozzle tip design by General Electric with 14 distinct fluid passageways which could only be manufactured with Metal-AM. This new design after manufacturing weighed 25% less than the old model and increased fuel efficiency by 15%.

Components like an aerofoil with embedded cooling channels that are challenging to manufactured due to the small volume of the embedded features are easily made with Metal-AM. Airbus A350 brackets made by LMD using military-grade titanium alloy employing a state-of-the-art bionic design brought the weight of the old designs, which were made by conventional milling, down to 30%.

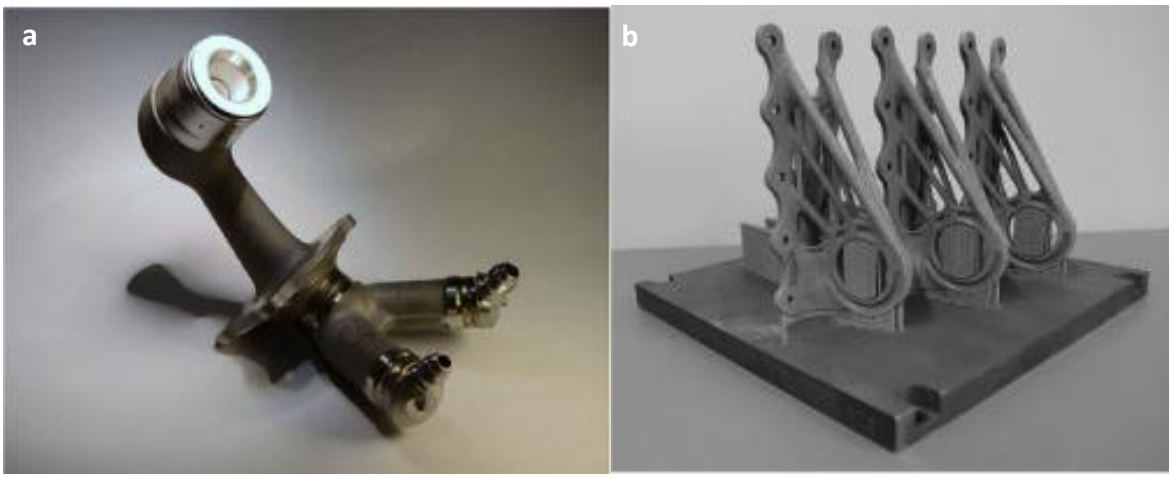

Figure 2-10: Lightweight applications of MAM a) GE fuel nozzle tip b)bracket for Airbus 350 [28]

2.3.2 Defense applications

For the defense industry, it is very critical to be in the capacity to replace mission-critical components of equipment on the field without having to return to base for repairs. Having the capability to print functional parts that are mission ready will be a huge step in the right direction without the life-threatening and logistical challenges of having to move defective equipment. The 'Jesus nut' also known as the main rotor retaining nut is the most important component in an aircraft that when it fails leads to immediate and sure catastrophic failure. Successfully printing a functional nut will usher a new paradigm in aircraft maintenance and safety.

Ti6Al4V and Alloy 718 are widely used in turbine applications of aircraft with temperatures exceeding 315℃. GE has used 50% by weight of these alloys in the rotating forgings of the turbines [45], [46]. Having replacement parts and techniques that significantly reduce downtime while preserving structural integrity is extremely desirable. Repair processes using some additive manufacturing techniques will reduce downtime and cost considerably by substituting only the damaged or worn out part whilst maintaining structural integrity. Additive

manufacturing has a much faster shift from the design stage to the manufacture of the final product. With a direct transition from 3D Computer Aided Designs (CAD) models, no molds and tools are required. This provides the possibility of complex geometries that are difficult to reach using subtractive methods to be easily and efficiently manufactured. The inability of traditional manufacturing methods to construct complex geometries comes short to the ability of MAM technology to print differently manufactured parts as one consolidated part. The military employs MAM to prototype wind tunnel testing models for planes, missiles, etc. to compare the performance of new designs. This reduces the cost of building a full-size part without testing a model or the time it takes to model these complex parts with traditional manufacturing techniques. Dameshmand et al used SLS to fabricate a wind tunnel model with subsonic and transonic testing methodology. The SLS model was accurate and shaved of time and cost as well [47]. Bell flight working out of Fort Worth in Texas uses LENS technology to create a gas turbine exhaust nozzle to a $1/6^{th}$ scale. Arcam, a subsidiary of GE, is the industry leader in EBM technology. Arcam uses this technology to create a wide variety of military aircraft functional components using the most widely research metallic alloy, Ti6Al4V. Parts like turbines with thin walls and embedded channels are the components that benefit the most with MAM. MAM can also be used in a support capacity for other traditional manufacturing technology like molding or casting by additively fabricating molds and dies. Satellites for military and communications also benefit from MAM, as these techniques are used to rapidly create several of its functional components. Optomec is a leading industry partner in making satellite and jet engine components with an expertise in LENS technology [48].

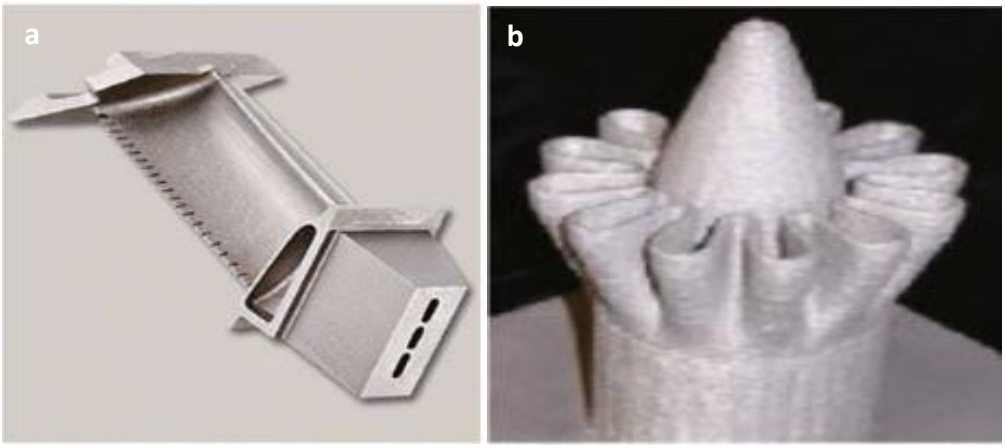

Figure 2-11: a)Turbine blade with cooling channels b) Bell rotorcraft mixing nozzle made by EBM[1]

2.3.3 Medical Applications

Additive manufacturing in the medical field has been grouped into five major groups: medical models, surgical guides, surgical implants, external aids and bio-manufacturing [49]. Improved quality through this technology is possible as the medical field has followed this form of manufacturing. 3D printed implants and prosthetics patients are getting an improved quality of healthcare. Orthopedics are being customized to fit each lone patient better thereby allowing companies to enhance their final product and services. Rapid technology is also being used in dentistry and is being used to fabricate maxillo-facial prosthesis [50]. An added advantage of this process is the ability to prevent stress-shielding by tailoring the microstructure of the material of the implant to resemble the rigidity of bone. Medical grade titanium alloy Ti6Al4V trademarked ELI are intentionally employed with induced pores to make tissues grow into them for extra support. The fact that pores can be induced and controlled with MAM in transplant opens a whole other area of interest to manufacturing technologists. Implants with just the right size, distribution, and interconnectivity of pores can tremendously help in osteointegration [51]. This is where the bone tissues and muscles can grow through the induced or controlled pores to offer more reinforcements to the implants. This type of implants is reported to have better mechanical properties with reduced density and also reduces the risk of bacterial infection [1]. Plaster molds with unique designs are easily fabricated with techniques such as SLS, SLM, and EBM. These aid dentists in creating an identical teeth mold for each patient's' teeth [2].

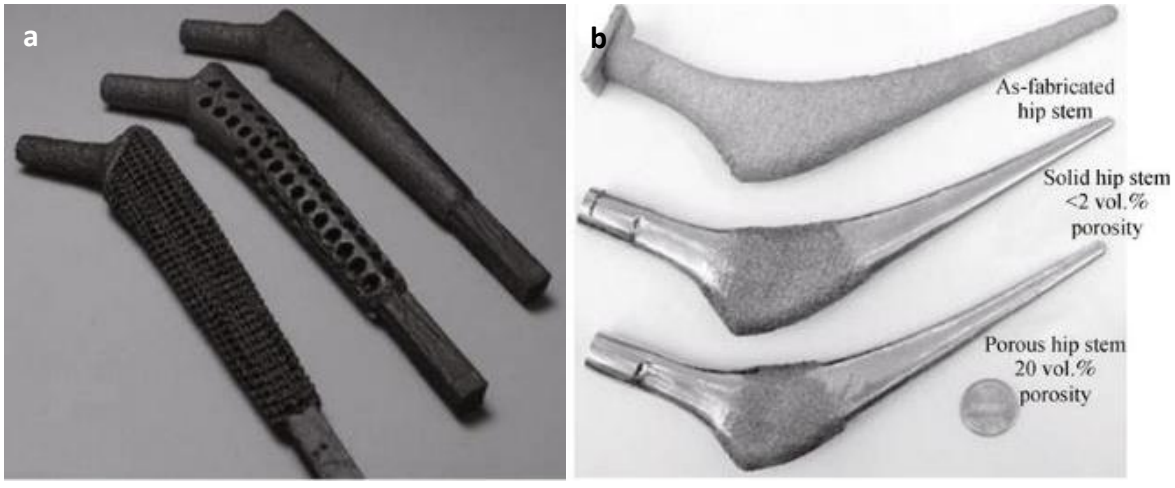

Figure 2-12: Hip stems designed with controlled porosities using a)EBM b)LENS[1]

2.3.4 Prototyping and research purposes

Research institutions have investigated the MAM technology for a while trying to determine the resulting behavior of the parts made by these technologies. Also, testing methods and experiments are designed to be repeated for easy characterization of MAM parts. Most of the research into comparing the methodology and results of various MAM process come out from universities. These studies are detailed in section 2.6.

2.4 Challenges of Metal-Additive Manufacturing

There many benefits such as the possibility to print complex structures, customization, and ease in designing parts. However, metal AM still has many challenges before being entirely implemented into all real-world applications. Parts processed using this manufacturing technique are riddled with many defects and discontinuities which affect the integrity of the printed part. Defects such as porosity, that compromises the load-bearing capacity and cracks resulting from residual stresses are induced during the printing of the parts [1]. Also, the presence of non-equilibrium phase changes because of the irregular and repetitive thermal cycles during the printing process makes it very difficult to predict the mechanical and material properties of the printed part [2].

2.4.1 Printing Parameters

Printing parameters can be grouped into two main categories; laser control parameters and material control properties. Laser control parameters involve the manipulation of the laser properties or laser position which includes power, speeds, hatch spacing, beam diameter, point distance, exposure time, modulation of laser wave, scan strategy, etc. The material control parameters include layer thickness, size distribution, material alloying, etc. All these parameters can affect the material integrity. Mostly these parameters are the various ways that defects in the material are controlled. Studies on Metal-AM have shown that there are over 130 printing parameters that affect the structure of the final part which include laser power, scanning speed, laser spot size, layer thickness, scan pattern, etc. [18]–[20] These parameters are found in the printing machines that have adopted the laser powder bed fusion technology for metal additive processing. However, detailed studies on how these printing processes and parameters affect the final microstructure and other printing-induced defects are still being carried out. The most critical parameters of the laser powder bed fusion technology that requires little to medium level of expertise to manipulate and dictates the final microstructure

are laser power, layer thickness, scan speed and hatch spacing between the scan lines. A list of studies that have been done on the effect of printing parameters on the microstructure of 316L stainless steel is shown in Table 2 1.

Table 2-1: Printing parameter combinations for getting optimized parameters for printing [52]

Stainless steel 316L	P(W)	v(mm/s)	t(mm)	h(mm)	E (J/mm3
Kamath et al. (2014)	150-400	500-1800	0.03	0.15	28-74
Li et al. (2012)	190	800	0.05	0.15	32
Miranda et al. (2016)	50-100	300-1250	0.03	0.070-0.140	32-80
Spierings et al. (2010),	104	175-800	0.030-0.045	0.13	33-107
Spierings and Levy (2009)					
Kruth et al. (2010b)	100	175-380	0.06	0.126	35-76
Yasa et al. (2009)	85-105	300	0.020-0.060	0.112-0.125	38-156
Yusuf et al. (2017)	200	1600	0.05	0.06	42
Liu et al. (2011)	50	100-300	0.05	0.08	42-125
Casati et al. (2016),	200	750	0.05	0.11	48
Yakout et al. (2018a)					
Kruth et al. (2010a)	105	380	0.020-0.040	0.125	55-111
Dadbakhsh et al. (2012)	87	150	0.075	0.13	59
Kurzynowski et al. (2018)	100-200	200-220	0.05	0.124	81-150
Yadroitsev and Smurov (2010)	50	120	0.04	0.12	87
Yasa et al. (2010)	100	300	0.03	0.081-0.126	88-137
Yasa (2011)	100	300	0.03	0.112-0.125	89-99
Sun et al. (2016)	380	625-3000	0.05	0.025-0.120	99-109
Liverani et al. (2017)	100-150	700	0.02	0.050-0.070	102-214
Saeidi (2016)	190	800	0.02	0.1	119
Yadroitsev and Yadroitsava (2015)	50	100	0.05	0.07	143
Liu et al. (2016)	200	400	0.04	0.08	156
Yadroitsava and Yadroitsev (2014)	50	100	0.05	0.06	167
Shifeng et al. (2014)	180	900	0.02	0.06	167
Yadroitsava and Yadroitsev (2015)	50	10	0.04	0.07	179

Also, these are the parameters that can easily be changed without voiding the warranty of a Metal 3D printer which is very expensive. The energy density (specifically the volumetric energy density) combines these three influential parameters into a single expression to compare these process parameters on the microstructural integrity of the final part [8], [52], [53].

2.4.2 Porosities

Porosity can be a good or undesired property in a part depending on the application of the part. Even if the application requires a porous component, being able to control the formation and sizes of the final printed part is very crucial. Porosity is very characteristic of additive manufacturing and is attributed to several factors. Porosity can be process-induced or as a result of trapped gas that could not escape fast enough before solidification occurs.

Process induced pores are also referred to as Lack of fusion pores (LOF) which are formed as a result of low energy input delivered to the powder to achieve complete fusion. This can happen by lower laser power, very fast scanning speeds or lack of overlap between the scan pattern (high scan spacing)[34][54]. These types of pores/voids/holes contain unmelted powders that did not completely fuse to each other. A typical LOF can be seen in Figure 2 14 below. LOF pores are seen as a lack of bonding between two adjacent scan tracks or build layers. The presence of unmelted powders confirms the lack of overlap between two adjacent scan tracks [55]. Also, when two layers do not bond properly because the energy input delivered was not enough to penetrate deeper through the first layer to the one beneath to fuse the layer together, interlayer bonding will not occur properly [34][54]. LOF pores can, therefore, be seen mostly between laser scan tracks and layers [30]. The interlayer bonding defect can propagate to the surface creating a multi-layer defect. Some LOF pores are covered up with subsequent layers and hence cannot be detected by surface analysis techniques. These cases can sometimes be detected by an Electron Dispersive X-ray Spectrometry analysis by exposing areas rich in oxygen [56].

Porosity is very rampant when using metal powders with very low packing densities which leaves huge spaces in-between the particles. These spaces are then filled with gas that gets trapped in the molten metal pool and cannot escape fast enough to the surface [30]. Gas can also be trapped in the molten pool due to vaporization at higher energy densities. The process by which the metal powders are produced such as gas atomization can also introduce gas into the metal powder [30]

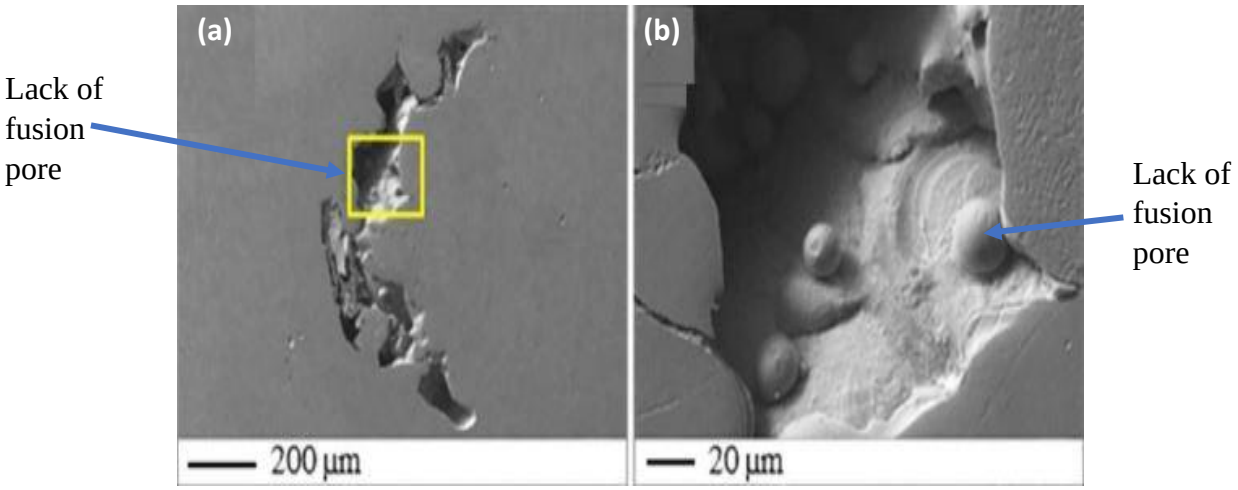

Figure 2-13: Lack of fusion pores a)at low magnification b)at high magnification revealing unmelted powders[30]

A lot of explanations as to how gas pores are formed have been proposed by researchers lately. Gong et al attribute the formation of gas pores to very high laser energies that cause vaporization of low melting point alloy constituents in the molten pool that gives rise to the gaseous state of the molten metal getting trapped in the pool. After the molten metal solidifies, these gas a trapped, sometimes, underneath the surface [57]. It is, however, believed across the field that gas-induced pores are specifically spherical in shape and are enriched in oxygen as seen in Figure 2 15. These types of pores are difficult to entirely get rid of, even if they are not visible on the surface does not mean that they are not underneath the layers.[30].

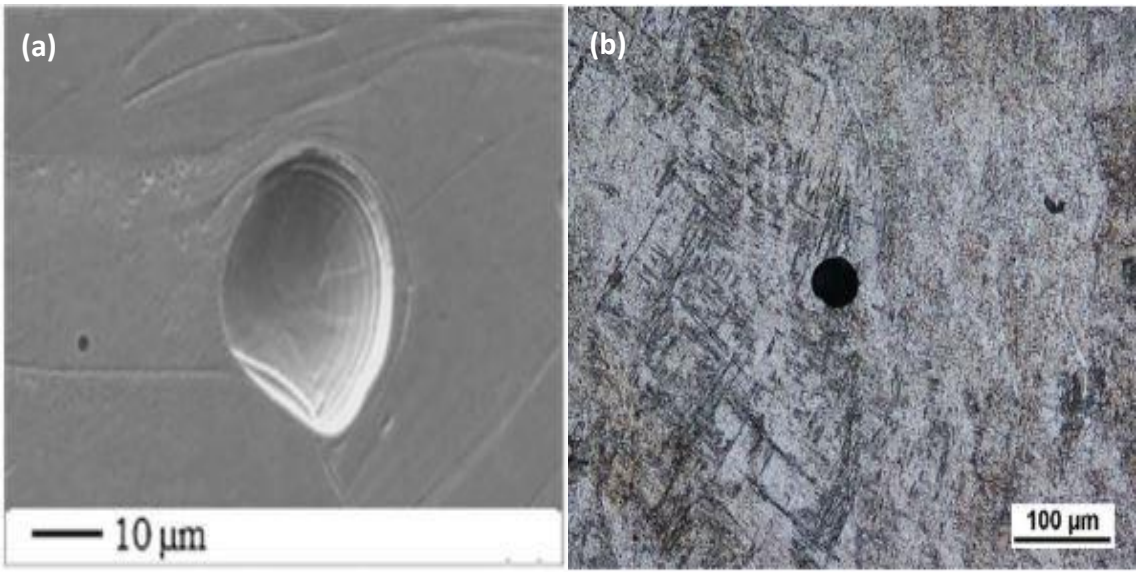

Figure 2-14: Spherical gas pore in a) 316L-SLM part[55] Ti-6Al-4V-EBM part[35]

2.4.3 Residual Stresses

Residual stresses are characteristic of metal 3D printing due to the huge thermal gradient as a result of the rapid cooling and rapid solidification. Thermal stresses coupled with the high thermal gradient are induced into the part after printing and when left unattended cause cracks to emanate in the sample [58][59]. When the cracks are initiated, they grow into the whole part in due time and that comprises the integrity of the part. Cracks can form along with the grain boundary or through grain themselves.

The cracks along grain boundaries are called intergranular cracks whereas crack through grains is transgranular cracks which bring about intergranular and transgranular fractures/failures respectively. Metal alloys with low thermal conductivity experience thermal stresses very strongly since the thermal energy accumulated during the printing process cannot easily dissipate, which makes them very susceptible to cracking. Examples of these types of cracks are shown in Figure 2 16. Such material includes stainless steel and nickel-based alloys [60], [61]. This phenomenon is reduced by preheating the substrate to try and create a uniform thermal distribution.

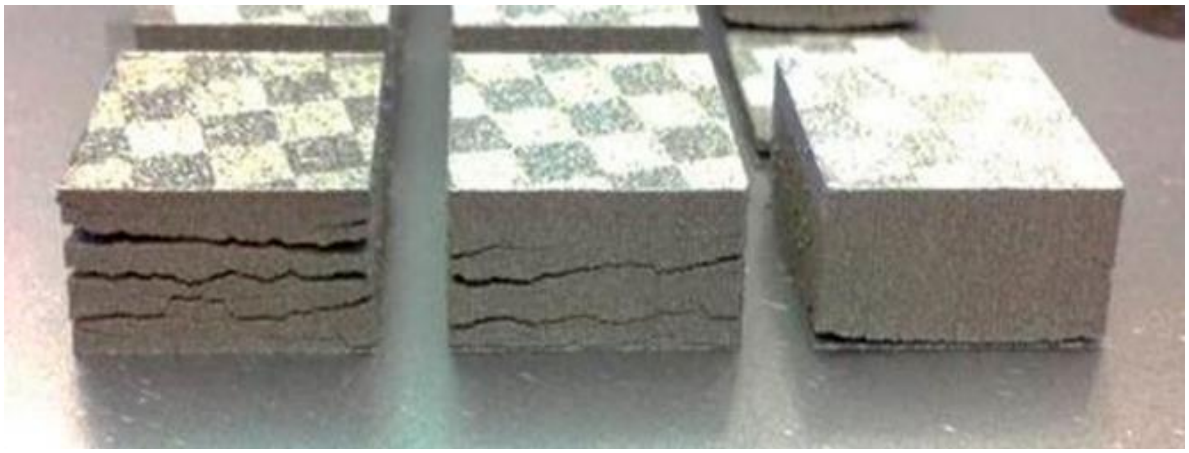

Figure 2-15 Cracking between layers in M2 Tool Steel[62]

2.4.4 Non-equilibrium Microstructures

Using various MAM techniques to fabricate parts changes the microstructure from structures that are induced with traditional manufacturing technologies. Steel MAM shows a lot of these microstructural changes with the introduction of new solid phases as well as micro-segregation of the sub-particles. These phases and microstructures are not present when traditional methods are used to produce parts with the same chemical composition. These new microstructures that

evolve change the properties from the know behaviors that have been recorded. Steel is among the most researched material for MAM parts fabrication and as all other metal used in AM, experience the same microstructural inconsistencies. Typically for steel AM parts, there are fine-grained structures that form due to the high cooling rates present during the manufacturing processes[63][64]. The microstructure changes that occur can be a super-structure such as a melt pool boundary a substructure like cellular and columnar structures, as well as secondary phases that form as the changes in temperatures occur during manufacturing [65] [66]. Also, grains that orient in a specific direction has been reported in MAM steel parts that create texture and consequently cause anisotropic property behavior. The LMD technologies are known to be susceptible to thicker melt pools boundaries which shows broadening microstructures due to slow cooling rates [63], [64]. Texture develops in the microstructure due to the parameters that were used in the fabrication processes[67]–[69]. Due to the thermal cycles experienced by a part that is additively manufactured, some alloying metals under phase transformations. This evolution that the microstructure goes through changes the properties entirely from its initial properties. The transformations that happen during the printing process is dependent on the type of AM used to fabricate the part. The microstructure shown in Figure 2 18 is that of a 316L Stainless Steel that is manufactured by LENS technology. This microstructure reveals the presence of intercellular ferrite on the boundaries of the cellular dendritic structures [38].
Austenitic stainless steel is known to entirely consist of a single-phase microstructure, however, most of the MAM fabrication techniques used introduces a second phase microstructure that changes the behavior completely but SLM technique [70][71]. After fabrication 316L and 304L steels are observed to be dominated with cellular and columnar dendritic structures based on the printing process parameters and the type of MAM technique employed [5]. Second phase particles particularly, ferrites are reported when using DED techniques for part fabrication [5]. Due to the low content of carbon in these types of alloy, precipitated carbides are not common in the final parts.

For martensitic steels, small volumes of ferrites are introduced after they have been additively manufactured. The same microstructure has been observed for precipitation hardening steels such as maraging steel, AISI 420,17-4 PH, etc. [63], [64], [68] A list of steel parts fabricated by various AM techniques and the different phases that are reported are shown in Table 2-3.

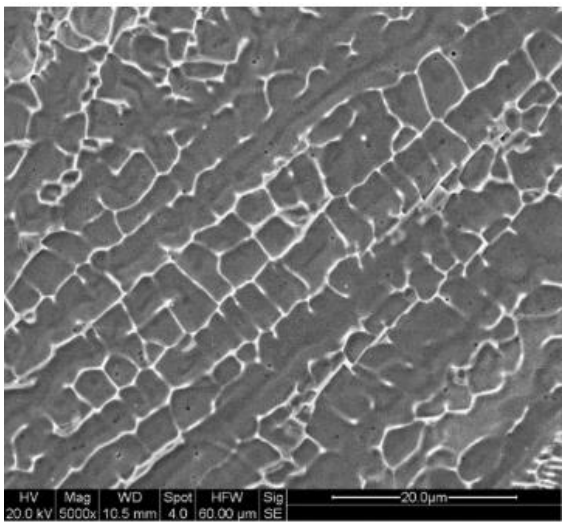

Figure 2-16: Microstructure of 316L Steel fabricated with DED showing cellular dendritic structures[5]

Table 2-2: Various MAM techniques and the different kinds of phases it induces in the final parts made of Iron Alloys [5]

Alloys	MAM techniques	Phases reported in studies	References
4340	DMD	Ferrite, Cementite, Martensite	[73]
316L	LENS	Austenite, intercellular ferrite	[36]
316L	GMA-AM	Austenite, sigma, delta ferrite	[74]
420 SS	DMLS	Martensite, Austenite	[75]
ER70S-6	3G-GMAW	Ferrites (polygonal and acicular)	[76]
FeCrMoVC	SLM	Martensite(fine), austenite, carbides	[77]
H13	EBM	Martensite	[78]
H13	DMD	Martensite, fine carbides, retained austenite	[79]
M2 Steel	DMLS	Austenite, Martensite, Carbides	[80]
Maraging Steel	SLM	Not reported	[81]

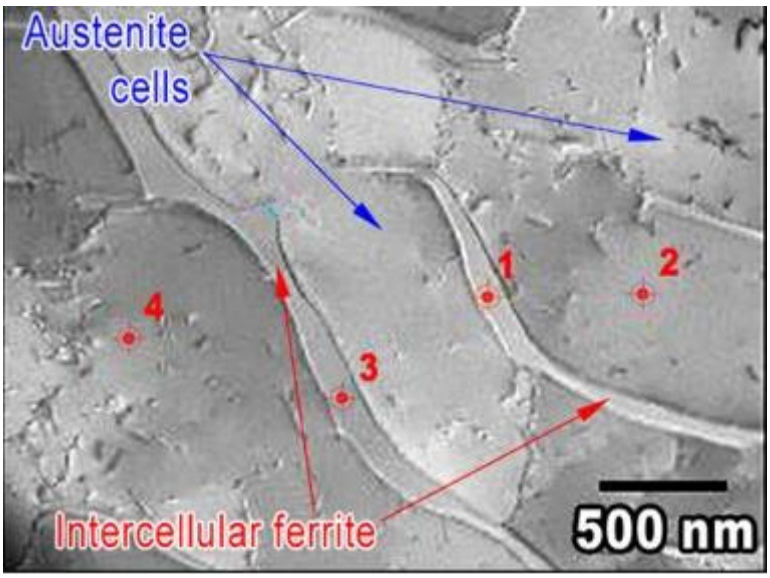

Figure 2-17: Presence of ferrite in Austenitic Stainless Steel produced with LENS (316L)[38]

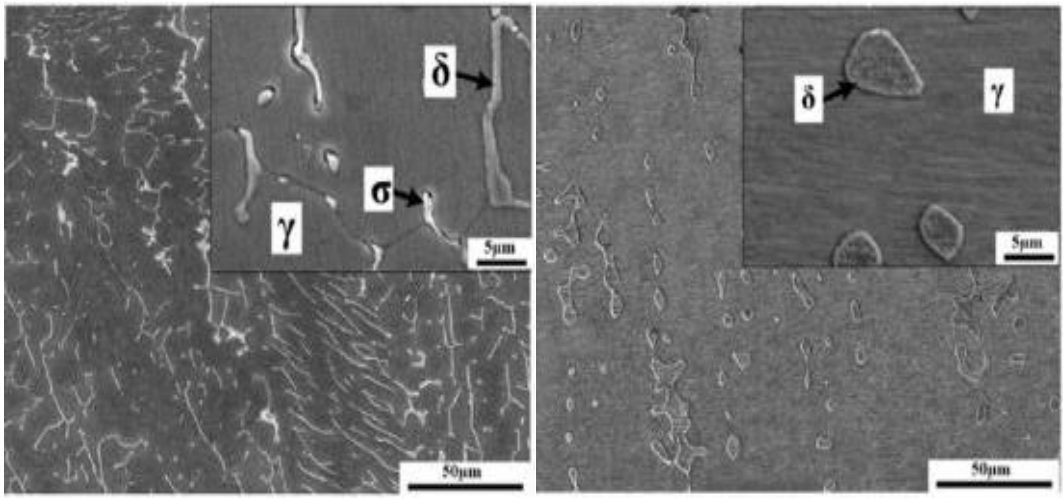

Figure 2-18: Sigma and delta ferrite in 316L produced with Arc AM[74]

Chen et al made a study to investigate the microstructure changes that occur in 316L that are fabricated using arc additive manufacturing technique and discovered different phases present. The austenite matrix, the intermetallic phase (sigma, which is metastable at room temperature). The sigma phase is reported to be a strengthening phase but at the same time, it depletes the ductility of the structure. The microstructure from this study showing the various secondary phases are illustrated in Figure 2 19.

2.5 316L Stainless Steel Alloy

Steel is used in almost all fields of engineering, from food processing to using them in nuclear power plants. This is mainly because of its high performance and material properties [68]. Steel has also found favor in MAM technologies [28]. Steel alloys are among the most researched metals used in MAM aside from titanium alloys. Commonly available steel grades used for MAM purposes include austenitic steels, precipitation hardenable steels, maraging steels,630 steel,15-5 PH steels, tool steels, etc. [63]. Austenitic steels that are used more often include 304L and 316L since they are low carbon steels that are resistant to corrosion due to their low carbon contents [28]. The 316L Stainless Steel is a single-phase austenitic stainless that is used most often in areas that require a material with high strength and corrosion resistivity. This variant of low carbon steel has numerous properties that influence its wide uses [72]. 316L SS maintains its high creep and tensile strength at elevated temperatures. Also, 316L is biocompatible and can be used as medical implants as well as surgical tools. Because of all these properties, these steels are being used in the oil and gas industries to processes corrosive chemicals.

Table 2-3: Chemical Composition of 326L Stainless Steel Powder from EOS

Element	**Composition (%)**
Fe	Balance
Cr	17.00/19.00
Mo	2.25/3.00
Ni	13.00/15.00
Mn	2.00
Cu	0.50
C	0.030
P	0.025
Si	0.75
S	0.010
N	0.10

They are seen in the food processing and pharmaceutical plants because they do not easily corrode and leak dangerous elements into the food or medicine. Due to their polished nature after surface treatment, they appeal to the architectural industry to be used in creating astonishing structures. They are used in making parts of ships that are susceptible to corrosion by the seawater and are used to build structures close to the sea due to the amount of salt in the atmosphere that can easily corrode other types of metal alloys. The 316L SS used for this study has a chemical composition listed in Table 2-4.

2.1 Printing Parameters effect on Laser Sintered 316L Microstructure

PBF as discussed earlier involved a layerwise fabrication of a part [82]. It involves a single scanning using a laser of specific power (P/W) moving at a constant speed, v (mm/s). A layer is completed by multiple scans depending on the type of scan strategy used. The distance between adjacent scan lines is referred to as the hatch spacing, h (mm). A new layer is started after new material is deposited onto the previously completed layer, and the height of the deposited material is the layer thickness, t (mm) [8]. A single expression is derived from a combination of these four important printing parameters to evaluate part density, porosity, surface roughness, etc. which is the volumetric energy density (VED)[83]. Materials such as 316L steel have been successfully printed by Selective Laser Melting technology(SLM) to achieve a 99.9% densification in 2010 [84]. However, the microstructural integrity of the part as a function of the printing parameters have been unpredictable[84]

$$\mathrm{VED} = \frac{\mathrm{P}}{\mathrm{v} \times \mathrm{t} \times \mathrm{h}} \tag{2.1}$$

Kamath et al. investigated the densities of 316L AM parts using 150W-400W laser power and concluded that the part densities are affected in two ways, insufficient melting and keyhole mode. For the insufficient melting, either the speed is increasing, or the laser power is reducing (at low powers). The keyhole mode occurs when the laser energy is too high and that results in lower densities as well. Also, Kamath and his group found out that the speed sensitivity is dependent on the intensity of laser power used. According to them, using high laser power causes negligible variation in part density when the scan speed is changed. High laser power gives the same densification over a wide range of scan speeds but at lower laser powers, the density varies significantly with change in scan speed [18].

Yakout et al studied the densification and mechanical behavior of 316L Stainless Steel Alloy using 200W laser power and suggested a stable energy density range between 62.5-104.2 J/mm^3. According to Yakout and his group, this range of energy density provides better densification, reduced level of voids and defects and highest toughness behavior [52]. Kruth et al assessed the effect of laser re-melting with further part densification. They provided us with optimized printing parameters which are 380 mm/s speed, 105W laser power, 125 um hatch-spacing and spot size of 200um (energy density of ~ 76 J/mm^3) which gives maximum densification at 0.77% porosity level and by re-melting porosity reduces significantly to 0.032%. But J. A. Cherry et al after conducting research on Laser melting on 316L Stainless Steel achieved that the lowest porosity which was recorded at 0.38% occurred at an energy density of 104.52 J/mm^3. The parameters that were studied are point distance and exposure time. Also, they concluded that the amount of porosity present in the sample affects the hardness of the material. The maximum hardness recorded for this started was at 225HV with an energy density of 125 J/mm^3 [85].

Metal-based Additive Manufacturing (AM) techniques such as the SLS is currently being used to produce complex metallic and high-performance parts for use in high-stress applications in the aerospace and automotive industries. However, there is no widespread use of AM processes for direct part production in these industries because of various concerns including gaps in performance metrics, standards to improve the accuracy of AM parts and lack of consensus on properties of produced parts [21]. Also, processing parameters and constituent powder materials produce microstructural heterogeneities which influence the properties and quality of parts fabricated via AM [21], [22].

Currently, Metal-based Additive Manufacturing (Metal-AM) techniques such as Direct Metal Laser Sintering (DMLS) is being used to produce complex metallic and high-performance parts for use in the aerospace, biomedical and automotive industries. However, strict requirements for part quality and standards have prevented widespread use of AM processes for direct part production in these industries. This is attributed to various concerns with AM parts including quality and repeatability of produced metal parts, gaps in performance metrics and standards to improve the accuracy of parts. Understanding the effect of processing parameters on the evolution of microstructural heterogeneities which influence the properties and quality of parts fabricated via AM, can be used to tailor the microstructure of parts for specific applications. In

this study, the effect of DMLS parameters on part quality and microstructural evolution is studied as a baseline for tailoring the microstructure of parts for a specific application.

2.2 Mechanical Properties of 3D Printed 316L Steel

Printing parameters and microstructural features play an essential role in the mechanical response of the 3D printed 316L steel for various applications. Mechanical testing such as hardness and wear test are discussed in this section.

2.2.1 Hardness

Hardness as a mechanical property is a measure of the resistance to the localized plastic deformation when a load is applied to the metal. This is normally determined when a flat surface is impacted with an indent of a predefined geometry. Vickers hardness test, which was developed in 1922 by the engineers at Vickers Ltd is the most commonly used form of micro-hardness testing[86]. Various Vickers hardness equipment has different loads ranging from 25gf to 400gf (2N-490N) are equipped. The diagonals from the square-based pyramidal impression made on the surface with a specific load are measured and the area under the indent is used to estimate the hardness of the metallic surface using the equation (2.2) below. The schematic for the hardness test is shown in Figure 2 20.

$$HV = 0.1891 \times \frac{F}{d^2} \tag{2.2}$$

Where F = the applied load (N)

d = average of the two diagonals

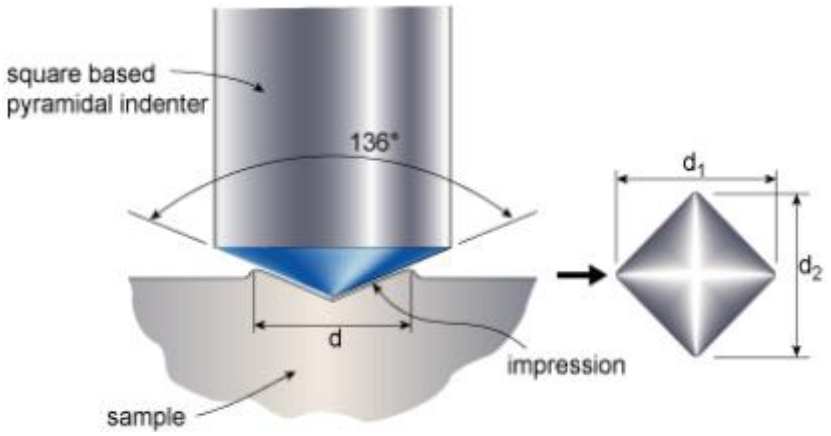

Figure 2-19: Schematic representation of the Vickers hardness process

There have been several types of research done that relate the hardness to the porosity of the printed sample [85], [87]. However, Zuback et al found no relation between the micro harness and part densification but attributed the hardness of the part to the variation in hatch spacing which plays a big role in the cooling rates [5]. Other studies also confirm no correlation of hardness with part density [35][88].

2.2.2 Tribological Behaviour of 316L Stainless Steel Alloy

The phenomenon of rubbing surfaces has been in existence since the stone age. “Tribology” was first introduced by the Jost when he reported on his landmark in 2006 [89]. The term Tribology was derived from the Greek word “tribos”, which means rubbing and therefore in simple terms defined as the “science of rubbing” [90]. Tribology is, therefore, the study of the science and engineering of the relative motion of contacting surfaces. Since the twentieth century, it has been developed to include the study of friction, wear, and lubrication of interacting surfaces [91]. Specific applicable fields of tribology include biomedical, automotive, aerospace, etc. Poor wear resistance and galling wear are characterized in most stainless steel including AISI 316L Stainless steel. They are usually prone to different forms of wear and contact damage due to their soft nature and limit their applications [92].

2.2.3 Friction and Coefficient of friction

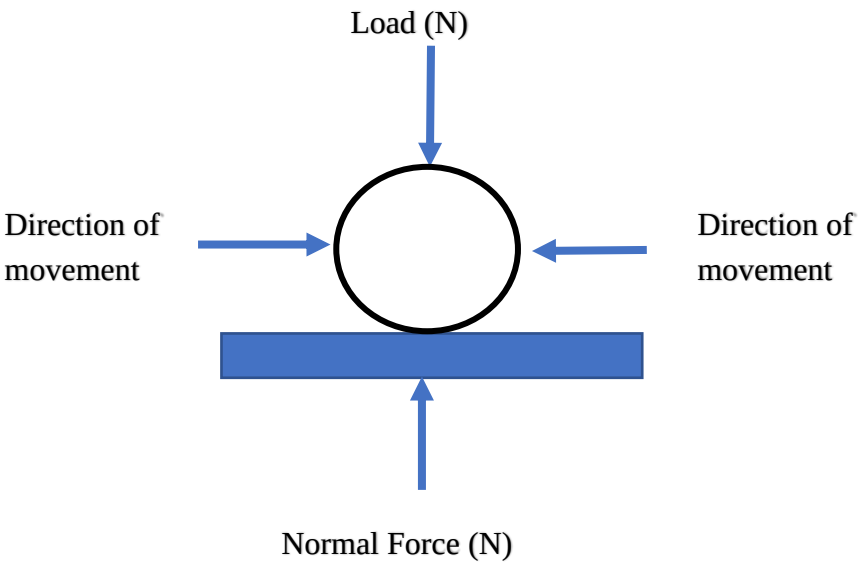

Figure 2-20: Schematic of friction on a sliding body

Friction is defined as the resistance to the relative motions of two bodies in contact. Friction is essential since it exists ideally in every form of a mechanical system. The mutual contact between two surfaces sliding against each other will experience a frictional force. This force is due to the resistance that is tangential to the contact surfaces of the sliding bodies. Figure 2 21 shows that the frictional force is experienced in the opposite direction of the sliding.

The frictional force is also related to the applied normal load, the contact area and surface features such as asperities and roughness. The term coefficient of friction (μ) is generally defined as the ratio of the maximum frictional force(F) between the two surfaces and the normal force applied (N). The mathematical expression of the coefficient of friction is given in equation (2.3) below:

$$\mu = \frac{F}{N} \tag{2.3}$$

2.2.4 Wear

Wear can be defined as the progressive removal of material from the surface of two materials in contact and relatively moving against each other. Wear can also be described as the level of plastic deformation occurring on a surface as a result of the mechanical action induced by the constant sliding actions [93]. These normally occur in mechanical processes such as machining, grinding, cutting and even polishing. Wear can be both desirable and undesirable in a system. Constant and excessive wear is most undesirable in many engineering applications leads because it leads to the deterioration and sometimes catastrophic failure of most components. The degree of wear of surfaces is normally quantified using wear rate. Wear rate is defined by the mass or volume loss of material per unit sliding distance. However, most wear rates are expressed in simple terms using mass loss (g) and volume loss(mm^3). The rate of wear of two surfaces is influenced by many factors. The type of material, geometry of contact surface, macroscopic and microscopic irregularities, surface roughness, atmosphere, and operating conditions highly affect the wear performance of parts in service.

2.2.5 Wear Mechanisms

Due to the nature of the contact surface and their interactions, different wear modes can be experienced on the surfaces of the materials. These wear mechanisms can act alone or

simultaneously on the surface and can be grouped as follows: adhesive wear, abrasive wear, surface fatigue, and tribo-chemical wear. Figure 2 22 shows the wear mechanisms experienced on various metal surfaces including stainless steel: Another prevalent wear mode is fatigue wear which results in surface crack formation due to the repeated sliding cycle of the contact surfaces, as shown in Figure 2 22c. These cracks break-up eventually and result in loss of material from the mating surfaces. Corrosive or oxidative or tribo-chemical wear occurs as a result of chemical interactions between the mating surface and the environment. This mode of wear is also demonstrated in Figure 2 22d which shows the formation of chemical products on the mating surface. These products can be regarded as protective layers but are easily worn as sliding continues, to expose the surface for material loss [94]. The medical industry has embraced this new manufacturing technology, 3D printing, for the huge advantage it offers to the field. From building custom implants to designing intricate surgical tools, additive manufacturing is revolutionizing the industry. It is very crucial that the toxic chemical component of the materials used in these tools do not leak into patients' bloodstreams. This results in the need to access the tribological performance of such materials.

For 316L steel, the nickel content is toxic if leaked into the bloodstream, so it is very prudent to access the wear properties of these parts printed with 316L Steel.

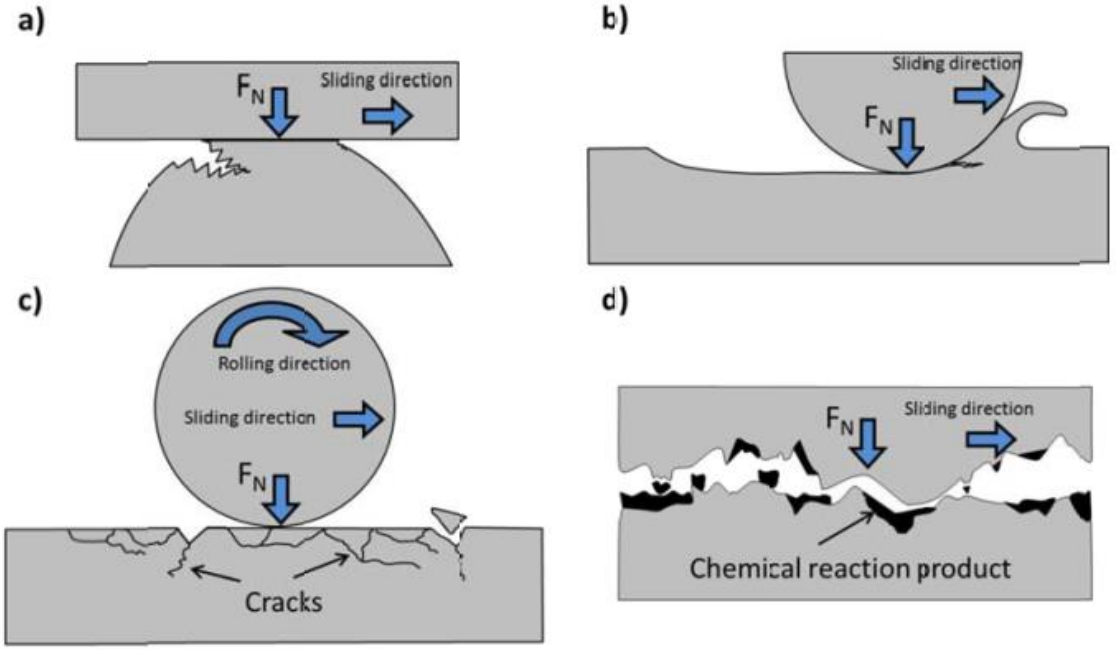

Figure 2-21: Schematic representation of wear mechanisms (a) adhesive (b) abrasive (c) fatigue wear (d) corrosive wear[95]

Y Sun et al did some work with testing the wear behavior of 316L steel. They performed a dry sliding reciprocating wear test and concluded that the denser the fabricated part, the more resistance it is to wear which ultimately means that sintered parts are not as resistant to wear as bulkier more dense part fabricated by conventional or traditional means. The 316L-SLM parts fabricated with different scan speeds in their study were able to achieve the lowest part porosity of 1.7% and a high porosity level of 6.7%. This study also concluded that a denser part will be more resistant to wear than a porous part [96]. However, some studies conducted on SLM fabricated 316L showed that they had better wear properties than conventionally manufactured parts. SLM better wear property.

Bartolomeu et al [97] compared the wear properties of parts fabricated by SLM, casting and hot pressing technology. A single SLM part with 70 W, a scan speed of 417 mm/s, hatch spacing of 70 µm, and an optimum layer thickness of 30 µm obtained from studies on printing parameters optimization [98], [99]. Among these three technologies used to create the tested specimen, the SLM part showed the highest wear resistance at a 28% lower wear rate that the casted specimen. These studies compared the wear behavior additively manufactured part to conventionally manufactured 316L SS. However, the studies into the effect of printing parameters on the wear behavior are still being explored. Li H. et al investigated the influence of parameters such as build direction on the COF and consequentially the wear rate. The effect of temperature on the wear rate was also investigated.

Li et al found out that the build direction has a negligible influence on the wear rate and COF but at high temperature, say 200^{o}C, the COF decreased greatly [100]. In adhesive wear as shown in Figure 2 22a, materials on the contact surfaces stick or adhere to each other due to the formation of bonds between the asperities of the sliding surfaces. This eventually leads to material transfer between the two surfaces and the loss of material from the contact surfaces as the load is continuously applied. Abrasive wear is characterized by the rubbing action of a softer surface with a harder surface. Surface asperities of the harder material cause flow or plowing of the softer material or more ductile material. When there is just an abrasive slide along one of the surfaces, it is termed as two-body abrasive wear. When a hard particle is caught between the mating surfaces and plows the softer surface, then we have third-body wear [94]. A schematic of the abrasive wear is illustrated in Figure 2 22b.

3 METHODOLOGY

3.1 Introduction

The samples are first 3D printed using varied printing parameters and then studied extensively to characterize their behavior based on two categories. After the samples were printed, they are taken through two different forms of studies: the microstructural and mechanical characterizations. The microstructural investigation involved density measurements, a surface morphological analysis that involved analyzing porosity, unmelted powders and the evolution of microstructural features. The mechanical characterization involves determining the hardness and the wear performance of the printed parts. The overview of the experimentations is shown in Figure 3 1 & 3 2.

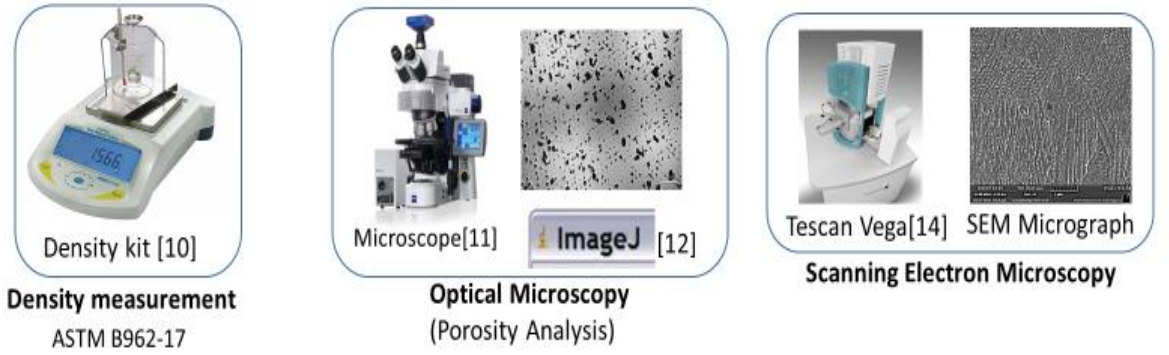

Figure 3-1: Microstructural Analysis of 3D-printed Samples

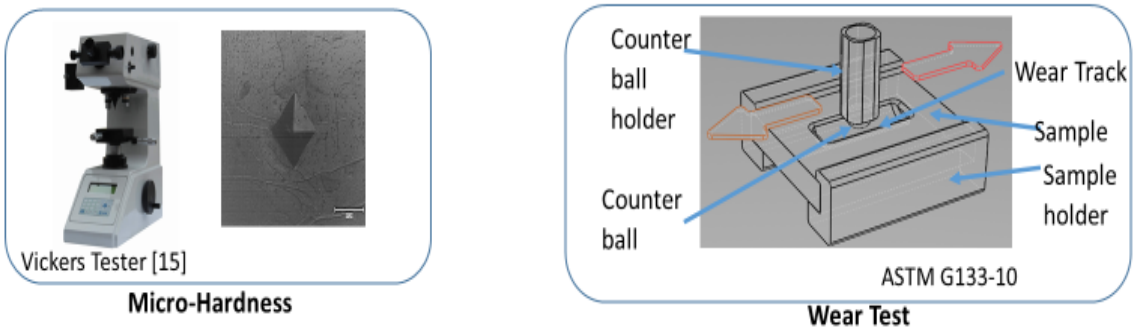

Figure 3-2: Mechanical Behaviour Testing of 3D printed Samples

3.2 Sample Processing

Figure 3-3: M280 DMLS Printer from EOS[101]

The steel powder used to print the samples has an average particle size of 55 μm based on a mill certification test conducted by Electro Optical Systems based out of Finland. The various parameters used to fabricate these samples are shown in Table 3-1. The parametric values were selected to be within the range that has been described in a review of laser sintering of 316L steel paper by Yakout et al [52]. From Table 3-1, there are three different laser powers 150, 200 and 250W. Each sample is printed with varying hatch spacing (0.08, 0.10, 0.12 and 0.14 mm) and laser scan speeds (250, 750, 1250 and 1750 mm/s). The hatch spacing that is used and the potential overlap or offset between the beam diameters of the scan lines are shown in Figure 3-5 & 3-6. Square cuboids, measuring 20 mm x 20 mm x 15 mm, were fabricated in a chamber filled with nitrogen gas with a substrate temperature of 375 K. Fifteen samples with different printing parameters were manufactured using a commercially available printer EOS M280 DMLS machine shown in Figure 3-3 using appropriate AISI 316L stainless steel. The scan pattern used to create the sample is referred to as a stripe scan pattern shown in Figure 3-4. The stripe patterns are rotated at by 67^{o} for every layer of the samples produced. The entire details of the scan patterns as portrayed by Yakout et al [52] is shown in Appendix D. The nomenclature of the sample is explained with the diagram shown in Figure 3-7.

Table 3-1: Printing parameters for AISI 316L Alloy

Group P1=150W					
Sample	G2B1	G2D1	G4A1	G4C1	G4D1
Hatching spacing(mm)	0.10	0.10	0.14	0.14	0.14
Scan speed(mm/s)	750	1250	250	1250	1750
VED (J/mm^3)	66.67	28.57	142.86	28.57	20.41
Group P2=200W					
Sample	G1B2	G1C2	G2B2	G3C2	G4B2
Hatching spacing(mm)	0.08	0.08	0.10	0.12	0.14
Scan speed(mm/s)	750	1250	750	1250	750
VED (J/mm^3)	111.11	66.67	88.89	44.44	63.49
Group P3=250W					
Sample	G1C3	G3C3	G3D3	G4B3	G4D3
Hatching spacing(mm)	0.08	0.12	0.12	0.14	0.14
Scan speed(mm/s)	1250	1250	1750	750	1750
VED (J/mm^3)	83.33	55.56	39.68	79.37	34.01

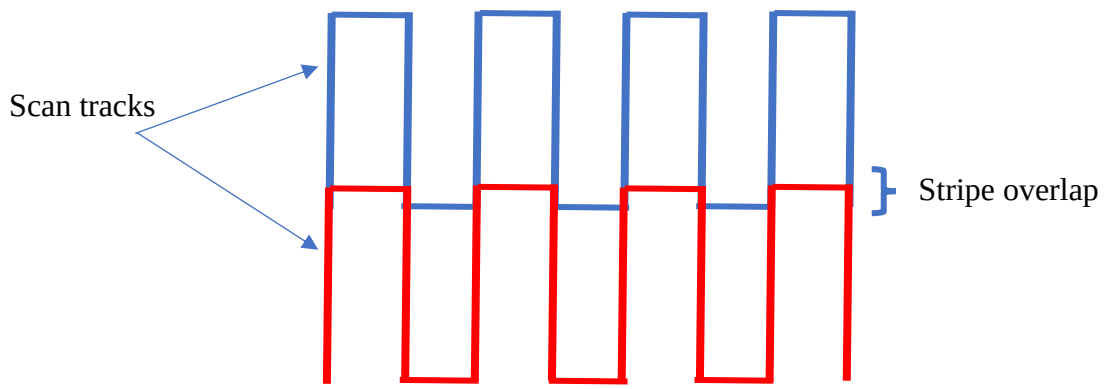

Figure 3-4: Stripe Scan pattern

-

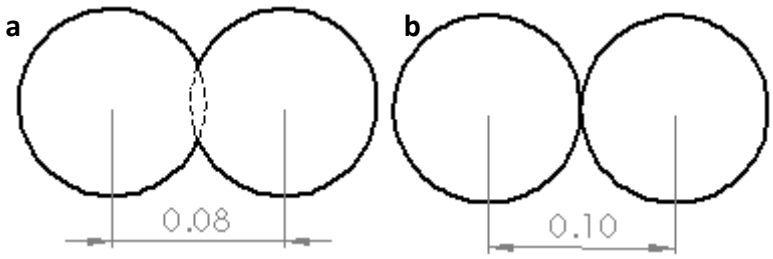

Figure 3-5: Hatch spacing with an overlap of a) 20 µm b) 0 µm

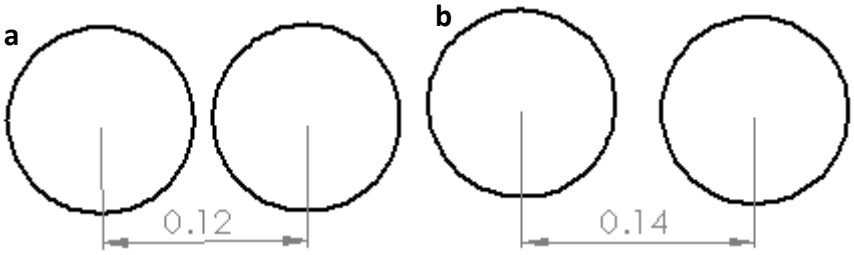

Figure 3-6: Hatching spacing with an offset of a) 20 µm b)40 µm

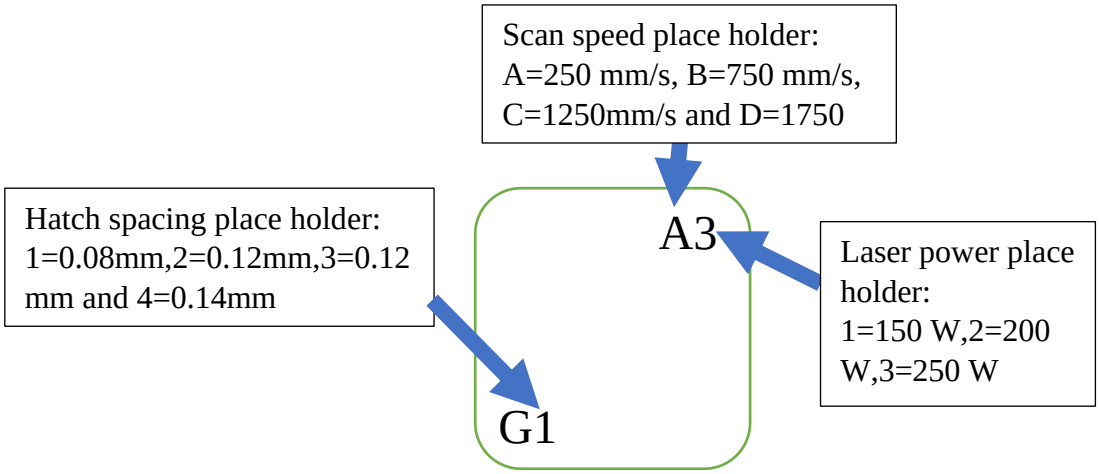

Figure 3-7: Nomenclature of Samples for Identification

3.3 Surface Preparation and Microstructural Characterization

The samples after printing are shown in Figure 3-8 with the dimensions shown with the help of a Vanier caliper in Figure 3-8b. A 5 mm thickness of the sample was cut from the bottom part of each cuboid with a wire Electric Discharge Machine (EDM). 5mm piece was taken from the bottom part of the whole sample as shown by the schematic diagram in Figure 3-9. The 20 x 20 x 5 mm cut pieces were hot mounted at 190^{o}c and 260 bars using the automatic mounting press from MetLab mounting shown in Figure 3-10a.

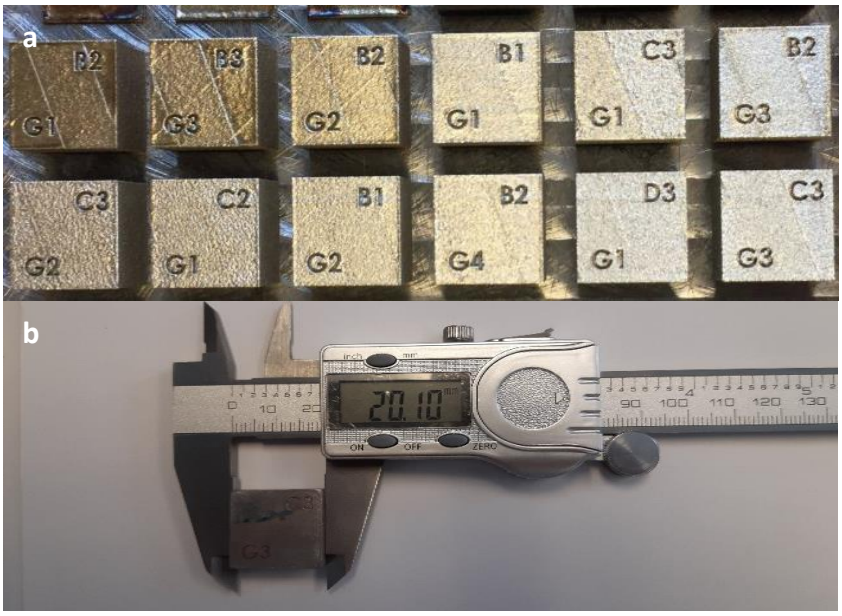

Figure 3-8: a) Sample Coupons after printing b)Dimension of sample coupon

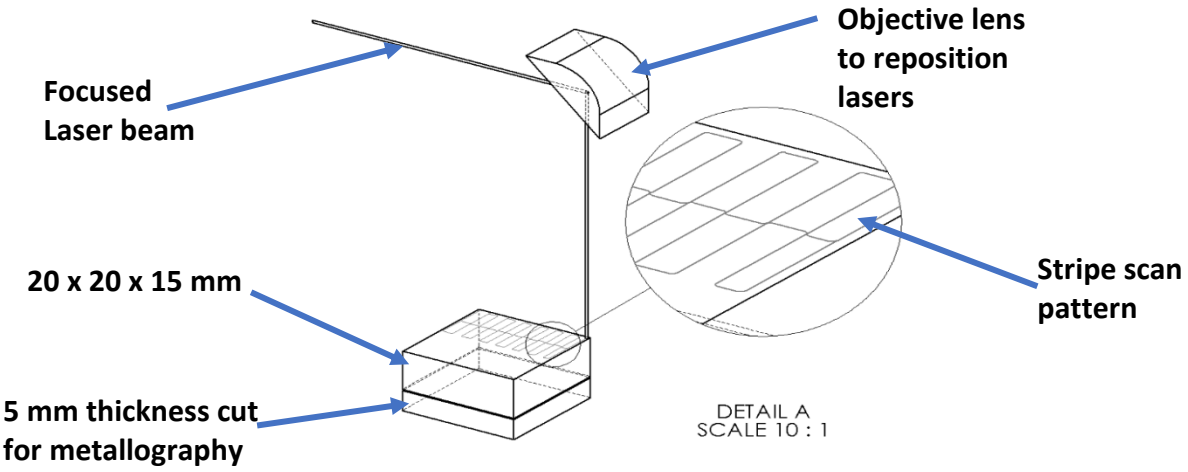

Figure 3-9: Cut part from the bottom of the sample

The mounted samples (one of them shown in Figure 3-11) were grounded with SiC grinding paper from MetLab starting with the roughest grit (180), then with the 400 grit,600 grit, 800 grit and finally with 1200 grit paper. Polishing was done with alumina suspension, starting with the alumina particle size of Iμ then finishing it with 0. 05μ to obtain a mirror finish. The grinding and polishing are done on the StarGrind 200-2V grinding and polishing station shown in Figure 3-10b. Approximately 10 minutes of grinding was spent on each grade for each sample. Polishing was done with Al_2O_3 suspension (0.1 microns) to a mirror finish for 15 minutes. The polished samples are then taken through chemical etching with marble's reagent. The etchant used was a combination of $CuSO_4$, HCl and H_2O. Each sample was immersed fully for 25 seconds for the etchant to react completely with the sample. The samples were removed

from the etchant and rinsed thoroughly under running water and then neutralized with ethanol. The etched samples were studied under the optical microscope to document the structure and morphology of the observed microstructural features.

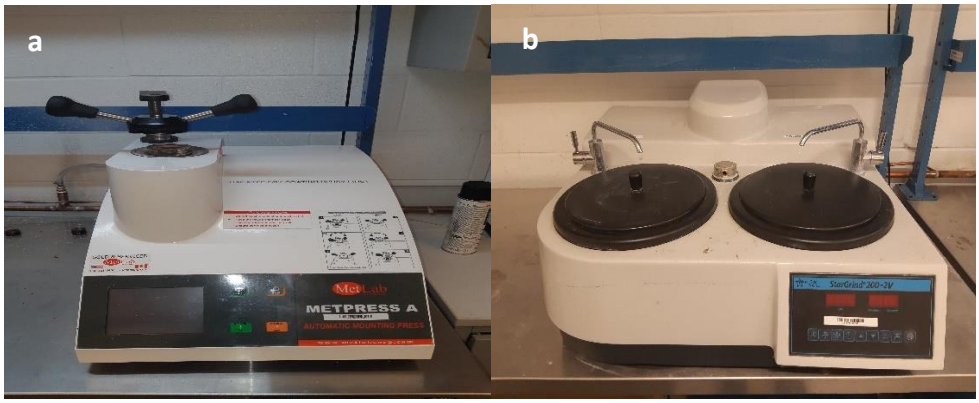

Figure 3-10: a) Hot- Mounting press b) Grinding and polishing station

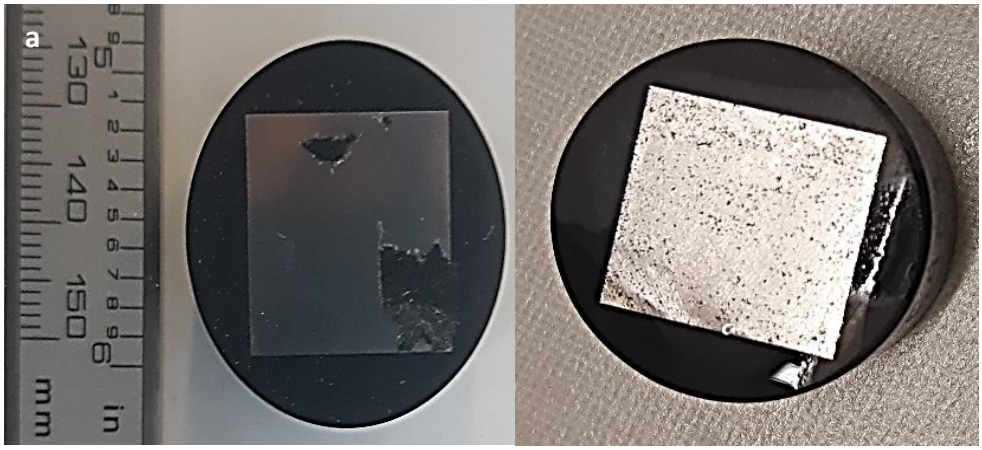

Figure 3-11: a) Mounted sample b) Sample after grinding

The samples were also studied with a scanning electron microscope (TESCAN SEM) to study the structure and morphology of the samples. 9kV of energy, with a beam intensity of 9.0 and at 25 mm working distance was adopted as settings for microstructural study. The SEM chamber was kept under vacuum in the presence of nitrogen gas. The samples were wrapped in carbon tape to reduce the rate of charging on the sample surface. The chemical composition and elemental mapping were carried out on the sample using the Electron Dispersive Spectroscopy (EDS) equipment attached to the SEM.

3.4 Determining the Surface Porosities and Density

Porosity in these samples was qualitatively analyzed using a 2d analysis approach. The porosity level in each sample was measured with the aid of ImageJ software by using 15 different pictures of the same magnification. Each image measures approximately 5.292 x 4.246 mm and a total of 15 images represents a theoretical coverage area of 75%. The size of one micrograph is shown in Figure 3-12a. The approximate areas that the micrographs where taken are also shown in Figure 3-12b where each area represents an average area of 3 micrographs. Average porosity is obtained from the 15 images as a representation of the whole sample. The surface porosities were determined using the image analysis software, Image J. Micrographs under various magnifications from the optical microscope of the unetched samples were used for the porosity analysis. The termed surface being used here is to denote the 2D measurement technique even though the surface here in internal to the sample. For each sample, 15 separate images under the same magnification were used for image processing making sure to stay away from jaggered edges of the samples. Each of the 15 images is taken through thresholding, where they are binarized, based on the threshold value that clearly distinguishes the grayscale values of the pores from the sample itself. The average

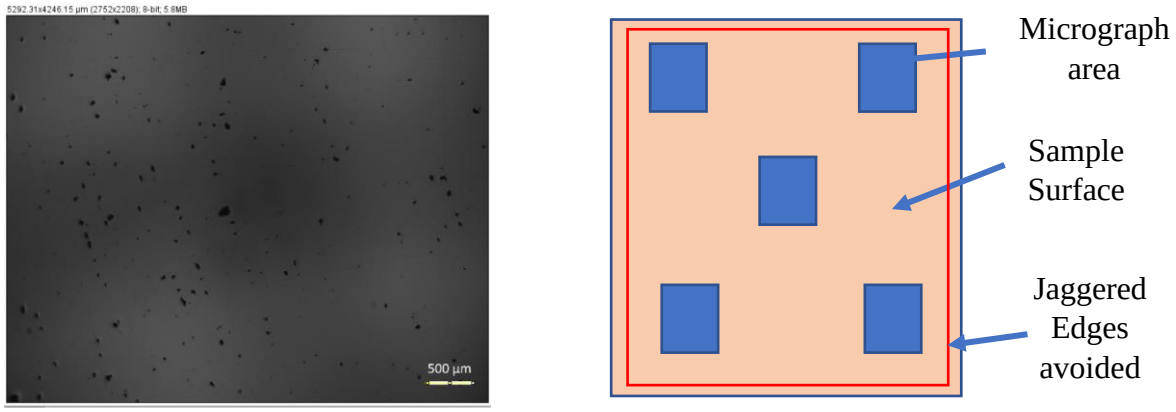

Figure 3-12: a) Micrograph size b) Approximate areas where images were taken

porosity is determined from the percentage area fraction from every single micrograph.

Part densities of the printed parts were determined by using the Archimedes principle according to the "ASTM B962-17 Standard Test Methods for Density of Compacted or Sintered Powder Metallurgy (PM) Products". The samples were cleaned, first with a diluted cleaning soap to remove dirt trapped on the sample surface. Secondly, the samples are rinsed completely with deionized water followed by cleaning with ethanol to get rid of any remaining solvent on the

samples. All the cleaning processes were done within a Branson Ultrasonic Bath with pressure 68 Pa. The ultrasonic bath employed in this study is shown in Figure 3-13.

The samples were weighed in both air and distilled water. The mass of the samples in the air was recorded as 'A' at room temperature with a Mettler Toledo balance shown in Figure 3-14. For the mass in water, the pores on the surface of the sample are coated with wax to prevent water from entering the sample. The wax coating was used to seal the connecting surface pore that will affect the buoyancy of the printed samples. These samples are made to cure under room temperature for 8 hours. The coated samples are weighed in air and noted as 'B'. Then, the coated samples were submerged and weighed to find the mass underwater.

The densities are determined using this formula based on the ASTM standard; as shown in equation (3.1)

Part density,

$$\rho_p = \frac{A\rho w}{B-F} \tag{3.1}$$

Where A= mass of the part in the air(g)

B=mass of the wax-coated part(g)

F=the mass of the wax-coated part in water with the mass of the support tared(g)

ρ_w =the density of water

Figure 3-13: Branson Ultrasonicator

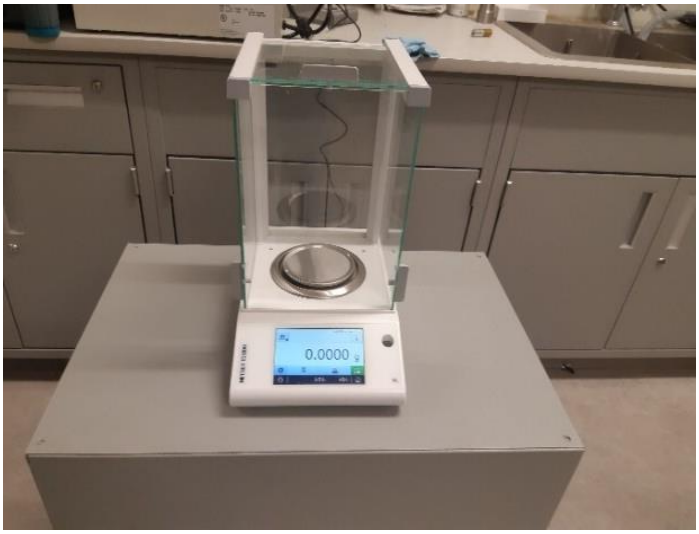

Figure 3-14: Mettler Toledo Balance

3.1 Hardness Testing

Hardness measurements were obtained using the Vickers Micro-Hardness Tester. This tester uses a pyramidal diamond tip indenter to impinge a known force to a point of interest on the sample surface. The hardness of the printed samples was tested with a force of 300gf which is equivalent to 2.94N. Ten different indentations were done per sample with dwell time for each indentation as 15 seconds. During the hardness testing, all indents that fell into pores were ignored.

Figure 3-15: Vickers Hardness Tester

The hardness values (HV) are obtained by measuring the diagonals of each quadrangular pyramid-shaped indent and found the corresponding hardness to the measured diagonals. The average of the indents was taken as the hardness of the sample.

3.2 Roughness Measurement

According to the ASTM G133-05, in order to effectively compare the wear rate of samples, it is required that the average surface roughness of each sample should not be within 0.02-0.05 µm. The surface roughness measurements of the printed 316L samples are measured using the Optical Profilometer from Bruker (Bruker Contour GT Optical profilometer). This surface roughness measurement system employs a non-contact method for measuring surface asperities and using high and low pass filters, the average 3-dimensional surface roughness values are obtained according to ISO 25178 standard.

Using an averaging technique to measure five separate regions, each measuring 1 x 1 mm area, and then taking the average measured roughness values to be representative of the roughness of the entire surface. To obtain the 1 mm^2 area, a window 0.3 x 0.3 mm was stitched over that area, with a 20% overlap which resulted in approximately 294 separate measurements.

Figure 3-16: Optical Profilometer [102]

3.3 Wear Testing

The wear tests are done according to ASTM G133-10 and the sample preparation was in accordance with the same standard. The counter body employed for the wear tests is a hardened steel E-5210. A 10 mm diameter ball is used with a hardness of 58 HRC and surface roughness measuring 0.04 μm. The ball and sample surfaces are thoroughly clean in a bath for 10 min prior to the test. The ball is firmly secured in the holder and the sample is also tightly fixed to the stage to avoid any motion as possible. The samples have an area of 20 x 20 mm to work with, but before the sample is secured in place, it is weighed on the balance to read the mass before wear. The ball is brought as close to the sample surface without touching it to make sure that running the test will not be done outside the sample surface in case there was any misalignment of the sample and the ball. A normal load of 25 N is used for the sliding test while maintaining a constant rate of 5 Hz. The stroke length is 10 mm with time 1000s which resulted in a total sliding distance of 100 m. This is equivalent to 5000cycles of the main drive on the tribometer. The equation used for this calculation is shown by Equations 3.2 and 3.3

$$\text{Sliding distance} = 0.002 \times t \times f \times L \tag{3.2}$$

$$\text{Cycles} = t \times f \tag{3.3}$$

The test was scripted in two steps;

Step1 that brings the ball into contact with the surface with a pre-load of 5 N for a total of 5s. This is to ensure the safe operating conditions of the sensors used in the equipment.

Step 2 involves the experiment itself. Here the load begins to ramp up from 5N to the testing load of 25N at a rate of 2N per sec. When the full 25N is attained, the slider that moves the sample begins to oscillate in a ‘to’ and ‘fro’ manner to begin wearing the sample.

After the first war track is completed at the end of the full cycle, the sample is carefully removed, and the debris cleaned off the track with a brush to make sure that all loose debris is gotten rid of. The sample is then weighed for the second time to calculate the mass loss after the experiment. The sample is placed back in the equipment for a second experiment using the same testing parameters. This is repeated three times and the average of the mass loss is determined to form the three separate tests. For each test, a new ball surface is used by rotating

the ball in the holder or using a new ball when there is no room for more wear scars. The mass loss for each step for each sample is recorded and represented (See Appendix B for detailed results form the wear test experiment). The Tribometer used is shown in Figure3-17 and a schematic of the test is presented in Figure 3-18. The tribometer records the COF of each of the test against time. The graphs for each test per sample are combined and shown in Appendix A1-8.

Figure 3-17: Universal Mechanical Tester Tribolab[103]

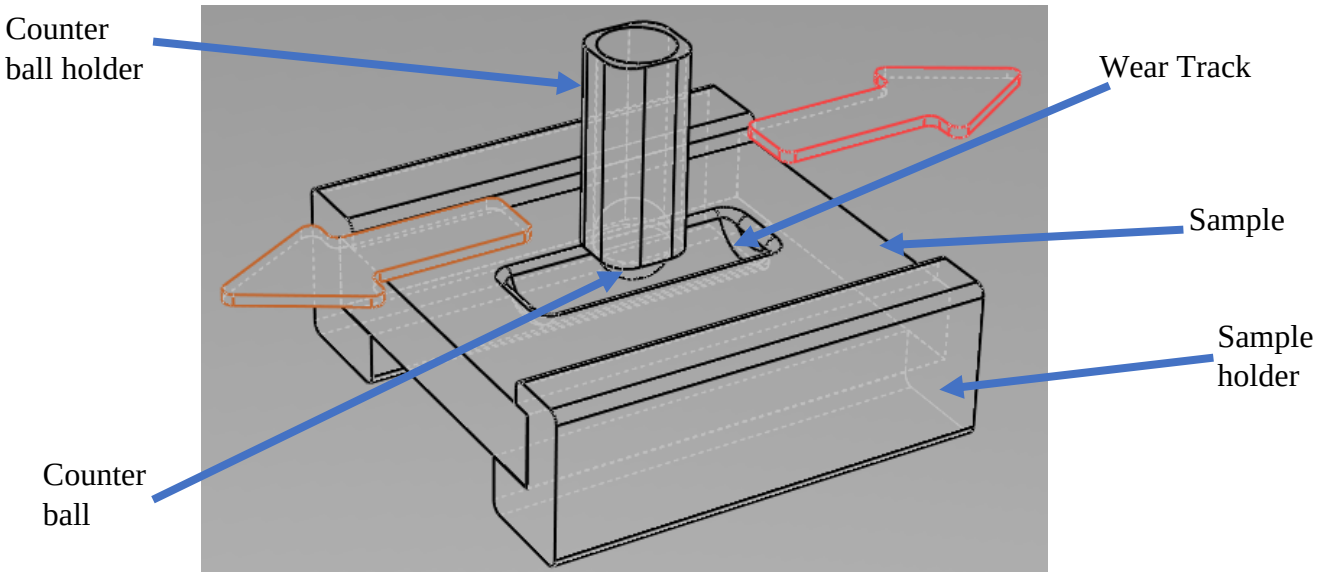

Figure 3-18: Schematic of the wear test

4 RESULTS

4.1 Effect of Printing Parameters on Surface Porosities

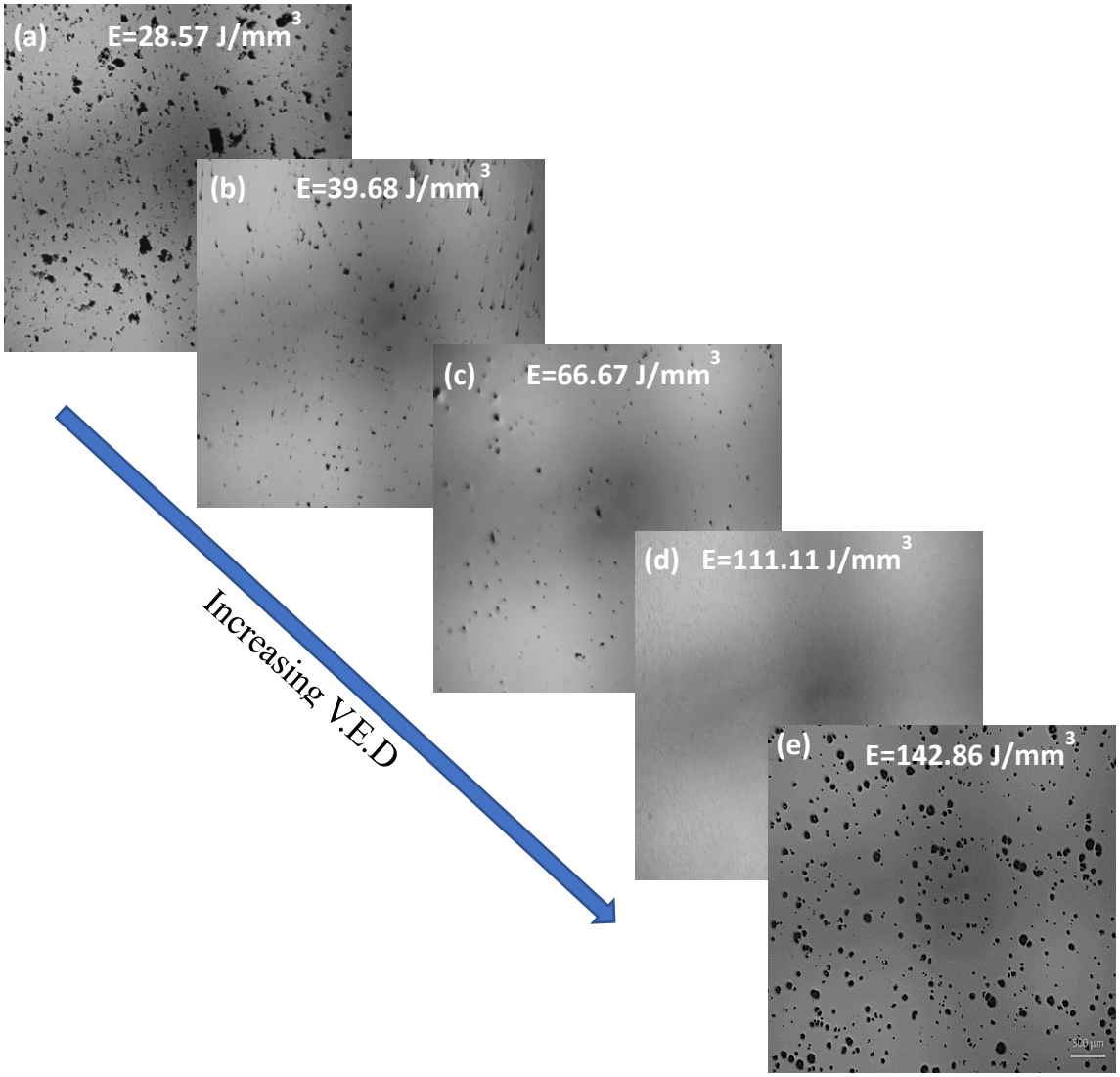

Figure 4-1: Effect of increasing V.E.D on surface porosity with (a) high level of porosity at 28.57 J/mm3 (b) moderate level of porosity at 39.68 J/mm3 (c) low level of porosity at 66.67 J/mm3 (d) very low level of porosity at 111.11 J/mm3 (e) re-emergence of pores

There was a good relationship between the printing parameters and surface porosities. Figure 36 shows the micrographs of the printed samples showing the surface porosities. The pore type, size, and distribution changed as the printing parameters were changed as shown in Figure 4-1 The printed sample which had a volumetric energy density of 20.41J/mm^3 had different pores dispersed across the sample as was observed for all the other samples with pores. The sizes of

surface pores in this sample were relatively bigger and seen as a black smudge as shown in Figure 3-11b.

An increase in the energy density from 20.41J/mm^3 to 28.57J/mm^3 decreased the volume fraction and sizes of the pores as shown in Figure 4-1b. In Figure 4-1d, the sample with a volumetric energy density of 111.11J/ mm^3 had the relatively lowest volume fraction of pores together with the lowest pore sizes. Beyond the volumetric energy density of 111.11J/ mm^3, there was an abrupt and significant increase in the size and volume fraction of the surface pores as shown by Figure 4-1e. Thus, the surface porosities of the samples reduced as the volumetric energy density increased from 28.57J/ mm^3 to 111.11J/ mm^3 and increased as the volumetric energy density increased above 111.11J/ mm^3 as shown in Figure 4-1. Table 4-1 shows the measured average porosity and the standard deviations and errors for the micrographs processed with the ImageJ software.

Table 4-1: Porosity level from Image processing (ImageJ)

Sample	Energy Density (J/mm3)	Average Porosity (%)	Std Dev	Std error
G4D1	20.40816	49.4310	3.391906	1.072615
G4C1	28.57	8.8576	2.439743	0.771515
G2D1	28.57143	6.2480	2.11106	0.667576
G4D3	34.01361	5.6310	1.515855	0.479355
G3D3	39.68254	1.4030	0.389686	0.12323
G3C2	44.44444	0.8090	0.334898	0.105904
G3C3	55.55556	2.4000	0.886716	0.267355
G4B2	63.49206	0.1450	0.024412	0.00772
G1C2	66.66667	0.4134	0.110894	0.035068
G2B1	66.66667	0.3990	0.06662	0.021067
G4B3	79.36508	0.0170	0.007315	0.002313
G1C3	83.33333	0.1560	0.06606	0.023356
G2B2	88.88889	0.0076	0.012619	0.00399
G1B2	111.1111	0.0972	0.054228	0.024252
G4A1	142.8571	6.3186	1.465029	0.441723

Figure 4-2 shows the measured volume fractions of the surface porosities as a function of volumetric energy density. The highest volume fraction of pores was obtained at the least energy density, 20.41 J/mm^3, which was a recorded 49%. The lowest volume fraction of pores was acquired at volumetric energy densities between 45 J/mm3 to 111 J/mm3. Increasing the volumetric energy density from 20.41 to 39.68 J/mm^3 caused the volume fraction of pores to reduce by a massive 48%. However, increasing the energy density from 39.68 J/mm3 to 88.89 J/mm^3 did not result in any significant reduction in the volume fraction of the pores since there was approximately only 1.39% reduction in surface porosities. In addition, any more increase in volumetric energy density beyond 88.89 J/mm3 to 111.11J/mm3 does not present any significant reduction in surface porosities. Thus, volumetric energy densities between 39.68 J/mm^3 and 111.11J/mm^3 offer approximately the same volume fraction of surface porosities. Beyond this VED, the pores on the surface of the samples begin to increase again. The sample with the highest volumetric energy density of 142 J/mm^3 had 14.13% volume fraction of surface porosities which is almost the same as the sample with volumetric energy densities of 28.57 J/mm^3 which had a 17.14% volume fraction.

There were 2 main types of surface pores observed in the printed samples as shown in Figures 38 and 39. These were lack-of-fusion pores and gas pores. Typically, the surface pores in the samples with volumetric energy densities between 20.41-55.56 J/mm3 were lack of fusion pores. These pores are polyangular in shape as shown in Figure 38a-f. There are instances were these pores join to form larger pores and they are also populated with powder unmelts. Also, the surface pores in the samples printed from 66.67-111.11 J/mm^3 volumetric energy densities showed circular surface pores as shown in Figure 4-3a-e. The sample with the highest volumetric energy density of 142.86 J/mm^3 showed keyholes as seen in Figure 4-3f.

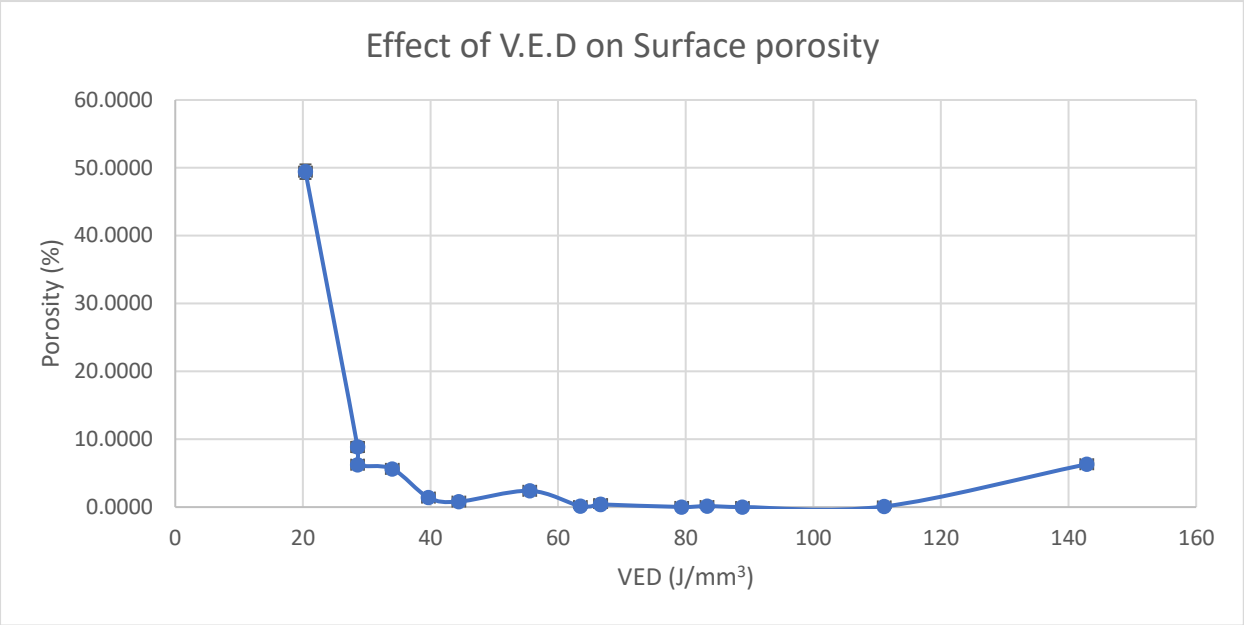

Figure 4-2: Porosity levels as a function of V.E.D

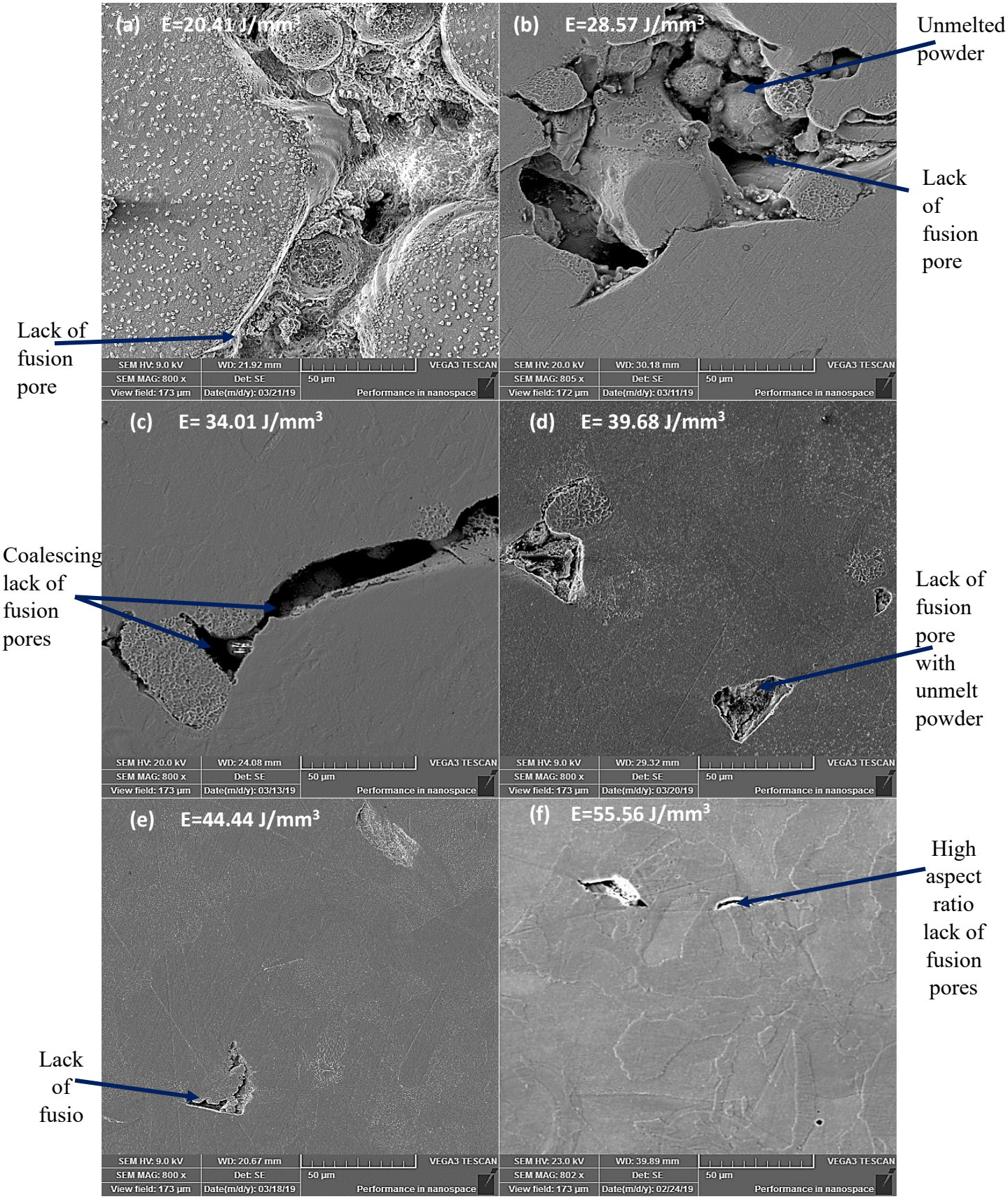

Figure 4-3: Micrographs showing low v.e.d samples impregnated with lack of fusion pores at increasing v.e.d of (a) 20.41, (b)28.57, (c)34.01, (d)39.68, (e)44.44 and (f)55.56 J/mm^3

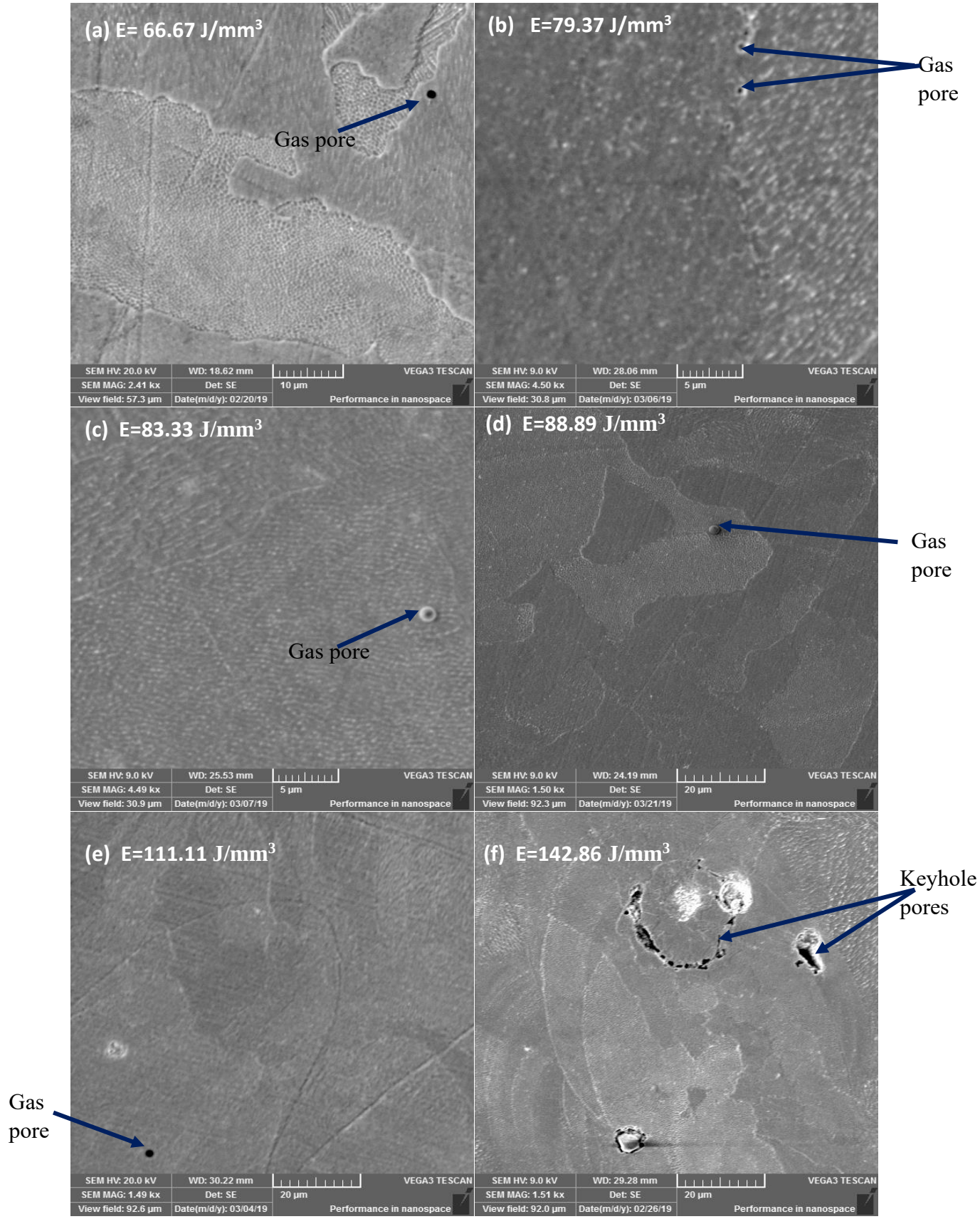

Figure 4-4: Micrographs showing high v.e.d samples impregnated with circular gas pores at increasing v.e.d of (a) 66.67, (b)79.37, (c) 83.33, (d) 88.89, (e)111.11 and (f) showing keyholes at 142.86 J/mm^3

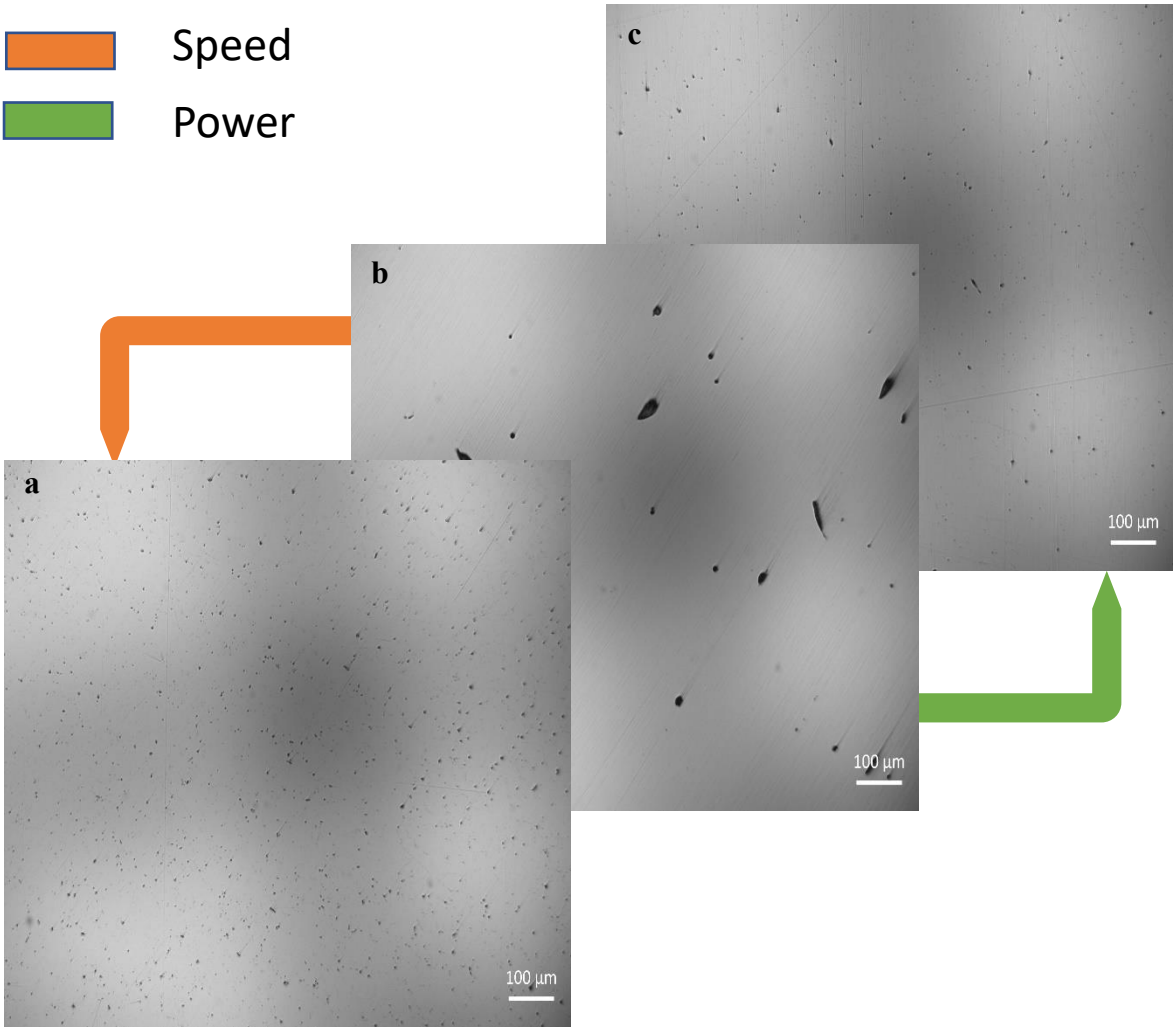

Figure 4-5: Effect of Laser Power and Scan Speed on Porosity size and distribution using a constant hatch spacing of 80 µm a) G1B2 b) G1C2 c) G1C3

4.1.1 Effect of Parameters on Pore Size and Distribution

The individual parameter's effects on the size and distribution of the pores are also accessed. The analysis is done in groups depending on the type of hatch spacing used to fabricate the part. The first group studied are the samples printed with a constant hatch spacing of 80 µm, and the effect of power and scan speeds are accessed separately. The orange arrow denotes a change in speed while the green arrow shows a change in laser power. Sample G1C2 in Figure 4-5b with a scan speed of 1250 mm/s and power of 200 W is used as the reference sample here. This reference sample surface has a high aspect pore randomly distributed on the surface. When there is a reduction in speed to 750 mm/s, the pores reduce considerably in size but maintains a uniform distribution across the sample surface as shown in Figure 4-5a. The pore count also increases with relatively the same pore sizes. However, an increase in power from

200-250 W though also causes a reduction in pore sizes, the sizes are not uniform. In this case, there are bigger pores amidst smaller pores that are randomly distributed. The sample with the lowest amount of porosity in this group is sample G1B2.

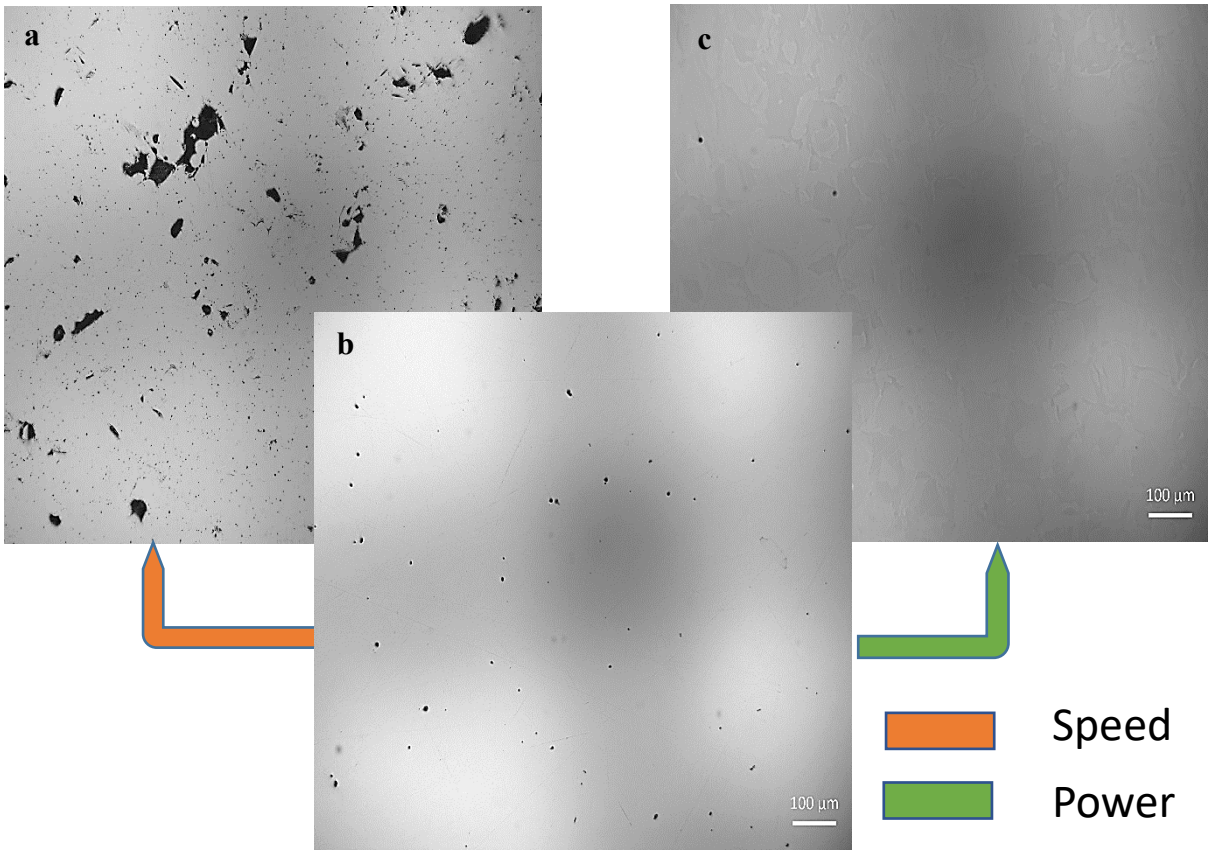

Figure 4-6: Effect of Laser Power and Scan Speed on Porosity size and distribution using a constant hatch spacing of 100 µm a) G2D1 b) G2B1 c) G2B2

The second group of samples looked at are fabricated with hatch spacing of 100 µm, which shows zero overlap and zero offset of the beams of adjacent scan lines from the schematic shown in Figure 4-6b. Using sample G2B1 shown in Figure 4-6b as a reference with a power of 150W and 750 mm/s speed. An increase in power by 50 W leads only to a reduction in pore count, but the size of pores present remains the same as the sizes in the reference sample which is evident in Figure 4-6c. On the other hand, increasing the speed to 1750 mm/s shows a huge increase in pore sizes with non-uniform pore sizes and distribution. G2D2 shown in Figure 4-6c has the least porosity level in this group.

The third group of samples looked at are fabricated with hatch spacing of 120 µm, which shows 20 µm offset of the beams of adjacent scan lines from the schematic shown in Figure 24a. Taking sample G3C3, which has a power of 250W and 1250 mm/s speed, as the reference sample. This reference sample shows irregularly shaped pores with different sizes and mostly with high aspect ratios. A reduction in laser power to 200W shows the high aspect ratio pores becoming globular (increasing roundness). The pore count shows negligible change as observed in sample G3C2 shown in Figure 4-7c. Sample G3D3 to the left of the reference sample shows an increase in scan speeds revealing a reduction in pore sizes but also shows negligible pore count differences as seen in Figure 4-7a. Sample G3C2 recorded the least porosity in this group of samples.

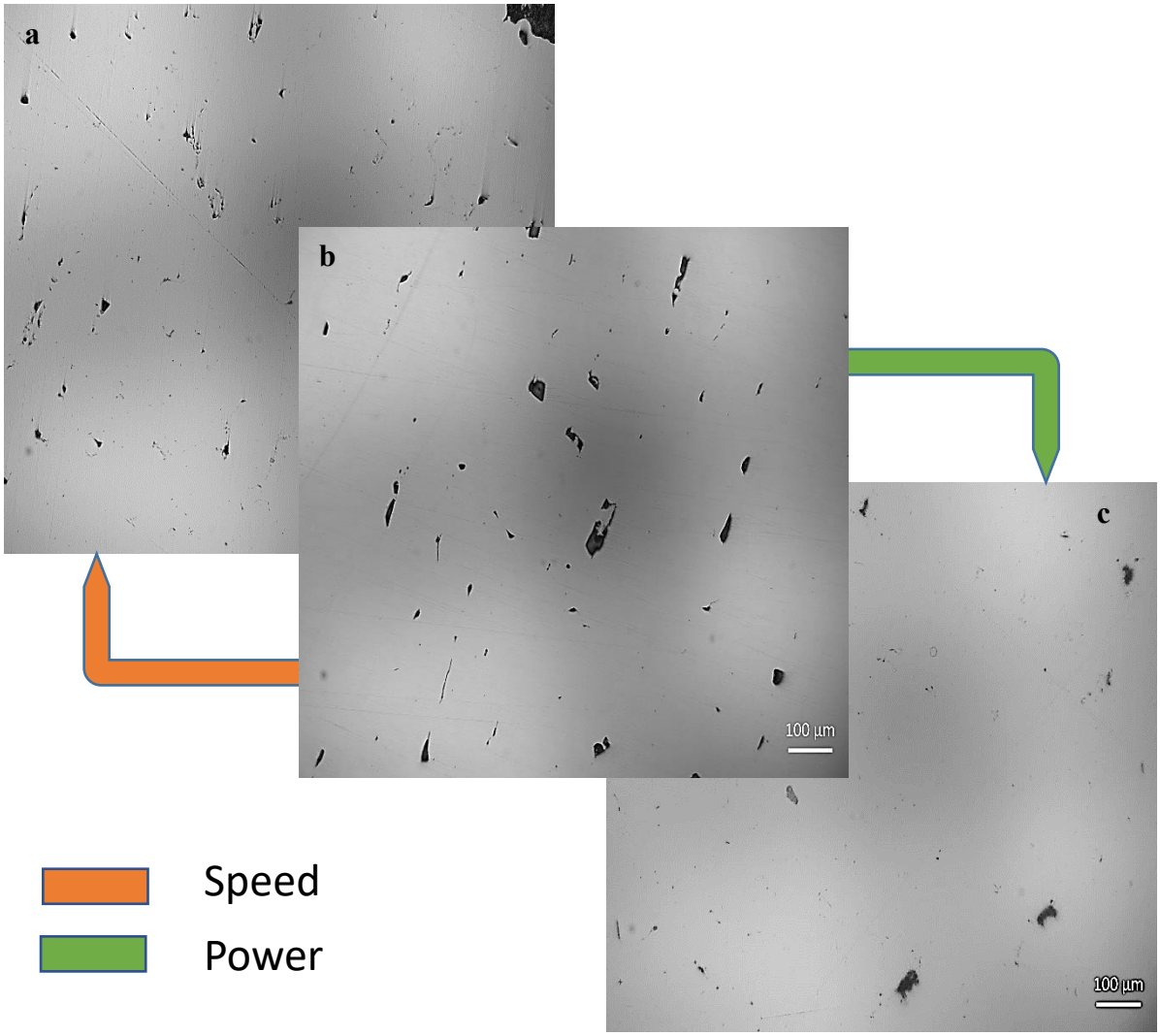

Figure 4-7: Effect of Laser Power and Scan Speed on Porosity size and distribution using a constant hatch spacing of 120 µm a) G3D3 b) G3C3 c) G3C2

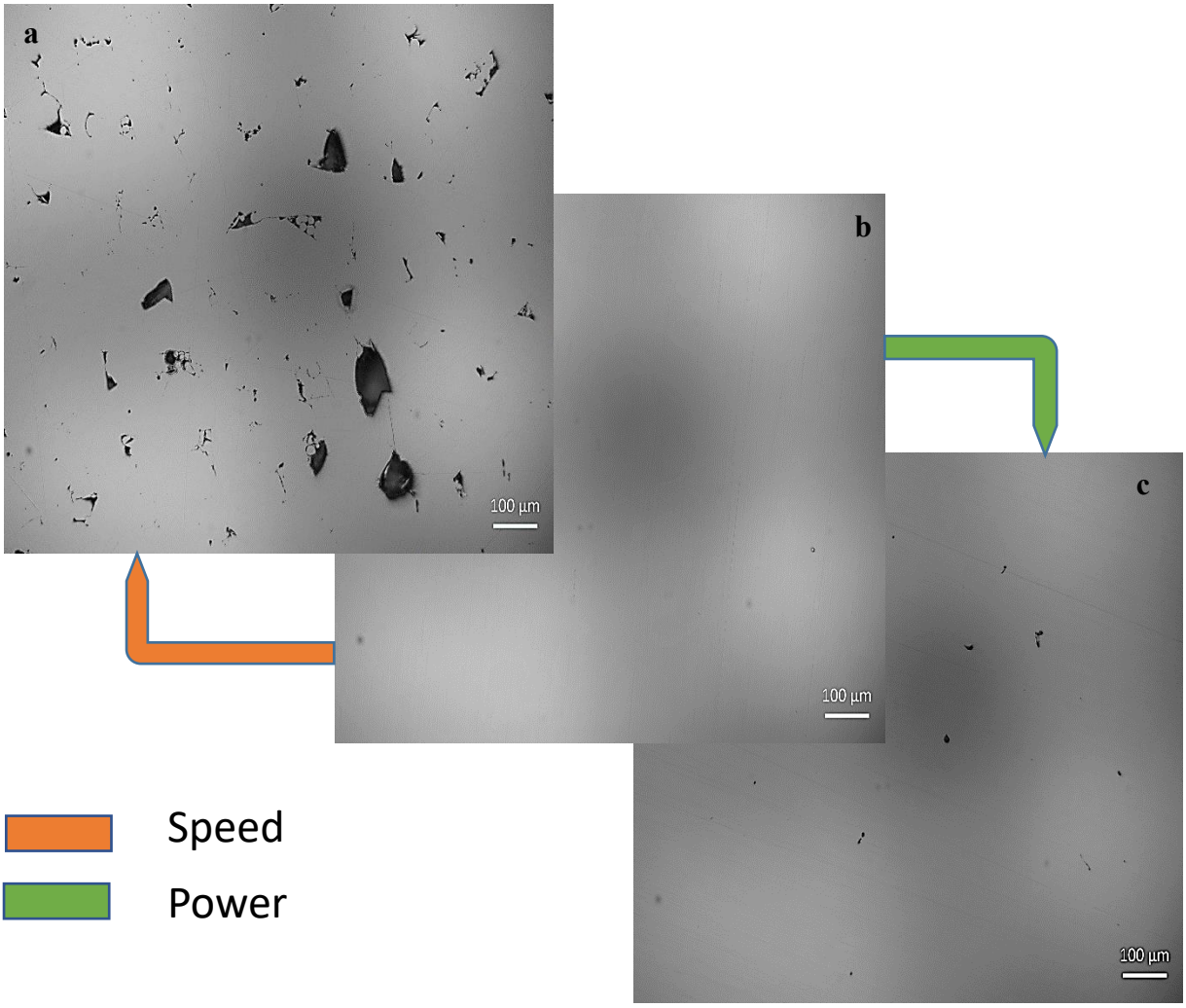

Figure 4-8: Effect of Laser Power and Scan Speed on Porosity size and distribution using a constant hatch spacing of 140 mm a) G4D3 b) G4B3 c) G4B2

The fourth group of samples is fabricated made with hatch spacing of 140 µm, which is an offset of 40 µm shown in the schematic presented in Figure 4-8b. Sample G4B3 with laser power of 250W and speed of 750 mm/s, shown in Figure 4-8b, is used as the reference sample. An increase in scan speed from 750 mm/s to 1750 mm/s resulted in irregular pore sizes and random distribution of the pores. The pore count increases the same as when the power is lowered to 200W in sample G4B2 as shown in Figure 4-8c. The pore size increase with the non-uniform distribution of pores. The effect of scan speed only is also accessed among three different samples as shown in Figure 4-8. Using another reference sample G4D1 which shows the higher level of porosity in all the 15 samples as seen in Figure 4-9c. When the scan speed is reduced from 1750 mm/s to 1250 mm/s, the pore sizes reduce significantly as well as an increase in pore count. The pores that were seen in the sample with the lower speed increase in roundness amidst high aspect ratio pores with a decrease in speed. Further reduction in scan

speeds yields the same result by a reduction in pore sizes and the pores become completely round. Sample G4B3 recorded the lowest porosity level in this group of samples.

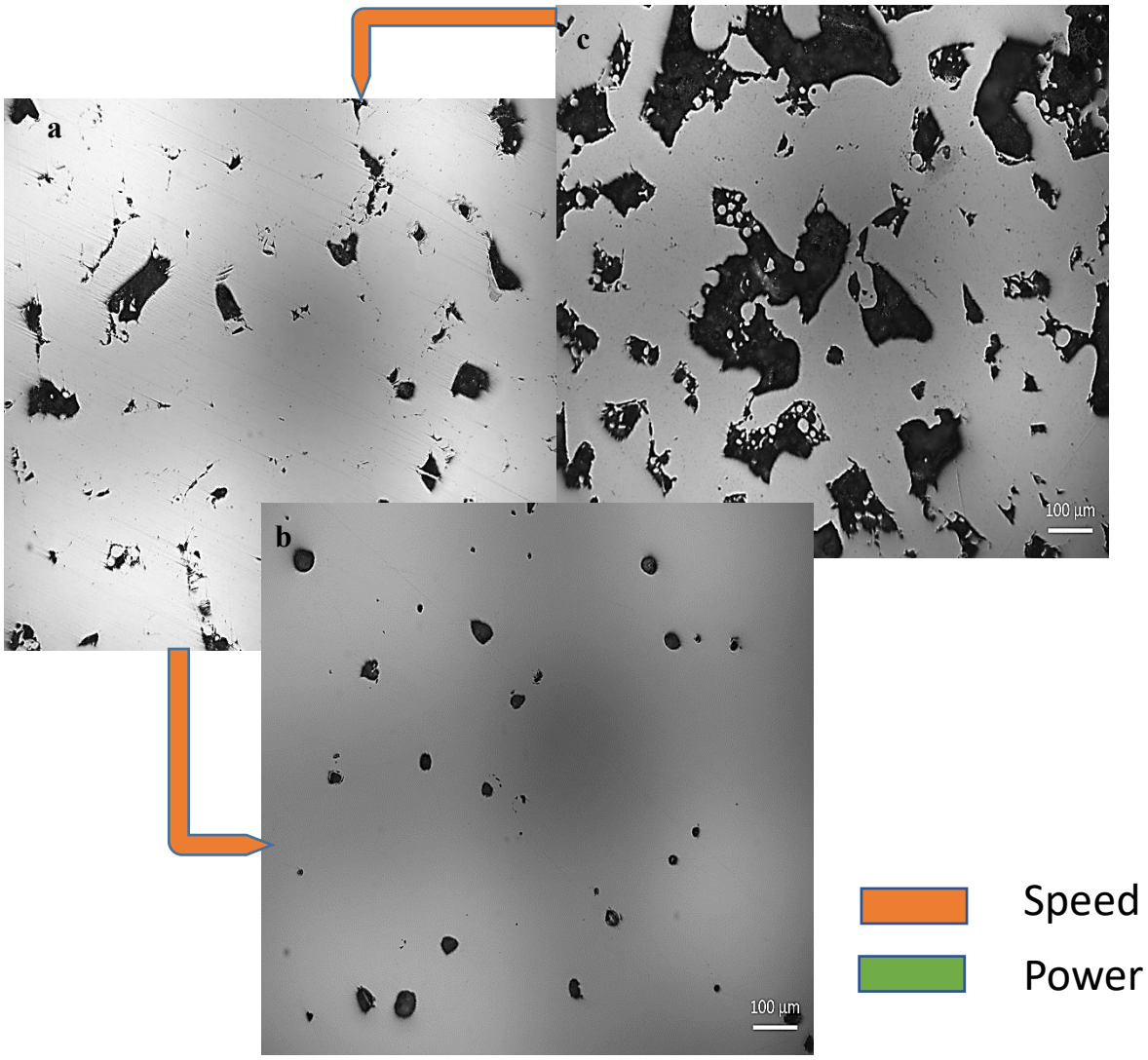

Figure 4-9: Effect of Scan Speed on Porosity size and distribution using a constant hatch spacing of 140 µm a) G4C1 b) G4A1 c) G4D1

4.1.2 Parameter Sensitivity on Porosity

The individual parameter sensitivity on the formation of pores on the sample surface is also analyzed. Firstly, the sensitive of scan speeds against porosity is accessed. As evident from Figure 4-10, using the lower laser power of 150 W and hatch spacing of 140 µm, an increase in speed by 400% led to a 3.02% increase in porosity level and a 40% increase resulted in a corresponding increase in porosity by 32.29%. The laser power of 200W and hatch spacing of

80 µm, an increase in speed from 750 mm to 1250 (66.67%) resulted in a 0.32% increase in porosity level from 0.09% to 0.41%.

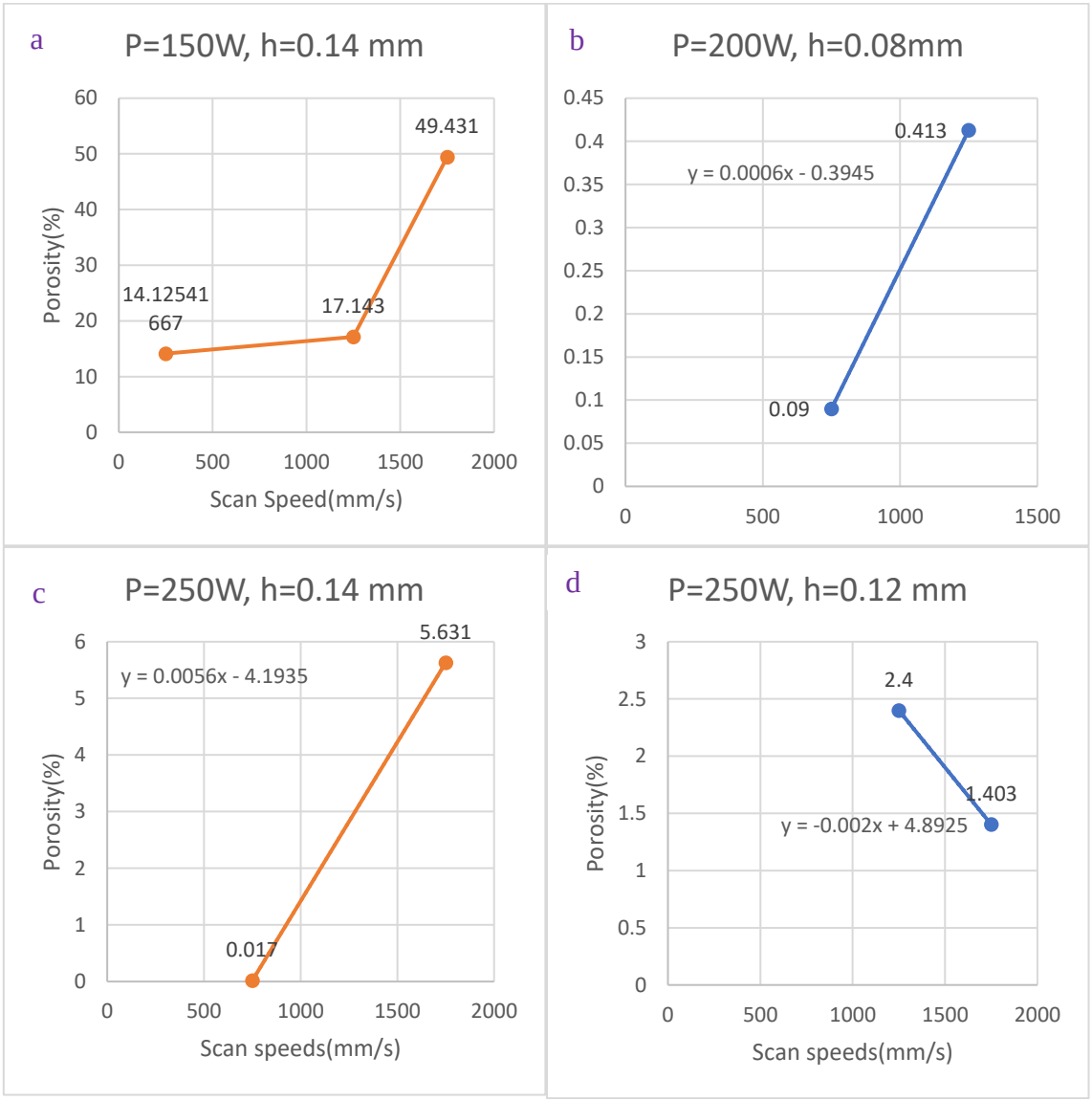

Figure 4-10: Sensitivity of scan speeds to part porosity

Similarly, an increase in speed from 750 mm/s to 1750 mm/s (133.3%) leads to a 5.6% increase in porosity when using 250 W at a hatch spacing of 140 µm. However, with a 250 W, the speed at 1250 mm/s and a hatch spacing of 120 µm, a high porosity of 2.4% is recorded. An increase in scan speed by 40% in this regard resulted in a reduction of the porosity level to 1.4%, a 1% reduction in porosity level.

In the second part of the parameter sensitivity analysis, the influence of the laser power on porosity was studied as shown in Figure 4-11. An increase in laser power by 66.7% from 150-

250 W, while maintaining a speed of 1750 and hatch spacing of 140 µm, results in a porosity reduction of 43.8%. A reduction in porosity (by 0.25%) is observed as well when the laser power gets increased by 25% from 200 -250W while maintaining an 80 µm hatch spacing and 1250 mm/s scan speed.

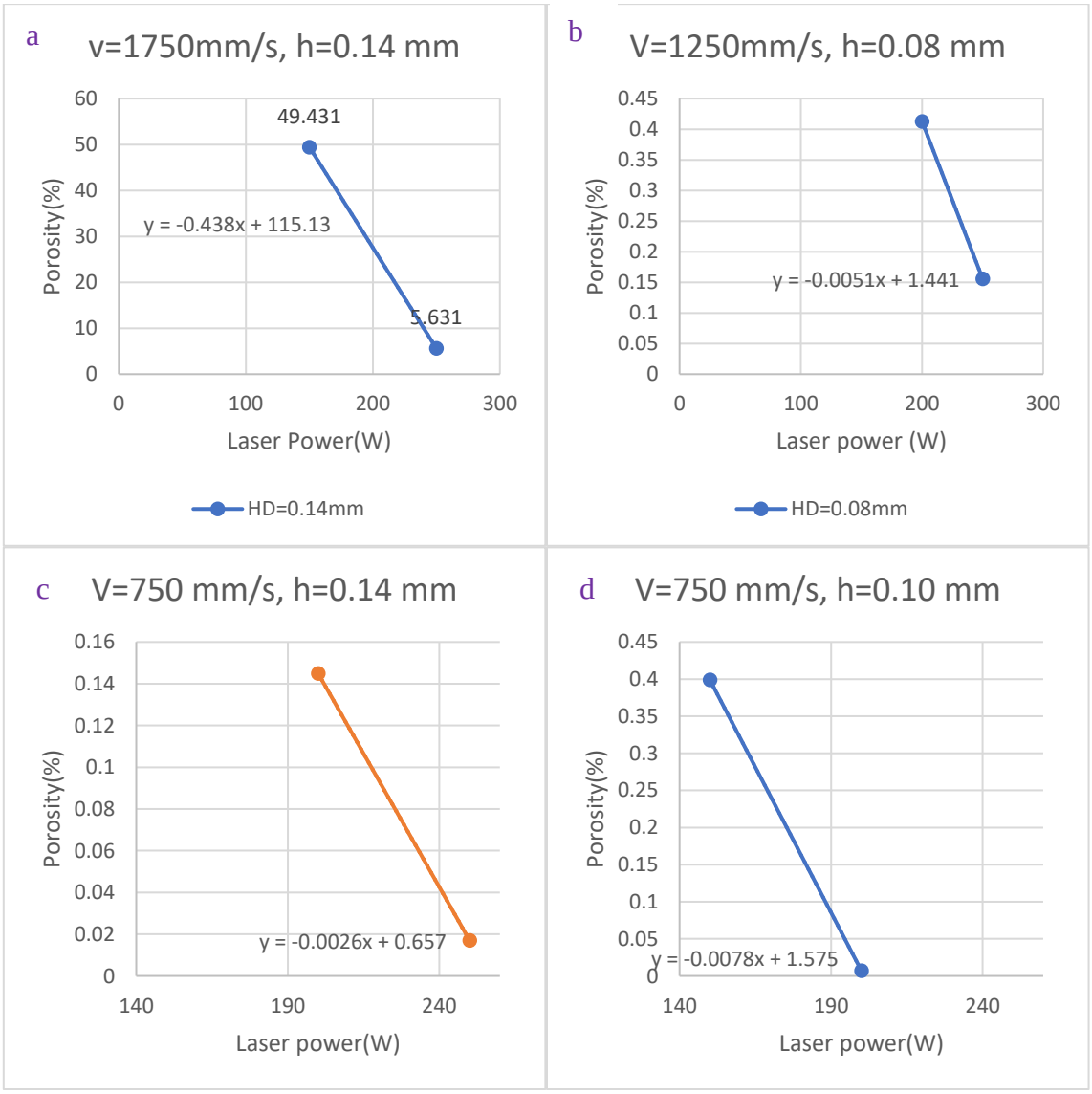

Figure 4-11: Sensitivity of Laser Power to part porosity

Similarly, an increase in power by 25% under a constant speed of 750 mm/s and 140 µm spacing results in a 0.14% decrease in porosity levels. A reduction of 0.39% in porosity is observed as the power increase by a 33.3% form 150 -250W at a constant speed of 750 mm/s and hatch spacing of 100 µm.

For the final part of the parameter sensitivity assessment, the hatch spacing influence on porosity is explored as illustrated in Figure 4-12. At a constant power of 150 W and a scanning

speed of 1750 mm/s, a 40% increase in hatch spacing from 100 µm to 140 µm results in an increase in porosity levels by 43.8%. An increase in porosity is observed as well when the spacing is increased from 80 µm to 140 µm (%) from 0.41-0.81%, a 0.40% change, all while maintaining 200W of power and 1250 mm/s laser speed. A similar trend is observed by increasing the hatch spacing from 120 µm to 140 µm (16.7%) under constant laser power of 250 W and speed of 1750 mm/s.

However, a decrease in porosity level is observed when the hatch spacing is reduced from 80 µm to 120 µm, a 50% increase in spacing while maintaining the power at 250 W and the scan speed at 1250 mm/s.

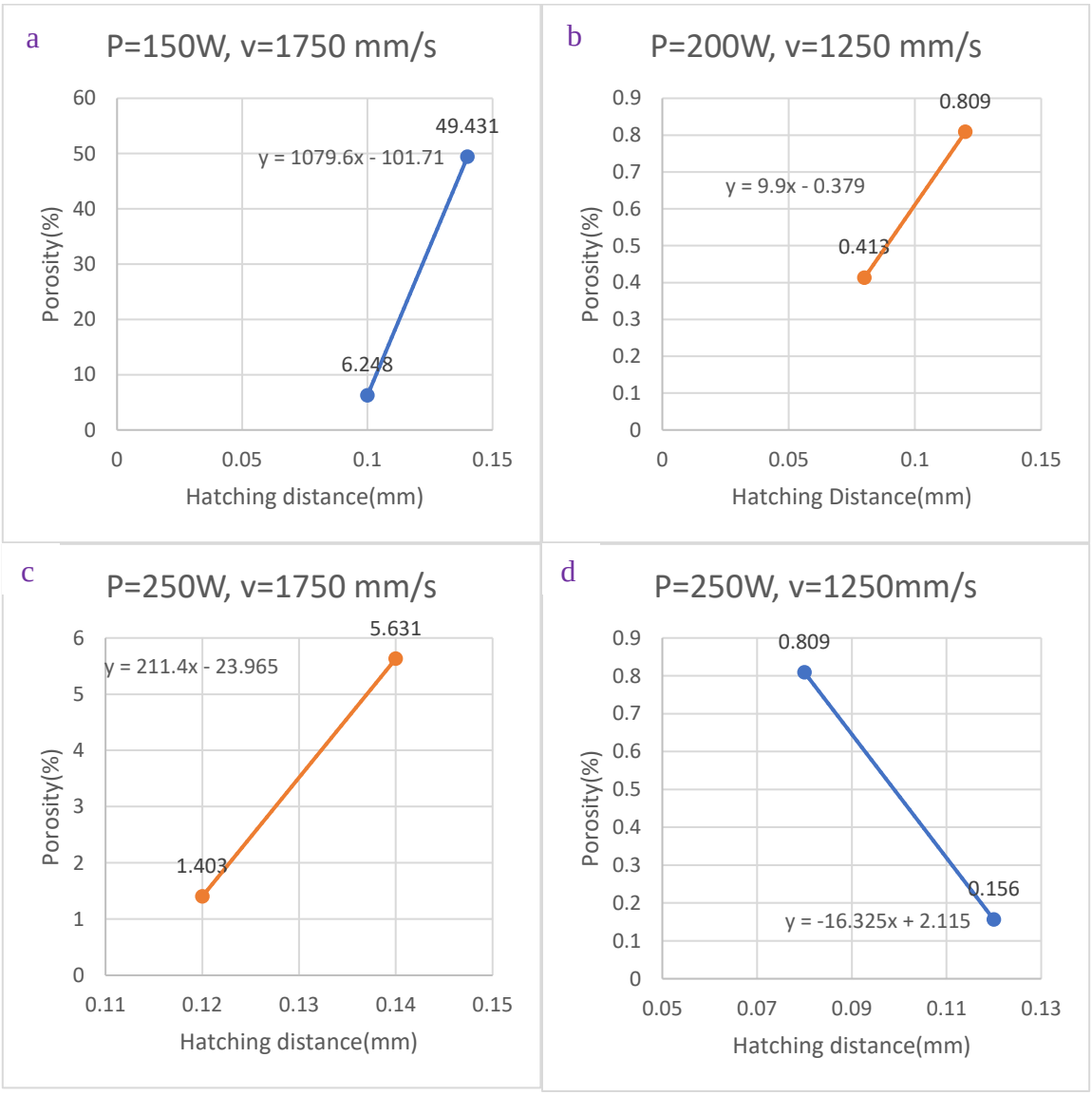

Figure 4-12: Sensitivity of hatch spacing to part porosity

4.2 Effect of Printing Parameters on Part Density

Generally, as the volumetric energy densities increase, the relative densities of the printed parts also increase as shown in Figure 4-13. These results were consistent with the volume fraction of the surface porosities. Part densification initially increased as the volumetric energy densities increased to a point where the density remains steady until the volumetric energy densities cross the 111.11 J/mm^3 threshold where the part density begins to drop. The sample with the lowest volumetric energy density also recorded the lowest relative density at 5.97 g/cm^3 which is 33.84% lower than the theoretical value (7.99 g/cm^3.) An increase from 20.41 to 39.68 J/mm^3 causes the density to rise by 22.3%, from 5.97 to 7.30 g/mm^3. Thus, volumetric energy densities between 39.68 J/mm3 and 111.11J/mm3 gave the highest amounts of densification as indicated by their relatively high densities which were closest to the theoretical densities.

However, an additional increase in the volumetric energy density (VED) from the 39.68 to 111 J/mm^3, a 180% VED increase resulted in only a 2.74% increase in density. Thus, regardless of the huge amounts of increase in VED, there is no significant increase in the relative density of the printed samples. These results were very consistent with the observed trend in the volume fractions of the surface porosities.

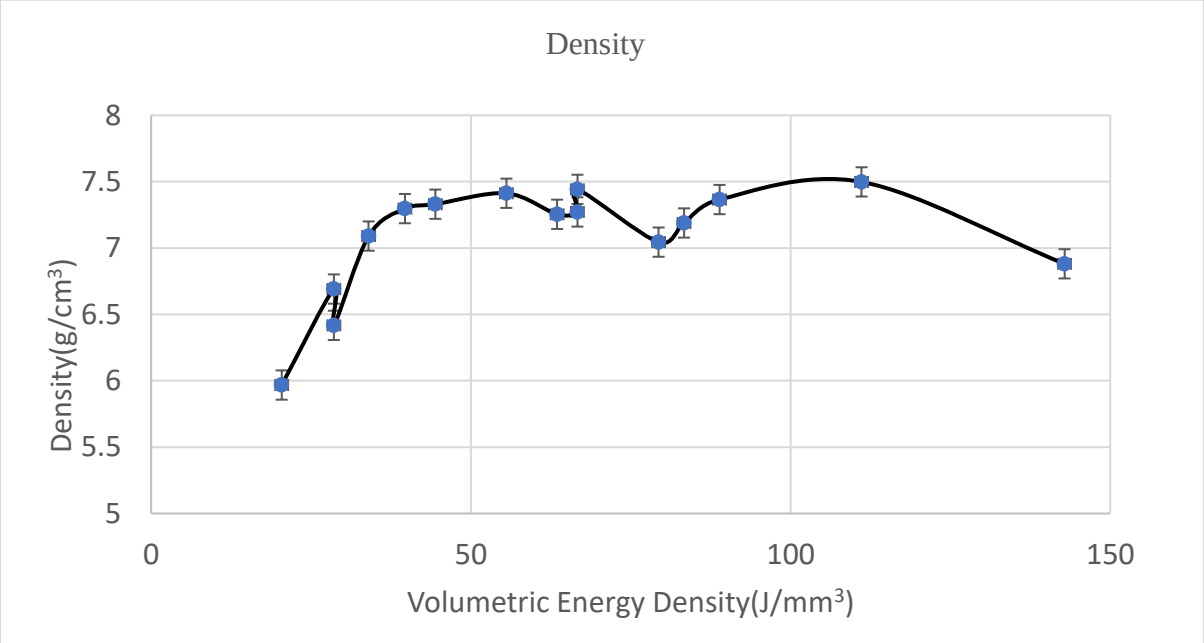

Figure 4-13: Part Density as a function of V.E.D

4.3 Effect of Printing Parameters on The Hardness and Evolved Microstructure of the Printed Samples

Table 4-2: Micro-hardness measurements of samples

Samples	Volumetric Energy Density(J/mm3)	Hardness (HV)
G4C1	28.57	208.70 ± 15.52
G2D1	28.57	209.82 ± 11.91
G4D1	20.41	230.10 ± 14.68
G2B1	66.67	233.80 ± 4.69
G4A1	142.86	238.64 ± 9.89
G1B2	111.11	234.10 ± 6.47
G3C2	44.44	235.10 ± 5.15
G2B2	88.89	236.10 ± 11.86
G4B2	63.49	240.10 ± 7.53
G1C2	66.67	241.00 ± 6.99
G3D3	39.68	224.80 ± 13.84
G4D3	34.01	227.00 ± 14.29
G3C3	55.56	231.00 ± 13.97
G1C3	83.33	233.42 ± 8.03
G4B3	79.37	236.50 ± 10.00

The hardness of the printed samples ranged from approximately 208.7 - 241 HV as seen in Figure 4-14. Two samples with 28.57 J/mm3 VED had hardness below 210 HV. Sample G4D1 and G2B1 with energy densities of 20.41 J/mm^3 and 66.67 J/mm^3 had hardness values below 230 HV (230.10 ± 14.68 and 233.80 ± 4.69 HV respectively). The majority of the samples fell within 220-230 HV hardness values as shown in Figure 4-14. A sample with an energy density of 66.67 J/mm3 had the highest hardness of 240 HV. Thus, volumetric energy densities between 44.44 J/mm3 to 111.11 J/mm3 gave the highest hardness values which are consistent with the trends observed for both the volume fraction of surface porosities and relative densities.

Generally, it was observed that the printing parameters had a significant effect on the evolution of the microstructure as well as observed discontinuities and defects. It was observed that the amount and size of unmelted/unfused powders reduce as the amount of energy delivered to the powders during printing increases as shown in Figure 4-15.

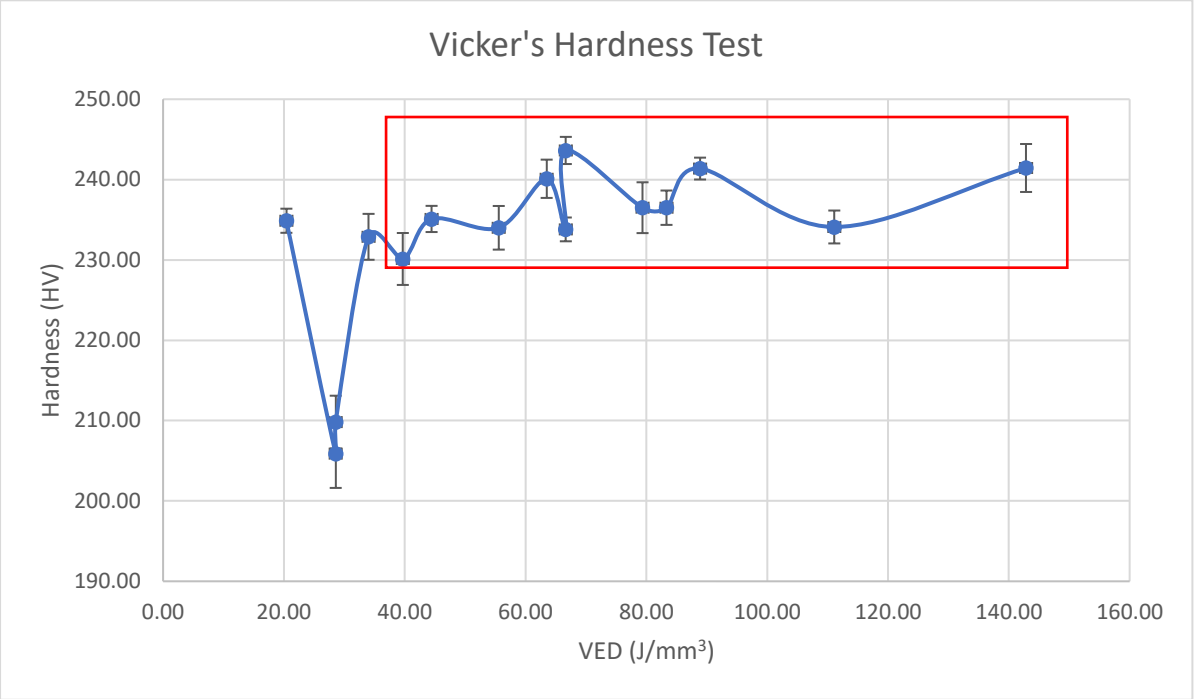

Figure 4-14: The hardness of samples as V.E.D Increases

The as-printed samples had many regions riddled with large unfused powders when printed using volumetric energy densities between 20.41 J/mm^3 to 44.44 J/mm^3. Increasing the VED by 42% from 44.44 to 63.49 J/mm^3 resulted in a drastic reduction in the size and amount of unmelted/unfused powders as shown in Figure 4-15b. There were no observed unmelted/unfused powders when the VED was increased beyond 66.67 J/mm^3.

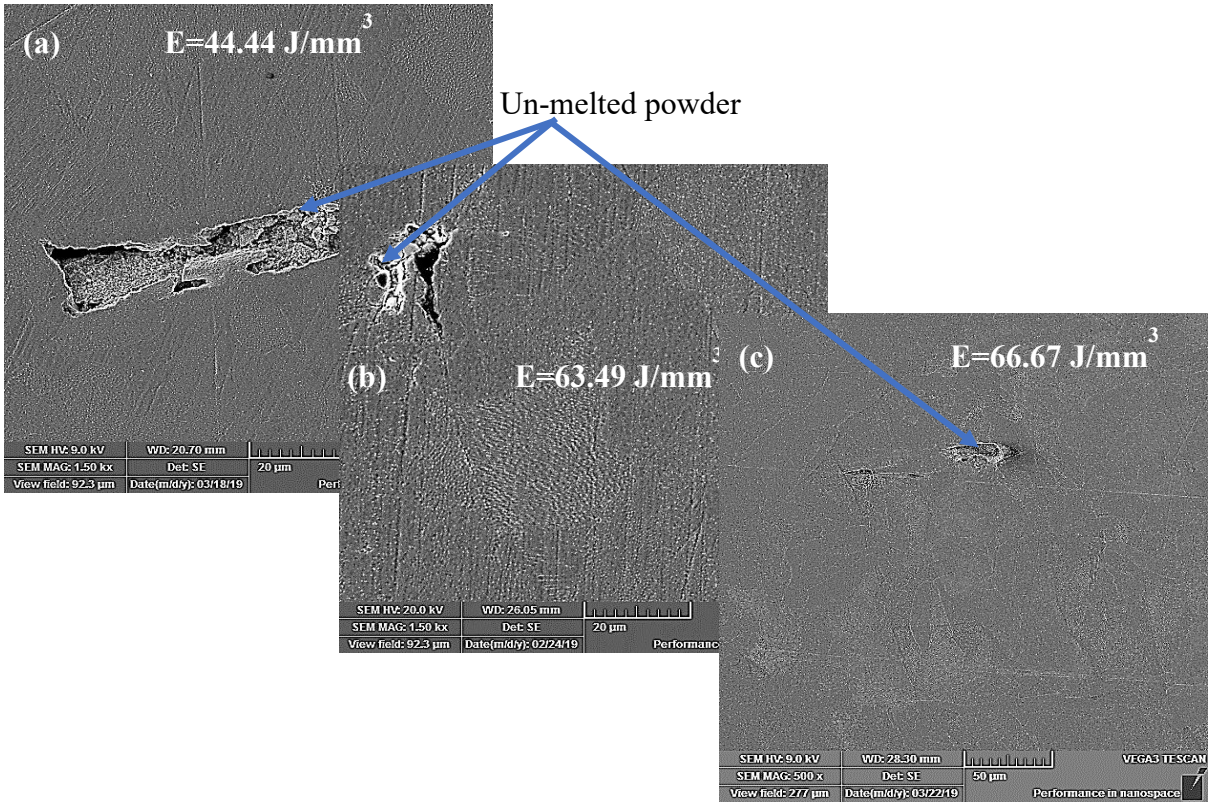

Figure 4-15: Effect of v.e.d on the amount of un-melted powders showing (a) high amount of unmelted powders at 44.44 J/mm^3 (b) moderate level of unmelted powders at 63.49 J/mm^3 and (c) powder depression at 66.67 J/mm^3

For all the 15 samples there were two distinct substructures or microstructural features observed at the microscale, cellular structures, and columnar/lath structures. It was clear that the individual printing parameters affected the size and morphology of these microstructural features including instances where there were distinctions in the orientation of these substructures. Comparing these substructures that evolved in the samples, increasing the laser power makes the substructures more distinct and well defined as shown in Figure 4-16. The boundaries of the cellular and columnar structures become thicker and well-defined as the laser power increased from 200 W to 250 W which translates to a 25% increase in power level.

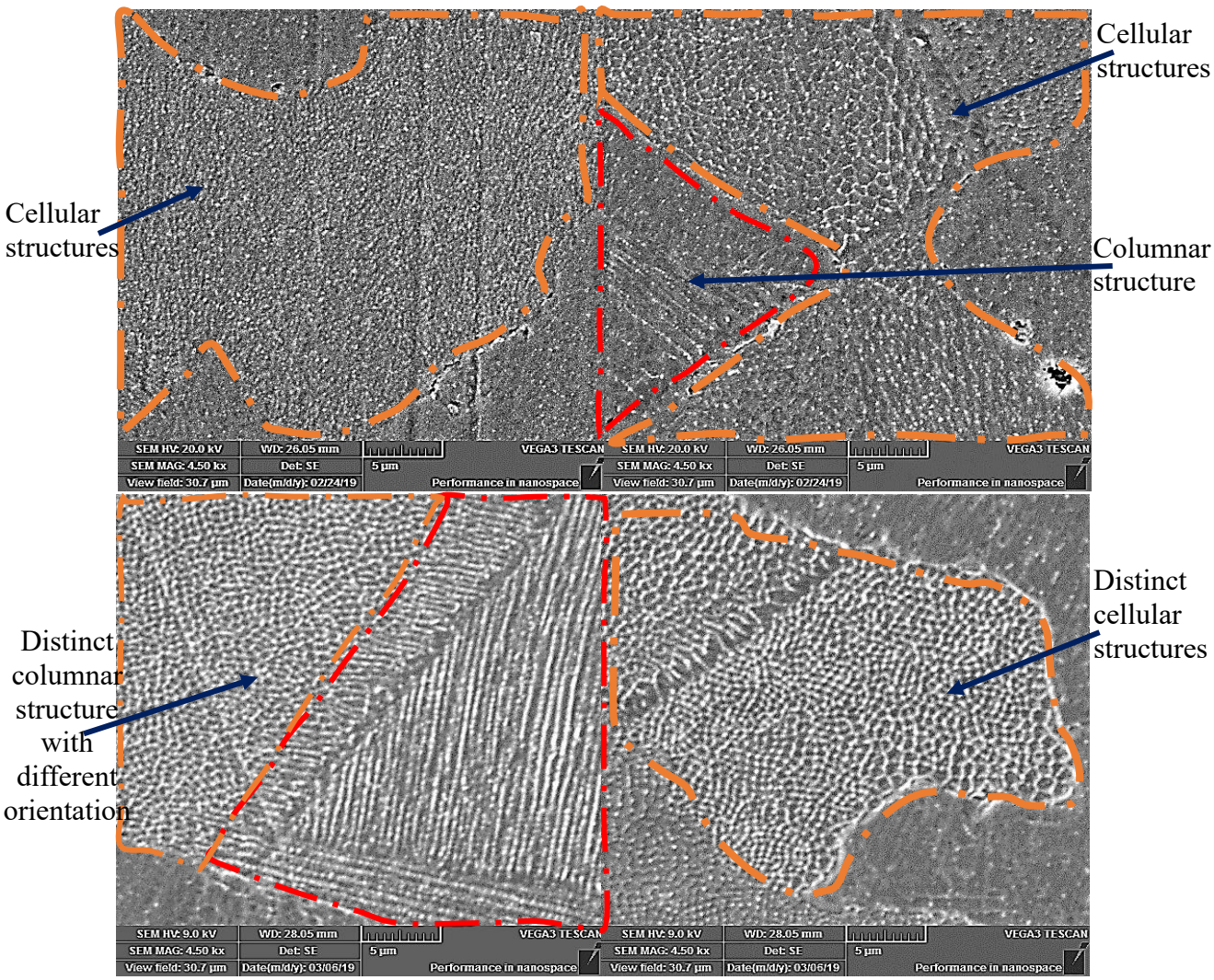

Figure 4-16: Effect of power on sub-grain structures a),b) Sample G4B2 with P=200W, h=0.14mm and v=750mm/s c),d) Sample G4B3 with P=200W,h=0.14mm and v=750mm/s

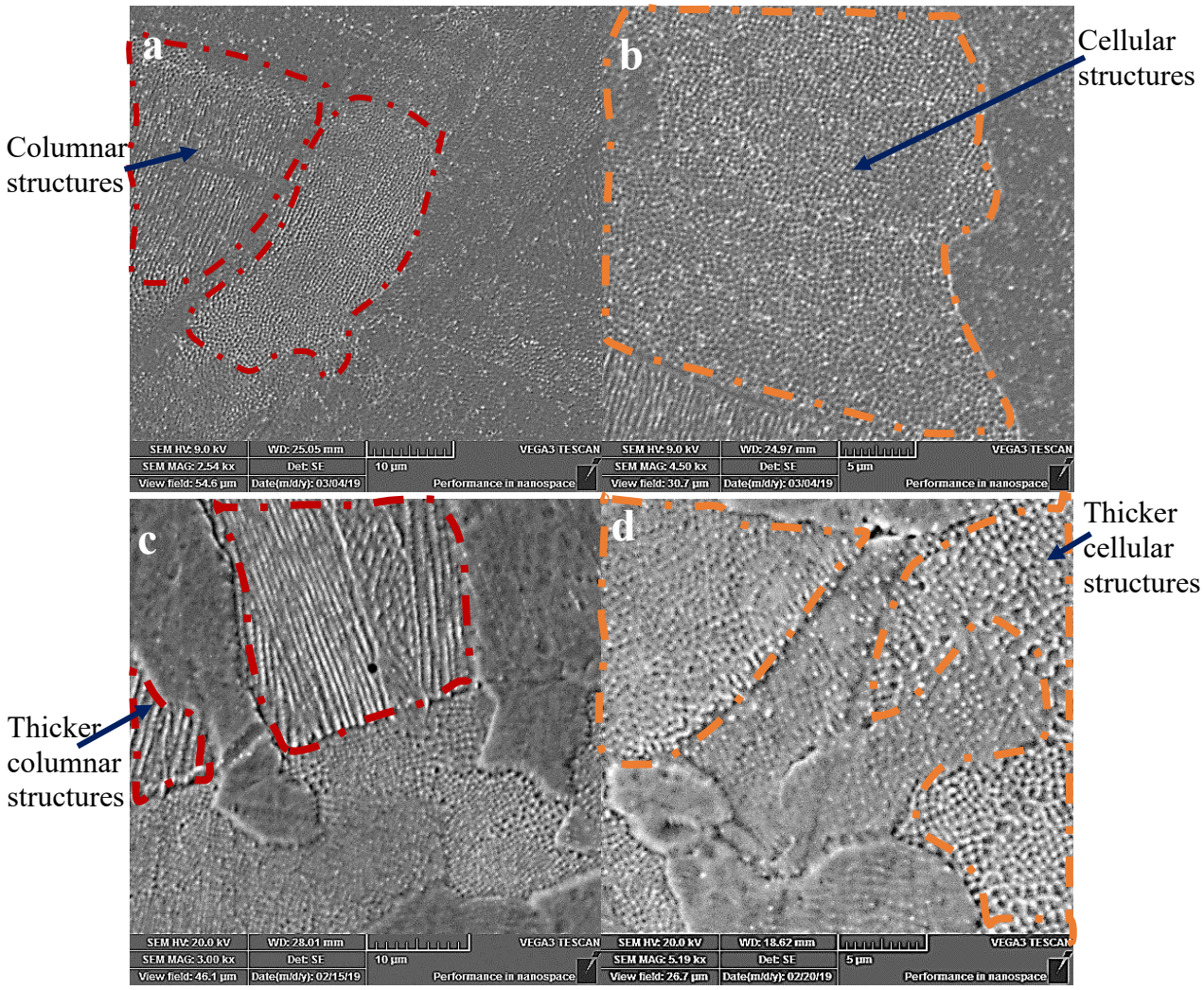

Figure 4-17: Effect of scanning speed on sub-grain structures a), b) Sample G1B2 with P=200W, h=0.08 mm and v=750mm/s c), d) Sample G1C2 with P=200W, h=0.08 mm and v=1250mm/s

In addition, the boundaries of the substructures become thicker and well-defined as the scanning speed increases as shown in Figure 4-17. For example, the boundaries of the cellular and columnar structures become more distinct and thicker when the scan speed is increased by 66.7% from 750 mm/s to 1250 mm/s as shown in Figure 4-17c-d. On the other hand, as the hatch spacing is increased, the boundaries of the cellular and columnar structures become less distinct and thinner as shown in Figure 4-18. For example, the boundaries of the substructures become less distinct and thinner when the hatch space increases from 80 µm to 120 µm which is a 50% increase in scan line spacing.

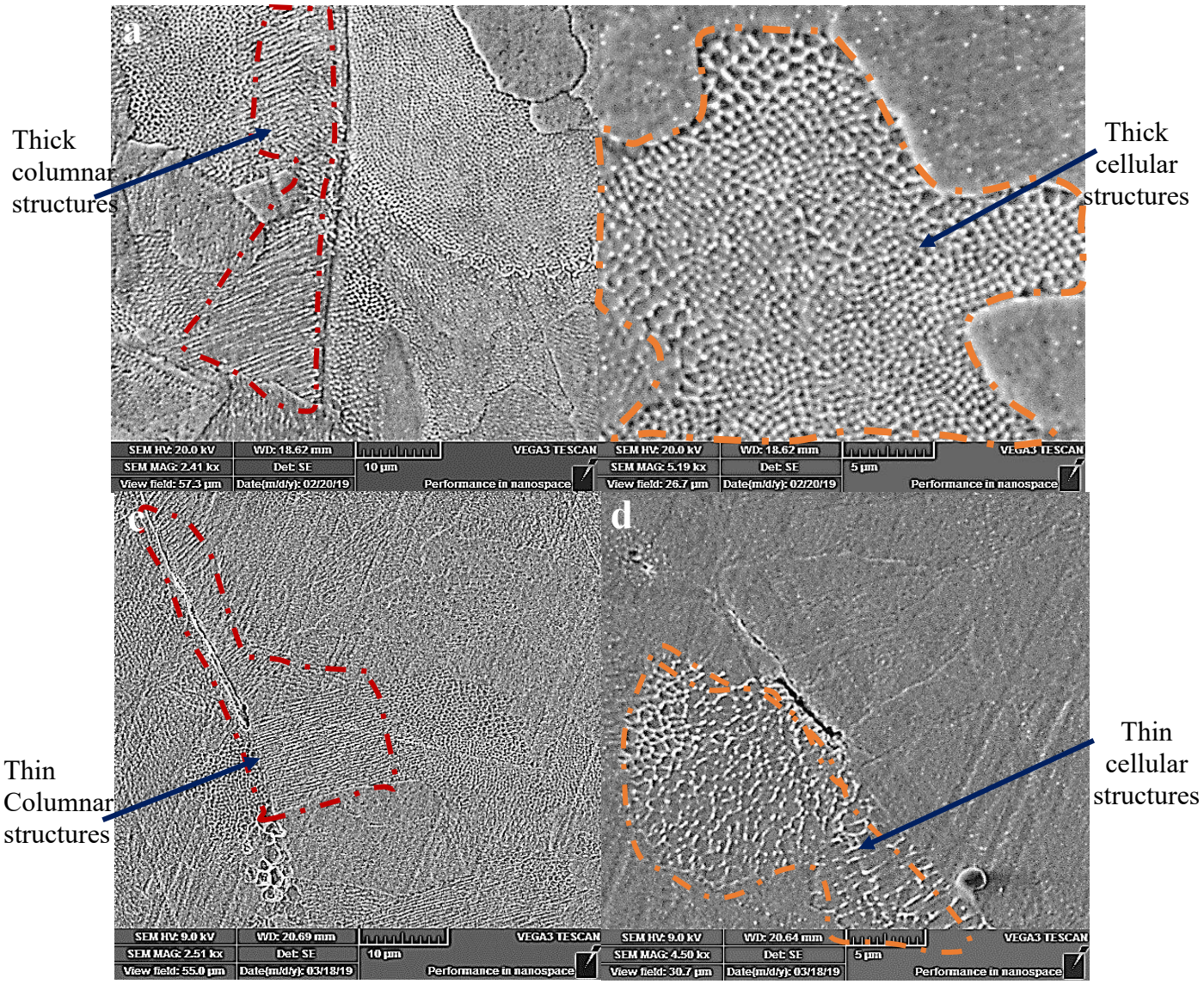

Figure 4-18: Effect of hatch spacing on sub-grain structures a), b) Sample G1C2 with P=200W, h=0.08 mm and v=1250mm/s c), d) Sample G3C2 with P=200W, h=0.12 mm and v=1250mm/s

The effect of the individual parameters on crack/debonding is also accessed. G1B2 showed no visible cracks but had micro pores aligned along a melt pool boundary as shown in Figure 4-19a. Increasing the scan speeds resulted in the formation of debonding cracks along melt pool boundaries as shown in Figure 4-19b. Increasing the hatching space of the same sample G1C2, introduced debonding cracks that traversed melt pool boundaries and joined together as shown by sample G3C2 in Figure 4-20b. Increasing the laser power reduces lack-of-fusion/debonding cracks seen in the sample, but at the same time, micro-cracks are formed on the grain boundary as well as within the grains themselves as shown in Figure 4-21c-d.

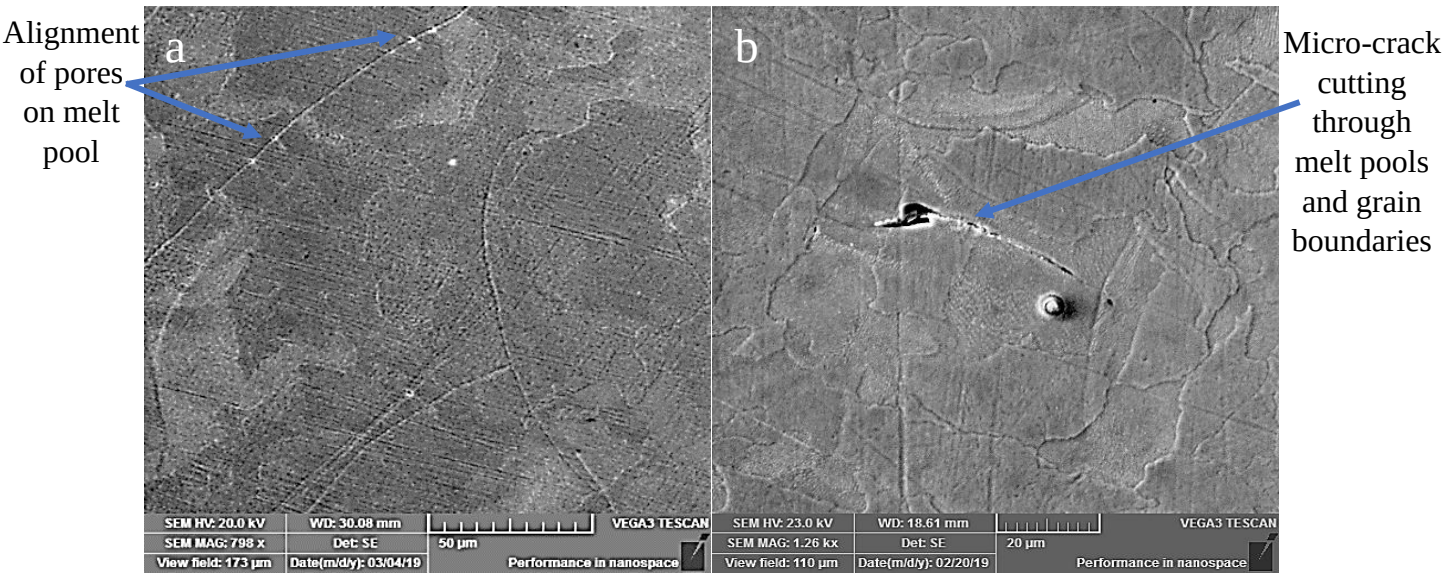

Figure 4-19: Effect of Speed on crack formation a) Sample G1B2 with P=200W, h=0.08 mm and v=750mm/s b) Sample G1C2 with P=200W, h=0.08 mm and v=1250mm/s

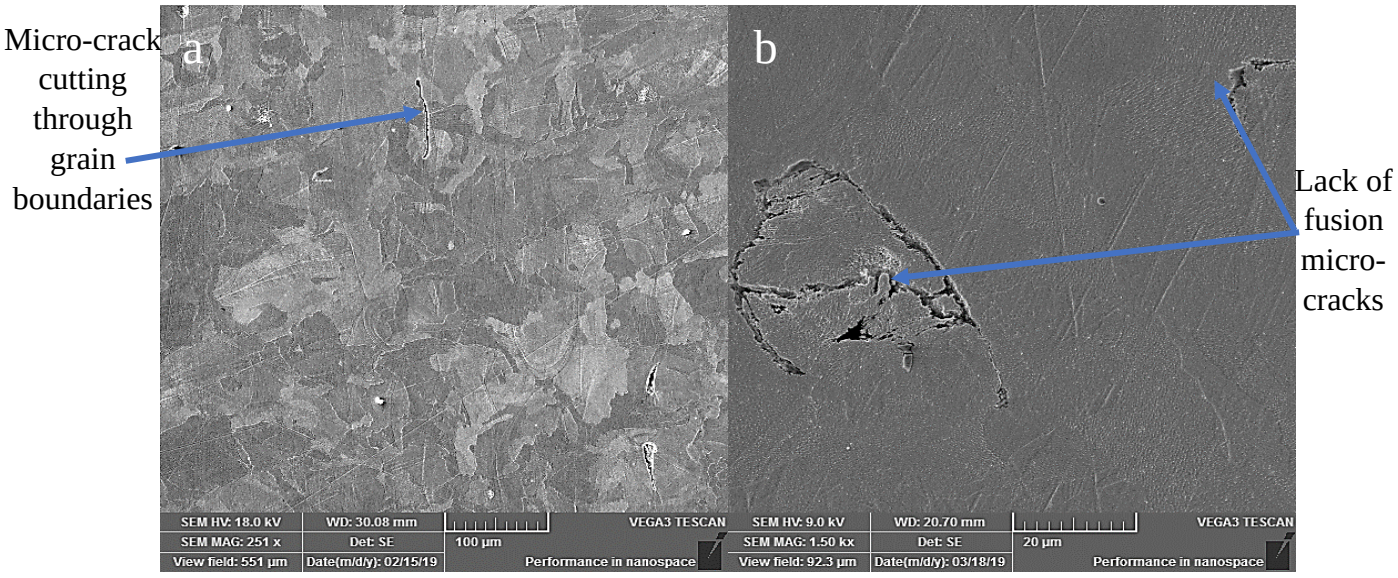

Figure 4-20: Effect of hatching space on crack formation a) Sample G1C2 with P=200W, h=0.08 mm and v=1250mm/s b) Sample G3C2 with P=200W, h=0.12 mm and v=1250mm/s

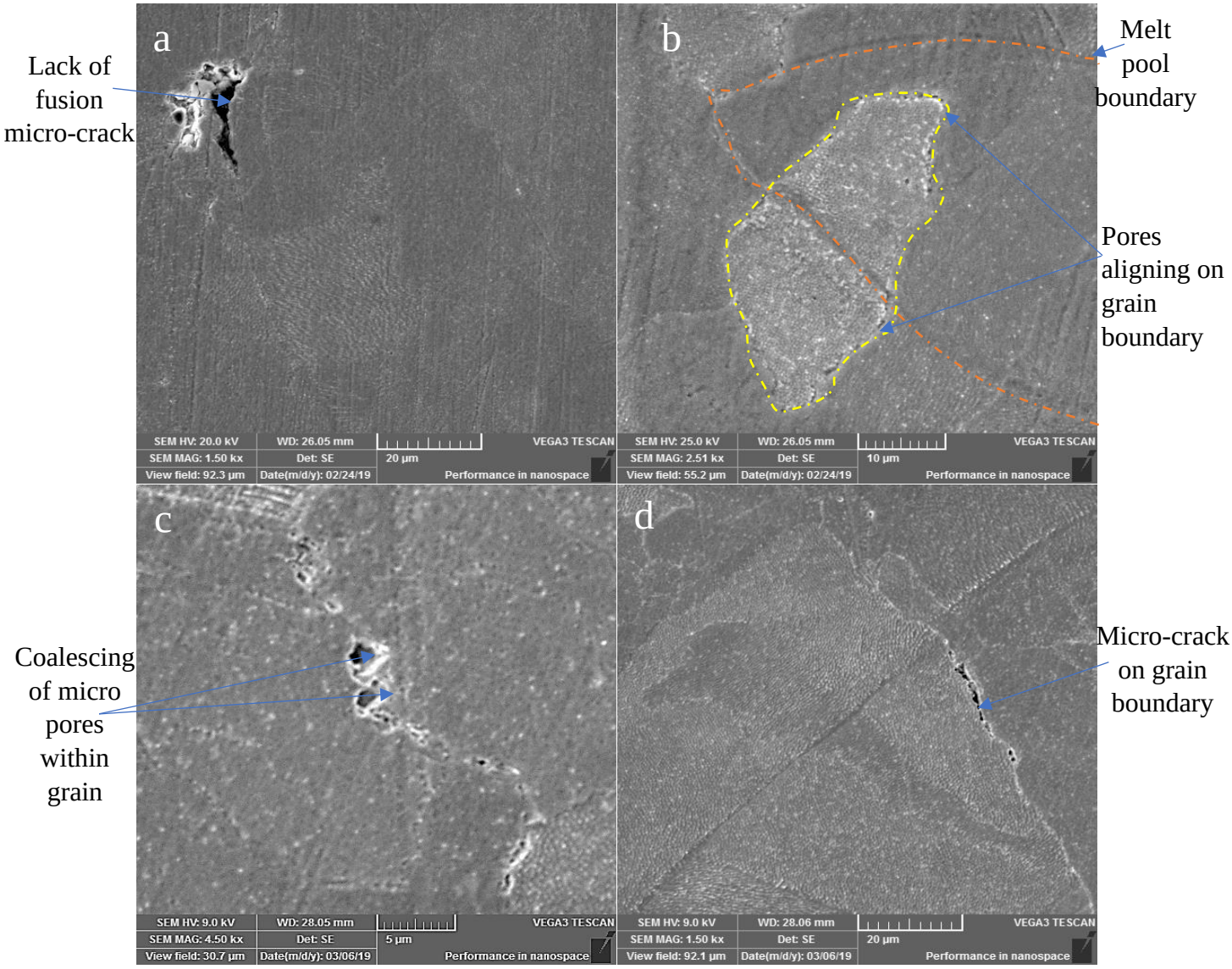

Figure 4-21: Effect of power on crack formation a), b) Sample G4B2 with P=200W, h=0.14 mm and v=750mm/s c), d) Sample G4B3 with P=250W, h=0.14 mm and v=750mm/s

4.4 **Surface Roughness and Wear Rate**

For structural applications, samples with less than 1% porosity are selected to undergo dry reciprocating wear tests, to access the effect of printing parameters on the wear properties of the samples. The roughness values of the samples prior to the wear test are measured with the OP and the values are presented in Table 4-3. The results shown for the roughness in Table 4-3 are below 50 nm which is in line with the ASTM standard for measuring wear properties. The 3D presentation of the roughness samples of a few of the samples is shown in Figure 4-22. Sample G4B2 recorded the lowest roughness values at 0.6340 nm whereas sample G3C2 recorded the highest value, at 1.8110 nm, among the eight different samples. The wear tracks

of four of the samples are scanned using the optical profilometer and the 3D representation of half of the tracks from the scans are shown in Figure 4-23.

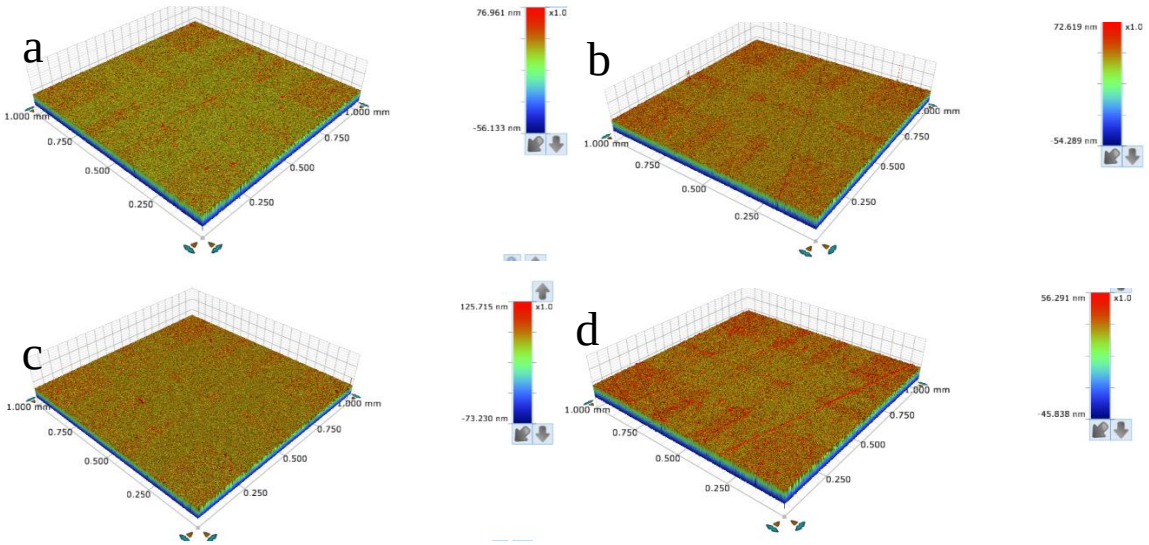

Figure 4-22: Roughness 3D representation of sample a) G1B2, b)G2B1 c)G4B2 d)G1C3

Table 4-3: Roughness of samples prior to Wear Testing

Sample	Roughness (S_a/ nm)
G4B3	0.6736±0.3012
G4B2	0.6340±0.3660
G3C2	1.8110±0.8099
G2B2	0.7020±0.3139
G2B1	0.6520±0.2916
G1C3	0.6984±0.3123
G1C2	0.7472±0.3342
G1B2	0.7162±0.3203

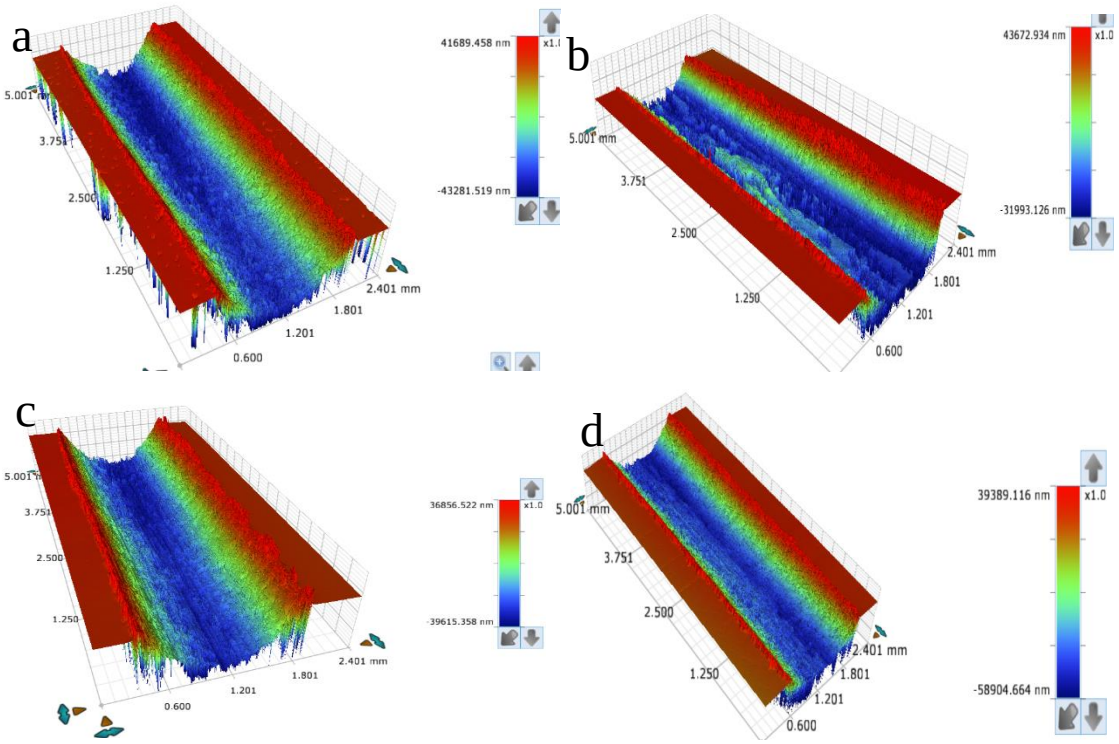

Figure 4-23: Wear tracks of samples after wear a)G3C2 b)G4B3 c)G2B2 d)G1C3

4.4.1 Influence of Printing Parameters on Wear

The mass loss in grams of the 8 samples used for the wear tests is shown in Figure 4-24 as well as the wear tracks for four of the samples are shown in Figure 4-23. Sample G4B3 is the one with the least mass loss at 27 x 10^{-4} g and Sample G4B2 had the highest mass loss of 42 x 10^{-4} g which is a difference of 74%.

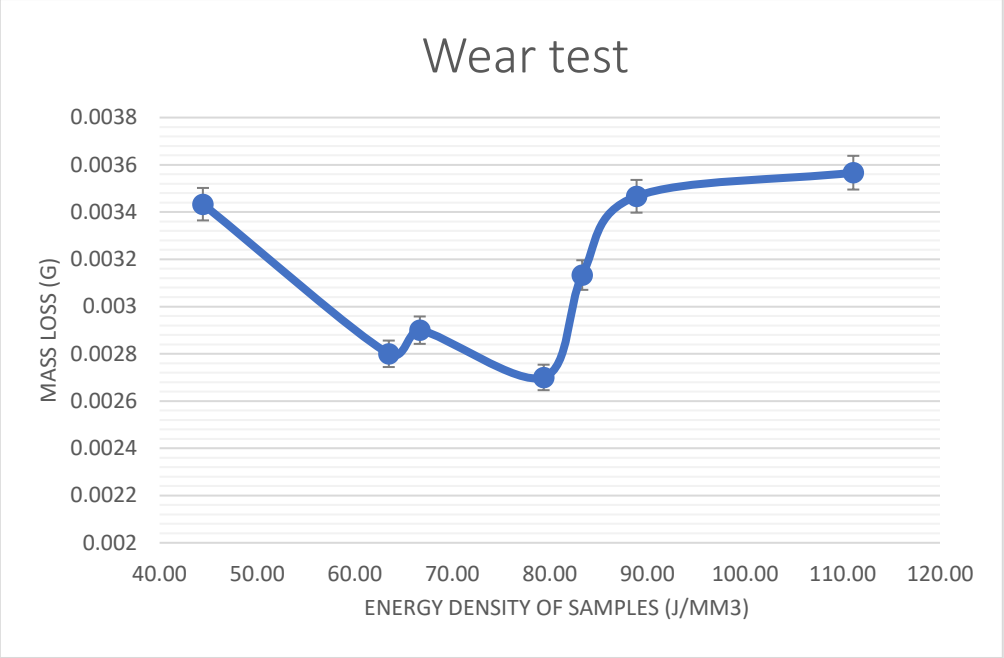

Figure 4-24: Mass loss for all samples

The effect of laser power on the mass is loss is investigated and the changes can be seen in Figure 4-25. Figure 4-25a shows the effect of laser power on the mass loss of samples in group 1, with a hatch spacing of 80 µm. An increase in power from 200 -250 W, a 25% increase leads to a 6.9% increase in mass loss form (29 to 31) x 10^{-4} g. A mass loss for groups 2 and 3 samples showed a reverse response to an increase in power as seen in Figure 4-25b when a 25% increase in power for samples in group 3 (from 200-250 W) led to 35.7% drop in mass loss.

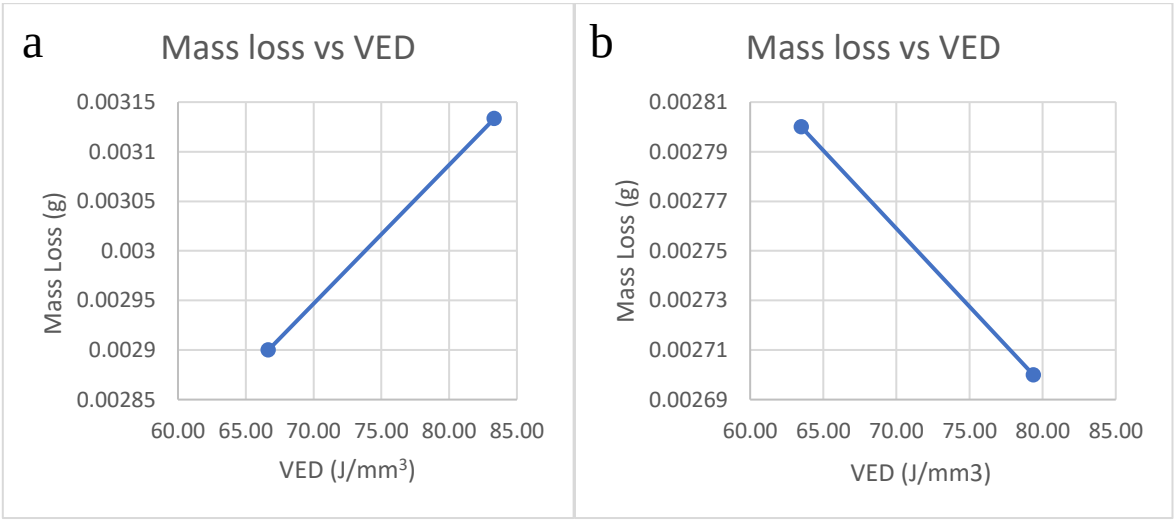

Figure 4-25: Effect of Power on mass loss using hatch spacing of a) 80 µm b)140 µm

Scan speed effect is accessed by observing the changes in samples G1B2 and G1C2. An increase in speed consequently means a reduction in VED. In Figure 4-26, a 66.7% increase in speed leads to a 13.9% decrease in mass loss is recorded as shown in Figure 4-26.

The influence of hatch spacing is also explored by looking at the mass loss changes of sample sets G1B2-G2B2 and G1C1-G3C2. An increase in hatch spacing from 80-100 µm, a 25% increase leads to a mass loss reduction of 5.6%. However, an increase from 80-120 µm leads to an increase in a mass loss by 17.2% as illustrated in Figure 4-27.

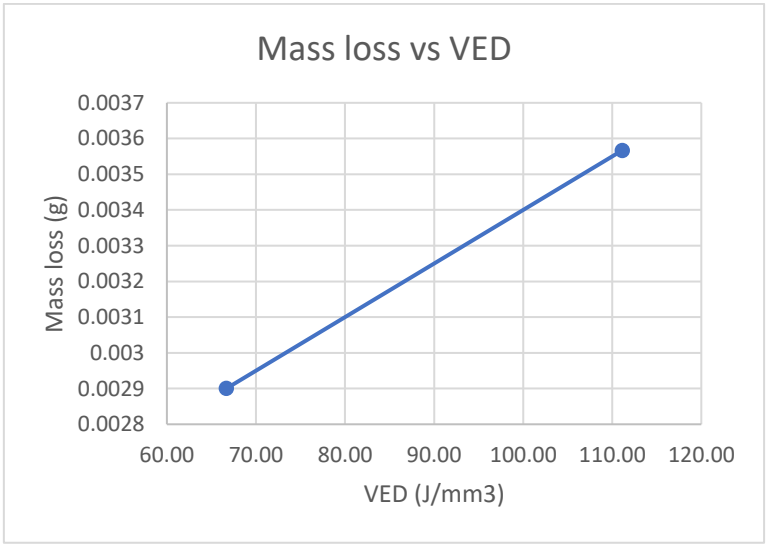

Figure 4-26: Effect of Speed on mass loss

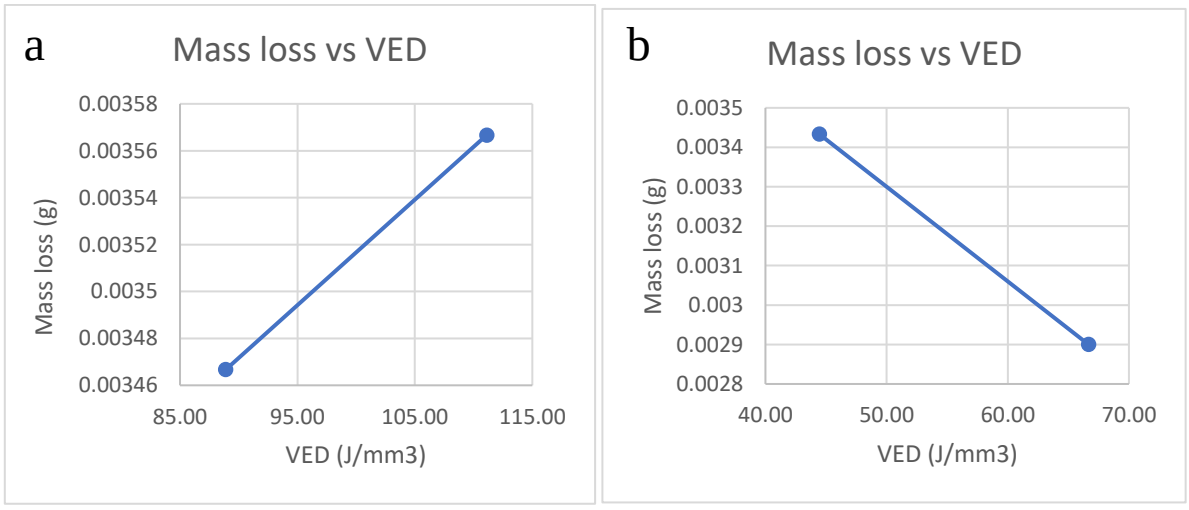

Figure 4-27: Effect of Hatch spacing on mass loss using speeds of a) 750 mm/s b)1250 mm/

Table 4-4: Wear results data

Sample	VED	Mass loss $x10^{-4}$ g	COF	Standard Deviation
G3C2	44.44	34	0.4654	0.2062
G4B2	63.49	42	0.4364	0.2108
G1C2	66.67	29	0.4273	0.2062
G2B1	66.67	40	0.4378	0.1714
G4B3	79.37	27	0.4688	0.2174
G1C3	83.33	31	0.4764	0.1968
G2B2	88.89	34	0.4778	0.1812
G1B2	111.11	36	0.4846	0.1755

5 DISCUSSION

The surface porosities of the samples were investigated using the combined effects of the varying printing parameters, referred to as the volumetric energy density (VED). The volumetric energy density quantified the amount of laser energy that is delivered per unit volume of the powders. Increasing VED means more energy is delivered to the metal powders which causes enough melting and therefore results in more of the powders fusing. There are two main forms of pores that are seen in metal-3D printed parts. Pores are formed either by incomplete fusion (lack of fusion pores) or as a result of entrapped gases. Lack of fusion pores are also sometimes referred to as process pores and are seen in parts with low VED. Vilaro et al [104] and Gong et al [57] both attributed lack-of-fusion pores to metal powders that do not fully melt and without enough overlap between the scan lines.

Gas pores are believed to be spherical due to trapped gases or introduced during the gas atomization process for preparing the metal powder feedstock [30]. Spherical pores are seen mostly in samples with high VED. Gong et al [57] attributed these gas spherical pores to high the VED due to material evaporation under high laser power or small hatch spacing. It is a known fact that fully consolidated parts are denser than parts that are partially or not fully consolidated. Therefore, samples with high VED should have higher densification than parts with low density. Part density is primarily affected by the introduction of pores taking up space that the feedstock material needs to occupy. This is confirmed by Yakout et al that the introduction of void formation and sometimes micro-segregation of some alloying elements reduce the part density [52]. Pores are introduced at two different stages during printing where Low VED leads to lack of fusion holes while high VED results in gas pores which contribute to the reduction in the density of the part. Having the right amount of VED creates more material per unit volume and fewer pores, thus increasing the amount per unit volume[52]. In this study, it was observed that the printed material had its maximum density at VED of 111.11 J/mm3 and lowest density at VED 20.41 J/mm^3.

It should be noted that the Archimedes principle for determining the part density is not the most reliable way of determining the density of the printed parts. This is because the pores or cracks are filled with unmelted powders which do not entirely form part of the structure but registers in determining the mass of the part [105]. The buoyancy of porous parts can also affect the final density calculation which requires that the sample pores be covered so the bubbles from

them do not affect the weight in water. According to the ASTM Standard B962-17, this step can be skipped if no observable bubbles are present when the sample is immersed in water.
The porosity calculation in the previous section is for surface pore determination and not, therefore, representative of the entire bulk of the sample. To find the entire pore distribution in 3D space a more accurate volumetric measurement technique should be employed

Porosity, as talked about in chapter 2, is a desirable property in medical orthopedics since the pores, when controlled, can be used to adjust the stiffness of the implants to match that of the bone in the limb without the implants. This way the weight of the patient is evenly distributed across both implant and bone. This prevents the implants from supporting a larger amount of the weight and leaving the bone to lesser weight. When this happens as the bone gets lesser weight applying pressure or force on it, it weakens to much the amount of weight that is applied to it. This phenomenon of the weakening of bone is what medical professionals call stress-shielding. Not only are pores required to control the stiffness/weight of medical implants, but they are required in implants so that the bone tissue and muscles can grow into them to thereby providing reinforcements to the implants. This is what is referred to in the medical field as Osseointegration [106]. Porous parts are not only desired in the medical field but can be used in structures such as filters, heat exchangers and cooling equipment [107][108]. The hardness values of most of the samples were higher than traditionally manufactured 316L samples. The lowest hardness was recorded at 208HV which is comparable to 316L parts manufactured by casting (210 HV) and the rest were higher than that value [109]. The hardness of the samples is not entirely dependent on the porosity of the part since in this study the hardness indents are controlled to not fall within the pores. This is because the presence of the pores makes the indents penetrate the sample deeper making a larger indent that translates to a lower HV value. For this experiment, the pores on the surface of the samples were intentionally avoided for each of the indentations made. This results in little correlation between the hardness and the surface porosity of the samples. There was no direct correlation between the VED and hardness of the printed parts. It was reported by Ghasri-Khouzani et al that for 316L stainless steel, the printing technique, as well as printing parameters, show little variation in the hardness of the parts [109]. Other factors that affect hardness is the presence of secondary phase particles and compositional changes [110].

The presence of unmelted/unfused powders, together with other defects such as porosity is found to reduce the mechanical properties of the fabricated metal parts [8]. The porosity

measurements with the aid of image processing have their own set of limitations, limitations with the thresholding method that introduces a little bias into the methodology. Also, very small tiny pores are not detected when the images have been taken through thresholding and makes it harder to find the porosity of samples with entirely tiny pores.

Generally, unmelted powders result in surface defects such as lack of fusion pores. The higher the VED during printing, the higher the supplied energy to the sample resulting in better fusion and consolidation of the powders [30]. Hebert et al suggested that the unmelted powders can also be a result of uneven powder spreading during the printing process [111]. The combined effect of the printing parameters has been well documented by a lot of studies but the effect of the individual parameters on the evolution of the microstructure is very lacking in the literature. All the as-printed samples had two separate substructures that evolved in the samples, columnar/lathe, and cellular structures. According to the principles of solidification, these substructures are evidence of the thermal cycles attributed to this type of manufacturing technology which exhibits fast solidification processes. It is also well documented that for 316L Stainless steel and with Direct Metal Laser Sintering process the sub-grain structures are bounded by ferrites. Therefore, the thicker these boundaries, the higher the amount of ferrite in the sample [38]. These substructures are prominent in the samples that receive high accumulation of heat in a short time over a relatively small area. Samples that had small hatch spacing or faster scan speeds are seen to be the samples with distinct cellular and columnar grains. Higher temperature rise leads to more diffusion occurring and as a result the particles within the grains grow bigger or thicker. Increasing the laser power and scan speed thicker and bigger boundaries while an increase in hatch spacing leads to less developed boundaries.

Cracks are usually formed as a result of residual stress due to the vast thermal gradient that the printing process introduces to the part during printing. Cracks can be along the grain or melt pool boundaries because these are high energy regions. Materials with low thermal conductivity and high thermal expansion are most susceptible to residual stress cracks because the accumulated thermal energies cannot easily be relieved without post-processing techniques. Usually, cracks form along the boundaries but when the thermal stress is high enough these cracks cut across grains (intragranular cracks). Generally, cracks may be reduced in AM fabricated parts by preheating the substrate which reduces the temperature gradients in the build chamber [30].

The surface friction during the test depends on various conditions such as containments, surface roughness due to surface asperities, humidity. The graph of the COF vs time shows the fraction history during the wear test as shown in Appendix A1-8. From the graphs, there is a region of low friction then followed by the break-in period which results in an increase in friction as the surface asperities are annihilated refer [112]. A steady region is then observed where the friction forces recorded are fairly stable. The COF recorded is the average friction recorded for over the entire 1000s as stipulated in the standard [113]. Individual parameters influence the formation of fine subgrain structures, the size and distribution of pore sizes and consequently these fine microstructures in addition to the pore distribution affects the tribological behavior of the samples. It is clear from the study that the sizes and distribution the pores cannot be predicted based on only the parameters studied here and therefore a volumetric analysis of the pores might reveal valuable insight into the matter. However, the sample that is best suited for structural purposes can easily be identified as the samples with very low porosity level and samples with globular shaped pores are more stable against crack formation and propagation.

The mass loss of the samples behaves very similarly to the hardness of the samples. This tells us that the controlling factors for mass loss and hardness are not entirely dependent on the VED. There is no discernible trend between the VED and the mass loss of the samples, but the individual parameters seem to affect the mass loss. Power has a positive relationship with the wear resistance of the samples when there is no overlap between adjacent scan lines such as the 100 and 140 µm hatch spacings. Small hatching that has overlap between scan lines, such as 80 µm hatch spacing, deteriorates the wear properties when the power input increased. Small hatch spacing causes intermittent re-melting when the laser beams of adjacent scan lines overlap which provides more energy input to the material.

6 CONCLUSION AND FUTURE WORK

6.1 Summary and Conclusion

In Metal-based Additive Manufacturing (AM) techniques such as the SLS, processing parameters and constituent powder materials produce microstructural heterogeneities which influence the properties and quality of the printed parts. It is critical to understand the effect of processing parameters and constituents on the microstructural evolution and properties of the printed parts to be able to produce unique microstructures with consistent properties from metal powders using AM processes. This study aimed to investigate how the individual printing parameters affect the microstructural integrity and properties of the printed parts. The main findings from this work are as follows:

1. Increasing the VED increases the part density, reduces the number of pores and the number of unmelts in the sample. Extremely high VED has a reverse effect on the pores, unmelts and resulting density of the printed part. A highly densified part is produced using a VED range of 40 and 110 J/mm3 for structural application. Porous structures for use in a biomedical application or for heat exchangers can be fabricated using VED below and above the range.

2. Cracks are observed both on the macro and micro levels. The macro cracks are observed in samples with low VED (low power or high speeds or a combination of both). Extremely high VED shows micro-cracks aligned along grain boundaries and within grains as well.

3. The hardness of laser-sintered part is high than the conventional manufacturing techniques such as casting and hot rolling. High hardness is attributed to the fine particle segregation and oxide nano inclusions formed as well as secondary phases present during the printing process. Hence, there was no observable trend with the VED and the hardness values of the samples.

4. Laser power and scan speeds affect the thickness as well as the spatial distribution of both the columnar and the cellular structure present in the sample. Increasing these parameters separately while maintaining the other parameters at a constant value increases the size and reduces the spatial distribution of these substructures.

6. Hatching spacing affects the size of the boundaries the same as the laser power and scan speed but has a non-consistent effect on the spatial distribution of each of the microstructure

substructure. The thickness of the boundaries is reduced as the hatch spacing is increased, but the columnar structures densely packed as opposed to the cellular structure exhibiting lower spatial distribution.

7. The wear properties of the samples are primarily dependent on the hardness of the samples. Generally, a sample with higher hardness shows better wear properties.

6.2 Future Work

The relationship between printing parameters and microstructure for different applications of Laser sintered parts has been explored extensively in this research work. For the future, more work needs to be conducted to comprehensively understand how microstructure affects other mechanical behaviors. The proposed future works are presented as follows:

1. The pore shapes affect the mechanical behavior of sintered parts. The introduction of pores in medical implants is desirable but how many pores can be induced into the parts and still be able to support the weight of a patient. What pore shapes are more stable and resistant to crack formation and propagation using a more volumetric characterization method.

2. When 3D printed 316L is used in implants or components in parts that are experience moderate to high strain rate impact, the dynamic behavior will be entirely different from the quasi-static responses. It is important to study how microstructure influences the dynamic response of these parts.

3. The corrosion responses of 3D printed 316L is also an interesting area to delved into by exploring how the individual parameters are either improving or deteriorating this chemical behavior.

4. Developing a model that will be able to predict the approximate microstructure and mechanical responses of a final 3D printed 316L part based on the individual parameter specifications. A model that can state the regimes where the properties of the material might lie as vague as if the pores induced might be stable or not, or if the specified laser power requires a low hatch spacing in combination with high speed.

5. The optimized/stable VED can be feed into an Artificial Neural Network in order to give out optimized parameters based on requirements or limitations in order to prevent future guesswork of combining printing parameters and going through the painstaking process of studying the effect of parameter on microstructure.

7 REFERENCES

[1] N. Guo and M. C. Leu, “Additive manufacturing: Technology, applications and research needs,” *Front. Mech. Eng.*, vol. 8, no. 3, pp. 215–243, 2013.

[2] O. L. A. Harrysson, O. Cansizoglu, D. J. Marcellin-Little, D. R. Cormier, and H. A. West, “Direct metal fabrication of titanium implants with tailored materials and mechanical properties using electron beam melting technology,” *Mater. Sci. Eng. C*, vol. 28, no. 3, pp. 366–373, Apr. 2008.

[3] A. A. Al-Tamimi, P. R. A. Fernandes, C. Peach, G. Cooper, C. Diver, and P. J. Bartolo, “Metallic bone fixation implants: a novel design approach for reducing the stress shielding phenomenon,” *Virtual Phys. Prototyp.*, vol. 12, no. 2, pp. 141–151, 2017.

[4] Q. Yan *et al.*, “A Review of 3D Printing Technology for Medical Applications,” *Engineering*, 2018.

[5] J. S. Zuback and T. DebRoy, “The hardness of additively manufactured alloys,” *Materials (Basel).*, vol. 11, no. 11, 2018.

[6] D. Manfredi *et al.*, “Direct Metal Laser Sintering: An additive manufacturing technology ready to produce lightweight structural parts for robotic applications,” *Metall. Ital.*, vol. 105, no. 10, pp. 15–24, 2013.

[7] M. N. Jahangir, M. A. H. Mamun, and M. P. Sealy, “A Review ofAdditive Manufacturing,” *AIP Conf. Proc.*, vol. 1980, 2018.

[8] S. M. Yusuf and N. Gao, “Influence of energy density on metallurgy and properties in metal additive manufacturing,” *Mater. Sci. Technol. (United Kingdom)*, vol. 33, no. 11, pp. 1269–1289, 2017.

[9] S. Yusuf, Y. Chen, R. Boardman, S. Yang, and N. Gao, “Investigation on Porosity and Microhardness of 316L Stainless Steel Fabricated by Selective Laser Melting,” *Metals (Basel).*, vol. 7, no. 2, p. 64, 2017.

[10] J. Kruth, J. Deckers, E. Yasa, and R. Wauthle, “Assessing and comparing influencing factors of residual stresses in selective laser melting using a novel analysis method,” vol. 226, no. 6, pp. 980–991, 2012.

[11] Y. Liu, Y. Yang, and D. Wang, “A study on the residual stress during selective laser melting (SLM) of metallic powder,” *Int. J. Adv. Manuf. Technol.*, vol. 87, no. 1–4, pp. 647–656, 2016.

[12] T. Kurzynowski, K. Gruber, W. Stopyra, B. Kuźnicka, and E. Chlebus, “Correlation between process parameters, microstructure and properties of 316 L stainless steel

processed by selective laser melting," *Mater. Sci. Eng. A*, vol. 718, no. January, pp. 64–73, 2018.

[13] O. L. A. Harrysson, O. Cansizoglu, D. J. Marcellin-little, D. R. Cormier, and H. A. West, "Direct metal fabrication of titanium implants with tailored materials and mechanical properties using electron beam melting technology," vol. 28, pp. 366–373, 2008.

[14] W. Xu *et al.*, "Additive manufacturing of strong and ductile Ti-6Al-4V by selective laser melting via in situ martensite decomposition," *Acta Mater.*, vol. 85, pp. 74–84, 2015.

[15] "ASTM International Forms New Standards Committee on Additive Manufacturing - Society of Manufacturing Engineers (SME) Partners with ASTM On First-of-Its Kind Industry Activity | www.astm.org." [Online]. Available: https://www.astm.org/cms/drupal-7.51/newsroom/astm-international-forms-new-standards-committee-additive-manufacturing-society. [Accessed: 05-Apr-2019].

[16] D. Augusto De Moraes and A. Czekanski, "the Influence of Powder Size and Packing Density on the Temperature Distribution in Selective Laser Melting," pp. 1–9, 2018.

[17] C. Weingarten, D. Buchbinder, N. Pirch, W. Meiners, K. Wissenbach, and R. Poprawe, "Formation and reduction of hydrogen porosity during selective laser melting of AlSi10Mg," *J. Mater. Process. Technol.*, vol. 221, pp. 112–120, 2015.

[18] C. Kamath, B. El-Dasher, G. F. Gallegos, W. E. King, and A. Sisto, "Density of additively-manufactured, 316L SS parts using laser powder-bed fusion at powers up to 400 W," *Int. J. Adv. Manuf. Technol.*, vol. 74, no. 1–4, pp. 65–78, 2014.

[19] I. Yadroitsev, I. Yadroitsau, and I. Yadroitsev, "Selective laser melting: Direct manufacturing of 3D-objects by selective laser melting of metal powders," *Appl. Catal. B Environ.*, vol. 75, no. 3–4, pp. 229–238, 2009.

[20] C. Kusuma, "The effect of laser power and scan speed on melt pool characteristics of pure Titanium and Ti-6Al-4V alloy for selective laser melting," p. 127, 2014.

[21] A. Cooke and J. Slotwinski, "Properties of metal powders for additive manufacturing: A review of the state of the art of metal powder property testing," *Addit. Manuf. Mater. Stand. Test. Appl.*, pp. 21–48, 2015.

[22] J. Chao, C. Capdevila, M. Serrano, A. Garcia-Junceda, J. A. Jimenez, and M. K. Miller, "Effect of α-α' phase separation on notch impact behavior of oxide dispersion strengthened (ODS) Fe20Cr5Al alloy," *Mater. Des.*, vol. 53, pp. 1037–1046, 2014.

[23] A. Mertens, *Additive manufacturing of metallic materials: an Introduction*. Elsevier

Inc., 2016.

[24] W. J. Sames, F. A. List, S. Pannala, R. R. Dehoff, and S. S. Babu, “The Metallurgy and Processing Science of Metal,” p. 302, 2016.

[25] P. Jan, “‘ UNITED .sTAT-Es PATENT -,” vol. 12, no. 19, pp. 2–4, 1943.

[26] “30 years of EOS.” [Online]. Available: https://30years.eos.info/en. [Accessed: 10-Nov-2019].

[27] T. Duda and L. V. Raghavan, “3D Metal Printing Technology,” *IFAC-PapersOnLine*, 2016.

[28] D. Herzog, V. Seyda, E. Wycisk, and C. Emmelmann, “Additive manufacturing of metals,” *Acta Mater.*, vol. 117, pp. 371–392, 2016.

[29] Y. Zhang *et al.*, “Additive Manufacturing of Metallic Materials: A Review,” *J. Mater. Eng. Perform.*, vol. 27, no. 1, pp. 1–13, 2017.

[30] B. Zhang, Y. Li, and Q. Bai, “Defect Formation Mechanisms in Selective Laser Melting: A Review,” *Chinese J. Mech. Eng. (English Ed.*, vol. 30, no. 3, pp. 515–527, 2017.

[31] T. M. Mower and M. J. Long, “Mechanical behavior of additive manufactured, powder-bed laser-fused materials,” *Mater. Sci. Eng. A*, vol. 651, pp. 198–213, 2016.

[32] C. Qiu, N. J. E. Adkins, and M. M. Attallah, “Microstructure and tensile properties of selectively laser-melted and of HIPed laser-melted Ti-6Al-4V,” *Mater. Sci. Eng. A*, vol. 578, pp. 230–239, 2013.

[33] M. Simonelli, Y. Y. Tse, and C. Tuck, “The formation of α + β microstructure in as-fabricated selective laser melting of Ti-6Al-4V,” *J. Mater. Res.*, vol. 29, no. 17, pp. 2028–2035, 2014.

[34] T. Vilaro, C. Colin, and J. D. Bartout, “As-fabricated and heat-treated microstructures of the Ti-6Al-4V alloy processed by selective laser melting,” *Metall. Mater. Trans. A Phys. Metall. Mater. Sci.*, vol. 42, no. 10, pp. 3190–3199, 2011.

[35] H. Galarraga, D. A. Lados, R. R. Dehoff, M. M. Kirka, and P. Nandwana, “Effects of the microstructure and porosity on properties of Ti-6Al-4V ELI alloy fabricated by electron beam melting (EBM),” *Addit. Manuf.*, vol. 10, pp. 47–57, 2016.

[36] R. P. Mudge and N. R. Wald, “Laser engineered net shaping advances additive manufacturing and repair,” *Weld. J. (Miami, Fla)*, vol. 86, no. 1, pp. 44–48, 2007.

[37] D. A. D. E. Moraes, “Thermal Fe Analysis of Powder Bed Fusion Process : Power Input Evaluation and Parameter Sensitivity a Thesis Submitted To the Faculty of Graduate Studies in Partial Fulfillment of the Requirements for the Degree of Master

of Science Graduate Program in Me," no. August, 2018.

[38] M. Ziętala *et al.*, "The microstructure, mechanical properties and corrosion resistance of 316 L stainless steel fabricated using laser engineered net shaping," *Mater. Sci. Eng. A*, vol. 677, pp. 1–10, 2016.

[39] G. N. Levy, R. Schindel, and J. P. Kruth, "Rapid manufacturing and rapid tooling with layer manufacturing (LM) technologies, state of the art and future perspectives," *CIRP Ann. - Manuf. Technol.*, 2003.

[40] S. Masurtschak, R. J. Friel, A. Gillner, J. Ryll, and R. A. Harris, "Fiber laser induced surface modification/manipulation of an ultrasonically consolidated metal matrix," *J. Mater. Process. Technol.*, vol. 213, no. 10, pp. 1792–1800, 2013.

[41] A. Hehr, J. Wenning, K. Terrani, S. S. Babu, and M. Norfolk, "Five-Axis Ultrasonic Additive Manufacturing for Nuclear Component Manufacture," *Jom*, vol. 69, no. 3, pp. 485–490, 2017.

[42] M. Attaran, "The rise of 3-D printing: The advantages of additive manufacturing over traditional manufacturing," *Bus. Horiz.*, vol. 60, no. 5, pp. 677–688, 2017.

[43] K.-U. Bletzinger and E. Ramm, "Structural optimization and form finding of light weight structures," *Comput. Struct.*, vol. 79, pp. 2053–2062, 2001.

[44] S. Ford and M. Despeisse, "Additive manufacturing and sustainability: an exploratory study of the advantages and challenges," *J. Clean. Prod.*, vol. 137, pp. 1573–1587, 2016.

[45] R. E. Schafrik, D. D. Ward, and J. R. Groh, "Application of Alloy 718 in GE Aircraft Engines : Past , Present and Next Five Years."

[46] N. R. Muktinutalapati, "Materials for Gas Turbines – An Overview," 2006.

[47] S. Daneshmand, R. Adelnia, and S. Aghanajafi, "Design and production of wind tunnel testing models with selective laser sintering technology using glass-reinforced nylon," in *Materials Science Forum*, 2006, vol. 532–533, pp. 653–656.

[48] "Additive Manufacturing Systems 3D Printing Electronics Metals." [Online]. Available: https://www.optomec.com/. [Accessed: 20-Nov-2019].

[49] J. Tuomi, K. Paloheimo, and M. Salmi, "Surgical Innovation," no. September, 2014.

[50] M. Javaid and A. Haleem, "Additive manufacturing applications in medical cases : A literature based review," *Alexandria J. Med.*, vol. 54, no. 4, pp. 411–422, 2018.

[51] P. Heinl, L. Müller, C. Körner, R. F. Singer, and F. A. Müller, "Cellular Ti–6Al–4V structures with interconnected macro porosity for bone implants fabricated by selective electron beam melting," *Acta Biomater.*, vol. 4, no. 5, pp. 1536–1544, Sep. 2008.

[52] M. Yakout, M. A. Elbestawi, and S. C. Veldhuis, “Density and mechanical properties in selective laser melting of Invar 36 and stainless steel 316L,” *J. Mater. Process. Technol.*, vol. 266, no. October 2018, pp. 397–420, 2019.

[53] U. Scipioni Bertoli, A. J. Wolfer, M. J. Matthews, J. P. R. Delplanque, and J. M. Schoenung, “On the limitations of Volumetric Energy Density as a design parameter for Selective Laser Melting,” *Mater. Des.*, vol. 113, pp. 331–340, 2017.

[54] K. Kempen, L. Thijs, J. Van Humbeeck, and J. P. Kruth, “Processing AlSi10Mg by selective laser melting: Parameter optimisation and material characterisation,” *Mater. Sci. Technol. (United Kingdom)*, vol. 31, no. 8, pp. 917–923, 2015.

[55] E. Liverani, S. Toschi, L. Ceschini, and A. Fortunato, “Effect of selective laser melting (SLM) process parameters on microstructure and mechanical properties of 316L austenitic stainless steel,” *J. Mater. Process. Technol.*, vol. 249, no. June, pp. 255–263, 2017.

[56] N. Read, W. Wang, K. Essa, and M. M. Attallah, “Selective laser melting of AlSi10Mg alloy: Process optimisation and mechanical properties development,” *Mater. Des.*, vol. 65, pp. 417–424, 2015.

[57] H. Gong, K. Rafi, H. Gu, T. Starr, and B. Stucker, “Analysis of defect generation in Ti–6Al–4V parts made using powder bed fusion additive manufacturing processes,” *Addit. Manuf.*, vol. 1–4, pp. 87–98, Oct. 2014.

[58] D. Gu *et al.*, “Densification behavior, microstructure evolution, and wear performance of selective laser melting processed commercially pure titanium,” *Acta Mater.*, vol. 60, no. 9, pp. 3849–3860, 2012.

[59] R. Li, Y. Shi, Z. Wang, L. Wang, J. Liu, and W. Jiang, “Densification behavior of gas and water atomized 316L stainless steel powder during selective laser melting,” *Appl. Surf. Sci.*, vol. 256, no. 13, pp. 4350–4356, 2010.

[60] L. N. Carter, M. M. Attallah, and R. C. Reed, “Laser Powder Bed Fabrication of Nickel-Base Superalloys: Influence of Parameters$\mathsemicolon$ Characterisation, Quantification and Mitigation of Cracking,” in *Superalloys 2012*, John Wiley & Sons, Inc., 2012, pp. 577–586.

[61] L. N. Carter, K. Essa, and M. M. Attallah, “Optimisation of selective laser melting for a high temperature Ni-superalloy,” *Rapid Prototyp. J.*, vol. 21, no. 4, pp. 423–432, 2015.

[62] W. J. Sames, F. A. List, S. Pannala, R. R. Dehoff, and S. S. Babu, “The metallurgy and processing science of metal additive manufacturing,” *Int. Mater. Rev.*, vol. 61, no. 5,

pp. 315–360, 2016.

[63] E. A. Jägle, P. P. Choi, J. Van Humbeeck, and D. Raabe, “Precipitation and austenite reversion behavior of a maraging steel produced by selective laser melting,” *J. Mater. Res.*, vol. 29, no. 17, pp. 2072–2079, 2014.

[64] K. Kempen, E. Yasa, L. Thijs, J. P. Kruth, and J. Van Humbeeck, “Microstructure and mechanical properties of selective laser melted 18Ni-300 steel,” *Phys. Procedia*, vol. 12, no. PART 1, pp. 255–263, 2011.

[65] B. Song *et al.*, “Differences in microstructure and properties between selective laser melting and traditional manufacturing for fabrication of metal parts: A review,” *Front. Mech. Eng.*, vol. 10, no. 2, pp. 111–125, Jun. 2015.

[66] X. Zhao, B. Song, Y. Zhang, X. Zhu, Q. Wei, and Y. Shi, “Decarburization of stainless steel during selective laser melting and its influence on Young’s modulus, hardness and tensile strength,” *Mater. Sci. Eng. A*, vol. 647, pp. 58–61, 2015.

[67] K. Abd-Elghany and D. L. Bourell, “Property evaluation of 304L stainless steel fabricated by selective laser melting,” *Rapid Prototyp. J.*, vol. 18, no. 5, pp. 420–428, 2012.

[68] L. Facchini, N. Vicente, I. Lonardelli, E. Magalini, P. Robotti, and M. Alberto, “Metastable austenite in 17-4 precipitation-hardening stainless steel produced by selective laser melting,” *Adv. Eng. Mater.*, vol. 12, no. 3, pp. 184–188, 2010.

[69] J. D. Majumdar, A. Pinkerton, Z. Liu, I. Manna, and L. Li, “Microstructure characterisation and process optimization of laser assisted rapid fabrication of 316L stainless steel,” *Appl. Surf. Sci.*, vol. 247, no. 1–4, pp. 320–327, 2005.

[70] P. G. E. Jerrard, L. Hao, and K. E. Evans, “Experimental investigation into selective laser melting of austenitic and martensitic stainless steel powder mixtures,” *Proc. Inst. Mech. Eng. Part B J. Eng. Manuf.*, vol. 223, no. 11, pp. 1409–1416, 2009.

[71] R. Li, J. Liu, Y. Shi, M. Du, and Z. Xie, “316L Stainless Steel with Gradient Porosity Fabricated by Selective Laser Melting,” *J. Mater. Eng. Perform.*, vol. 19, no. 5, pp. 666–671, Jul. 2010.

[72] United Performance Metals, “Stainless 316, 316L, 317, 317L,” vol. 316, pp. 316–318, 2018.

[73] S. Bhattacharya, G. P. Dinda, A. K. Dasgupta, and J. Mazumder, “Microstructural evolution of AISI 4340 steel during Direct Metal Deposition process,” *Mater. Sci. Eng. A*, vol. 528, no. 6, pp. 2309–2318, 2011.

[74] X. Chen, J. Li, X. Cheng, H. Wang, and Z. Huang, “Effect of heat treatment on

microstructure, mechanical and corrosion properties of austenitic stainless steel 316L using arc additive manufacturing," *Mater. Sci. Eng. A*, vol. 715, no. October 2017, pp. 307–314, 2018.

[75] M. Jamshidinia, A. Sadek, W. Wang, and S. Kelly, "Additive Manufacturing of Steel Alloys Using Laser Powder-Bed Fusion," *Adv. Mater. Process.*, vol. 173, pp. 20–24, 2015.

[76] A. S. Haselhuhn, B. Wijnen, G. C. Anzalone, P. G. Sanders, and J. M. Pearce, "In situ formation of substrate release mechanisms for gas metal arc weld metal 3-D printing," *J. Mater. Process. Technol.*, vol. 226, pp. 50–59, 2015.

[77] J. Sander, J. Hufenbach, L. Giebeler, H. Wendrock, U. Kühn, and J. Eckert, "Microstructure and properties of FeCrMoVC tool steel produced by selective laser melting," *Mater. Des.*, vol. 89, pp. 335–341, 2016.

[78] C. Denis, "Characterization of H13 steel produced via electron beam melting," *Rapid Prototyp. J.*, vol. 10, no. 1, pp. 35–41, Jan. 2004.

[79] R. Cottam, J. Wang, and V. Luzin, "Characterization of microstructure and residual stress in a 3D H13 tool steel component produced by additive manufacturing," *J. Mater. Res.*, vol. 29, no. 17, pp. 1978–1986, 2014.

[80] A. Simchi and H. Asgharzadeh, "Densification and microstructural evaluation during laser sintering of M2 high speed steel powder," *Mater. Sci. Technol.*, vol. 20, no. 11, pp. 1462–1468, 2004.

[81] G. Casalino, S. L. Campanelli, N. Contuzzi, and A. D. Ludovico, "Experimental investigation and statistical optimisation of the selective laser melting process of a maraging steel," *Opt. Laser Technol.*, vol. 65, pp. 151–158, 2015.

[82] D. D. Gu, W. Meiners, K. Wissenbach, and R. Poprawe, "Laser additive manufacturing of metallic components: Materials, processes and mechanisms," *Int. Mater. Rev.*, vol. 57, no. 3, pp. 133–164, 2012.

[83] Z. L. Lu, Y. S. Shi, J. H. Liu, Y. Chen, and S. H. Huang, "Manufacturing AISI304 metal parts by indirect selective laser sintering combined with isostatic pressing," *Int. J. Adv. Manuf. Technol.*, vol. 39, no. 11, pp. 1157–1163, Dec. 2008.

[84] C. Y. Yap *et al.*, "Review of selective laser melting: Materials and applications," *Appl. Phys. Rev.*, vol. 2, no. 4, 2015.

[85] J. A. Cherry, H. M. Davies, S. Mehmood, N. P. Lavery, S. G. R. Brown, and J. Sienz, "Investigation into the effect of process parameters on microstructural and physical properties of 316L stainless steel parts by selective laser melting," *Int. J. Adv. Manuf.*

Technol., vol. 76, no. 5–8, pp. 869–879, 2014.

[86] R. L. Smith and G. E. Sandly, "An Accurate Method of Determining the Hardness of Metals, with Particular Reference to Those of a High Degree of Hardness," *Proc. Inst. Mech. Eng.*, vol. 102, no. 1, pp. 623–641, 1922.

[87] Z. Sun, X. Tan, S. B. Tor, and W. Y. Yeong, "Selective laser melting of stainless steel 316L with low porosity and high build rates," *Mater. Des.*, vol. 104, pp. 197–204, 2016.

[88] L. Thijs, F. Verhaeghe, T. Craeghs, J. Van Humbeeck, and J. P. Kruth, "A study of the microstructural evolution during selective laser melting of Ti-6Al-4V," *Acta Mater.*, vol. 58, no. 9, pp. 3303–3312, 2010.

[89] H. P. Jost, "Tribology: How a word was coined 40 years ago," *Tribol. Lubr. Technol.*, vol. 62, no. 3, pp. 24–28, 2006.

[90] P. L. K. Bhushan. Bharat, *Introduction to tribology*. John Wiley and Sons, 2002.

[91] S. Affatato and L. Grillini, *Topography in bio-tribocorrosion*. Woodhead Publishing Limited, 2013.

[92] Y. Holovenko, M. Antonov, L. Kollo, and I. Hussainova, "Friction studies of metal surfaces with various 3D printed patterns tested in dry sliding conditions," *Proc. Inst. Mech. Eng. Part J J. Eng. Tribol.*, vol. 232, no. 1, pp. 43–53, 2018.

[93] E. Rabinowicz, *Friction and Wear of Materials*. 1995.

[94] W. Haws, "ASM Handbook Editorial Assistance," no. 423882, 2017.

[95] M. Elements, *Friction and Wear Phenomena in Steels at Elevated Temperatures*. .

[96] Y. Sun, A. Moroz, and K. Alrbaey, "Sliding wear characteristics and corrosion behaviour of selective laser melted 316L stainless steel," *J. Mater. Eng. Perform.*, vol. 23, no. 2, pp. 518–526, 2014.

[97] F. Bartolomeu *et al.*, "316L stainless steel mechanical and tribological behavior—A comparison between selective laser melting, hot pressing and conventional casting," *Addit. Manuf.*, vol. 16, pp. 81–89, 2017.

[98] A. Mertens, S. Reginster, Q. Contrepois, T. Dormal, O. Lemaire, and J. Lecomte-Beckers, "Microstructures and mechanical properties of stainless steel AISI 316L processed by selective laser melting," *Mater. Sci. Forum*, vol. 783–786, pp. 898–903, 2014.

[99] G. Miranda *et al.*, "Predictive models for physical and mechanical properties of 316L stainless steel produced by selective laser melting," *Mater. Sci. Eng. A*, vol. 657, pp. 43–56, 2016.

[100] H. Li, M. Ramezani, M. Li, C. Ma, and J. Wang, “Tribological performance of selective laser melted 316L stainless steel,” *Tribol. Int.*, vol. 128, no. July, pp. 121–129, 2018.

[101] EOS, “Eosint M 280,” *Web page*, pp. 1–3, 2014.

[102] Bruker, “ContourGT-K 3D Optical Microscope,” 2013.

[103] Bruker, “UMT TriboLab Mechanical Tester and Tribometer,” *Datasheet*, 2015.

[104] B. Vrancken, L. Thijs, J. P. Kruth, and J. Van Humbeeck, “Heat treatment of Ti6Al4V produced by Selective Laser Melting: Microstructure and mechanical properties,” *J. Alloys Compd.*, vol. 541, no. 0, pp. 177–185, 2012.

[105] Peen Rawn, “3D Printing of 316L Stainless Steel and Its Effect on Microstructure and Mechanical Properties,” 2017.

[106] D. Mahmoud and M. A. Elbestawi, “Selective laser melting of porosity graded lattice structures for bone implants,” *Int. J. Adv. Manuf. Technol.*, vol. 100, no. 9–12, pp. 2915–2927, 2019.

[107] G. Gagg, E. Ghassemieh, and F. E. Wiria, “Effects of sintering temperature on morphology and mechanical characteristics of 3D printed porous titanium used as dental implant,” *Mater. Sci. Eng. C. Mater. Biol. Appl.*, vol. 33, no. 7, p. 3858—3864, Oct. 2013.

[108] J. Banhart, “Manufacture, characterisation and application of cellular metals and metal foams,” *Prog. Mater. Sci.*, vol. 46, no. 6, pp. 559–632, Jan. 2001.

[109] M. Ghasri-Khouzani *et al.*, “Direct metal laser-sintered stainless steel: comparison of microstructure and hardness between different planes,” *Int. J. Adv. Manuf. Technol.*, vol. 95, no. 9–12, pp. 4031–4037, 2018.

[110] K. Saeidi, X. Gao, Y. Zhong, and Z. J. Shen, “Hardened austenite steel with columnar sub-grain structure formed by laser melting,” *Mater. Sci. Eng. A*, vol. 625, pp. 221–229, 2015.

[111] R. J. Hebert, “Viewpoint: metallurgical aspects of powder bed metal additive manufacturing,” *J. Mater. Sci.*, vol. 51, no. 3, pp. 1165–1175, Feb. 2016.

[112] L. J. O. Donnell, “Tribology of 316L Austenitic Stainless Steel,” *Wear*, no. January, 2010.

[113] P. J. Blau, *Friction science and technology: From concepts to applications, second edition*. 2008.

RESEARCH CONTRIBUTIONS

Publications

1. A.Eliasu, S. Boakye-Yiadom, A. Czekanski (2019), Effect of Direct Metal Laser Sintering (DMLS) Parameters on the Microstructural Evolution and Mechanical Properties of 316L Stainless Steel, Journal of Manufacturing Processes-(Under review as of Nov 2019).

2. A.Eliasu, S. Hanson Duntu, S. Boakye-Yiadom, A. Czekanski (2019) Effect of Direct Metal Laser Sintering (DMLS) Parameters on Wear behavior of 316L Stainless Steel, Journal of Manufacturing Processes-(Under preparation as of Dec 2019).

Conference Proceedings

1. A.Eliasu, S. Boakye-Yiadom, A. Czekanski (2019) Effect of 3D Printing Parameters on Porosity and Microhardness of AISI 316L Fabricated by DMLS, 31st Canadian Materials Science Conference, Vancouver, Canada.

2. A.Eliasu, S. Boakye-Yiadom, A. Czekanski (2019) Effect of Printing Parameters on Porosity of DMLS AISI 316L Alloy, Canadian Society of Mechanical Engineering, London, Ontario Canada.

3 A.Eliasu, S. Boakye-Yiadom (2019) Effect of High-Temperature Impact on the Formation of Adiabatic Shear Bands, Microscopy and Microanalysis Portland, Oregon, USA.

8 APPENDIX A- Coefficient of friction

A1 COF vs time for sample G1B2 for 20s

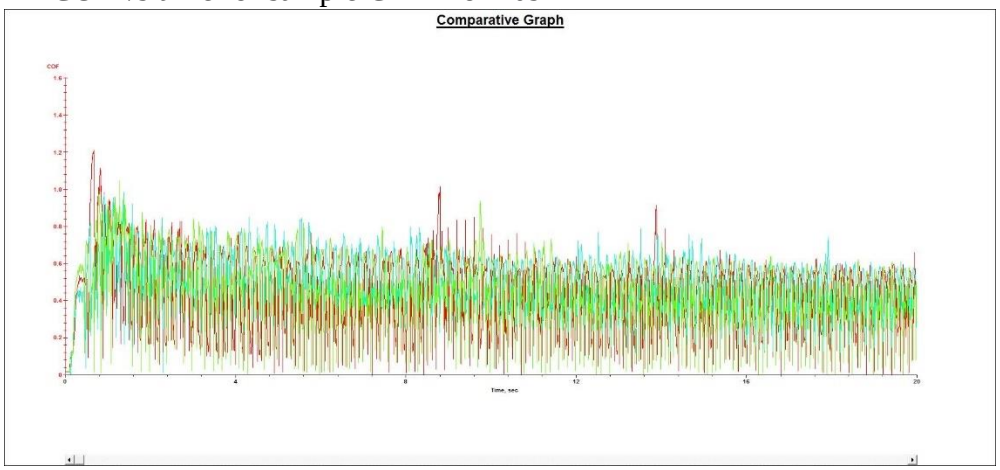

A2 COF vs time for sample G1C2 for 20s

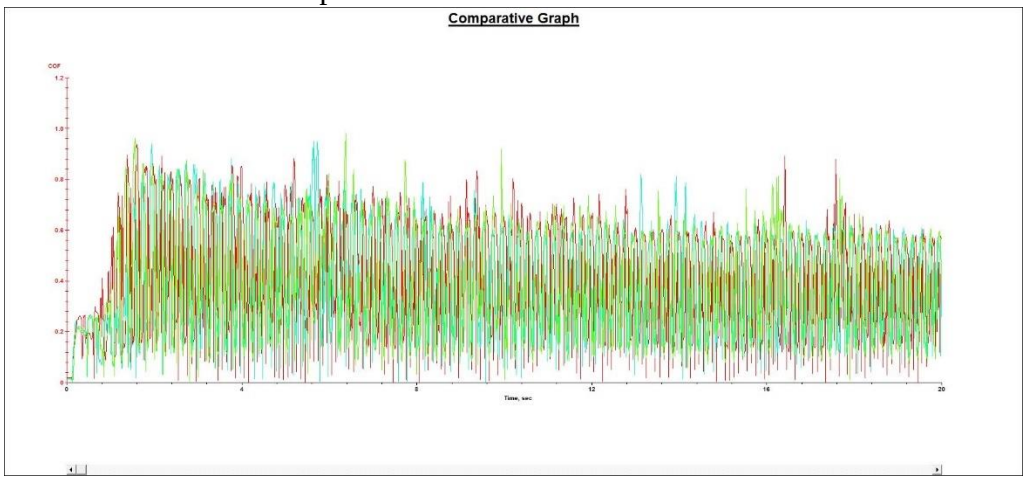

A3 COF vs time for sample G1C3 for 20s

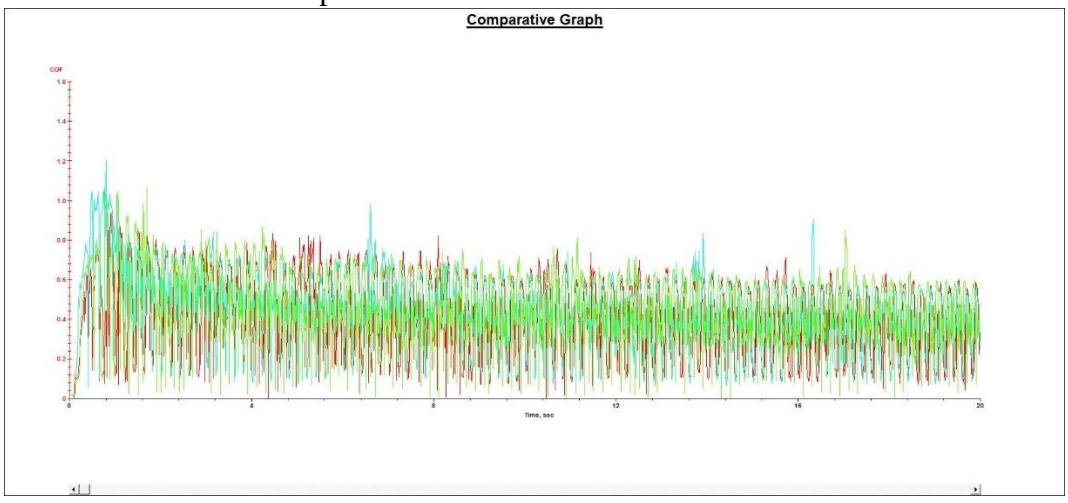

A4 COF vs time for sample G2B1 for 20s

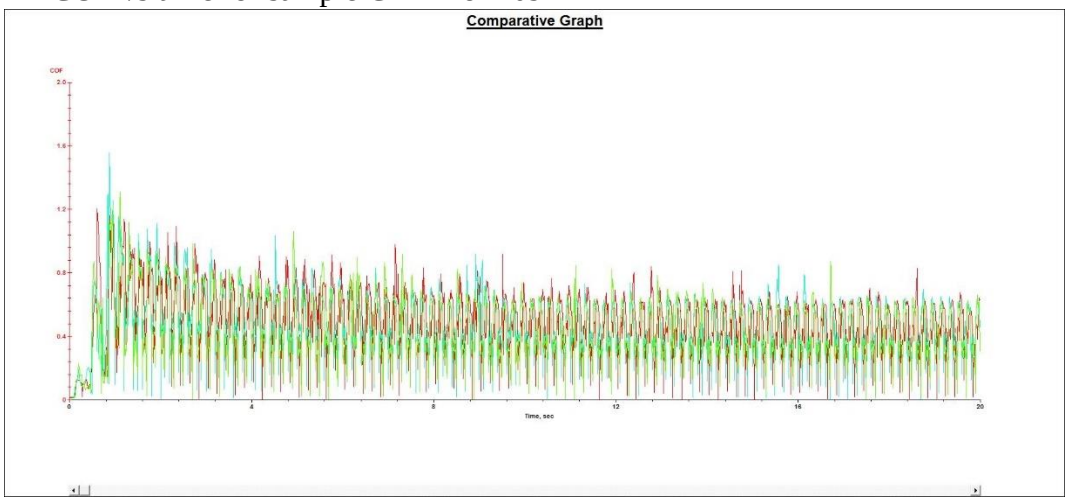

A5 COF vs time for sample G2B2 for 20s

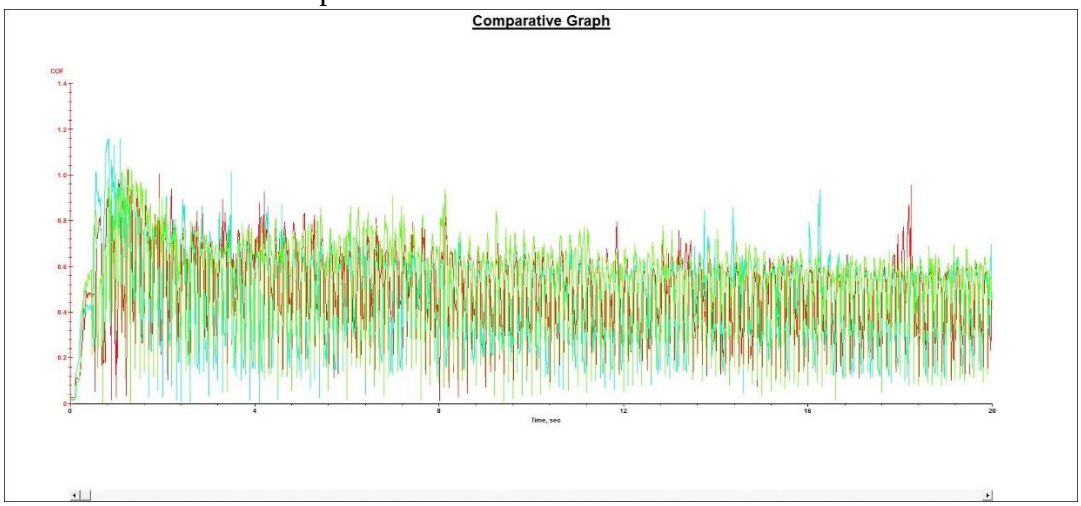

A6 COF vs time for sample G3C2 for 20s

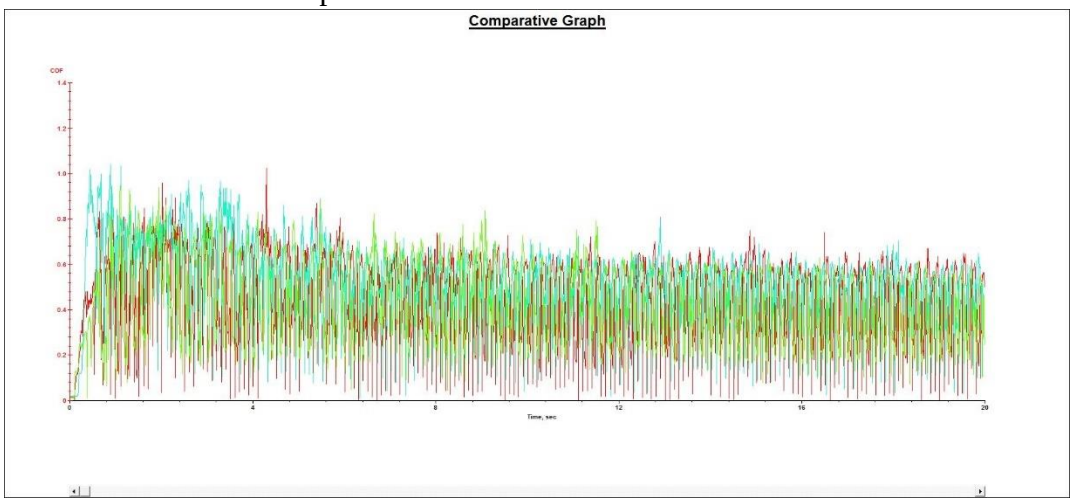

A7 COF vs time for sample G4B2 for 20s

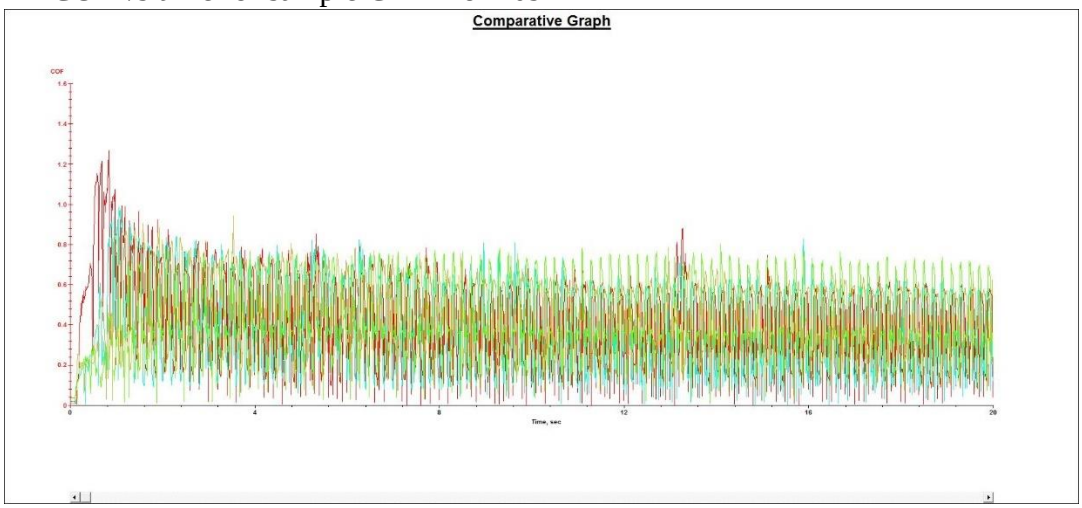

A8 COF vs time for sample G4B3 for 20s

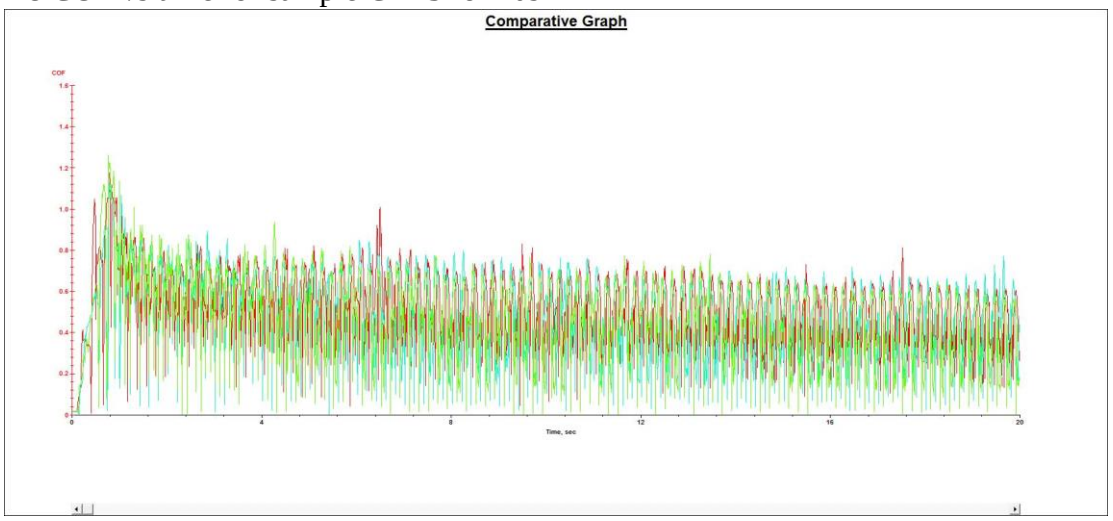

9 APPENDIX B- Raw data

B1-Wear Test

	Before wear				After wear				
sample	track 1	track 2	track 3	average mass	track 1	track 2	track 3	average	Mass loss
G3C2	24.3853	24.3852	24.3852	24.3852	24.3818	24.3820	24.3817	24.3818	0.0034
	24.3813	24.3820	24.3817	24.3817	24.3787	24.3786	24.3788	24.3787	0.0030
	24.3784	24.3782	24.3782	24.3783	24.3743	24.3743	24.3745	24.3744	0.0039
									0.0034
G1B2	26.4955	26.4955	26.4954	26.4955	26.4920	26.4921	26.4923	26.4921	0.0033
	26.4920	26.4921	26.4923	26.4921	26.4885	26.4885	26.4887	26.4886	0.0036
	26.4885	26.4885	26.4887	26.4886	26.4848	26.4848	26.4848	26.4848	0.0038
									0.0036
G4B3	24.9033	24.9030	24.9031	24.9031	24.9005	24.9004	24.9006	24.9005	0.0026
	24.9005	24.9004	24.9006	24.9005	24.8980	24.8983	24.8982	24.8982	0.0023
	24.8980	24.8983	24.8982	24.8982	24.8950	24.8950	24.8950	24.8950	0.0032
									0.0027
G1C3	24.9319	24.9321	24.9323	24.9321	24.9293	24.9291	24.9290	24.9291	0.0030
	24.9293	24.9291	24.9290	24.9291	24.9255	24.9256	24.9255	24.9255	0.0036
	24.9260	24.9232	24.9261	24.9251	24.9223	24.9224	24.9223	24.9223	0.0028
									0.0031
G2B2	25.9403	25.9402	25.9402	25.9402	25.9369	25.9368	25.9366	25.9368	0.0035
	25.9369	25.9368	25.9366	25.9368	25.9326	25.9328	25.9329	25.9328	0.0040
	25.9326	25.9328	25.9329	25.9328	25.9300	25.9297	25.9300	25.9299	0.0029
									0.0034
G4B2	24.5800	24.5801	24.5799	24.5800	24.5773	24.5772	24.5773	24.5773	0.0027
	24.5773	24.5772	24.5773	24.5773	24.5714	24.5717	24.5716	24.5716	0.0057
	24.5715	24.5716	24.5717	24.5716	24.5685	24.5687	24.5688	24.5687	0.0029
									0.0042
G1C2	24.6135	24.6131	24.6133	24.6133	24.6105	24.6105	24.6106	24.6105	0.0028
	24.6105	24.6105	24.6106	24.6105	24.6075	24.6075	24.6075	24.6075	0.0030
	24.6075	24.6075	24.6075	24.6075	24.6046	24.6046	24.6045	24.6046	0.0029
									0.0029
G2B1	30.2838	30.2839	30.2838	30.2838	30.2796	30.2798	30.2800	30.2798	0.0040
	30.2796	30.2798	30.2800	30.2798	30.2763	30.2762	30.2762	30.2762	0.0036
	30.2763	30.2762	30.2762	30.2762	30.2719	30.2719	30.2719	30.2719	0.0043
									0.0040

10 APPENDIX C-Chemical Analysis

C 1- EDS of Sample G2B1 showing the presence of SiO_2 precipitates

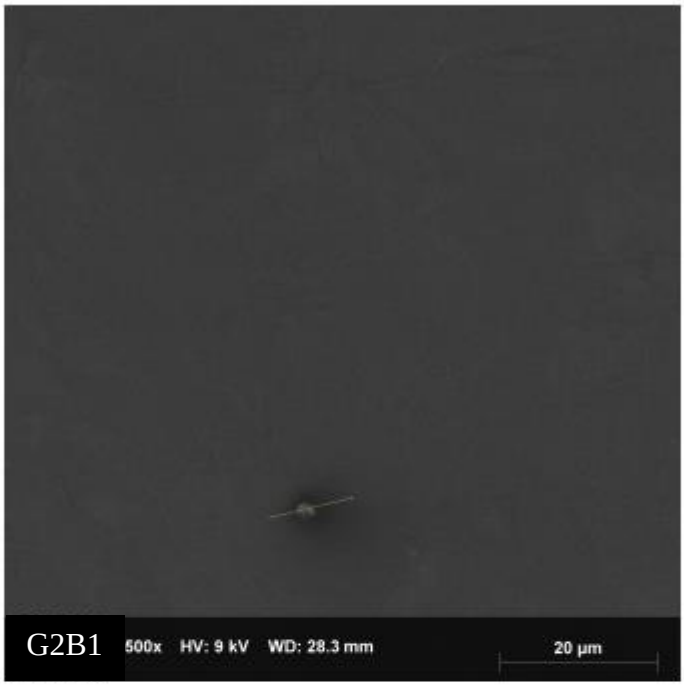

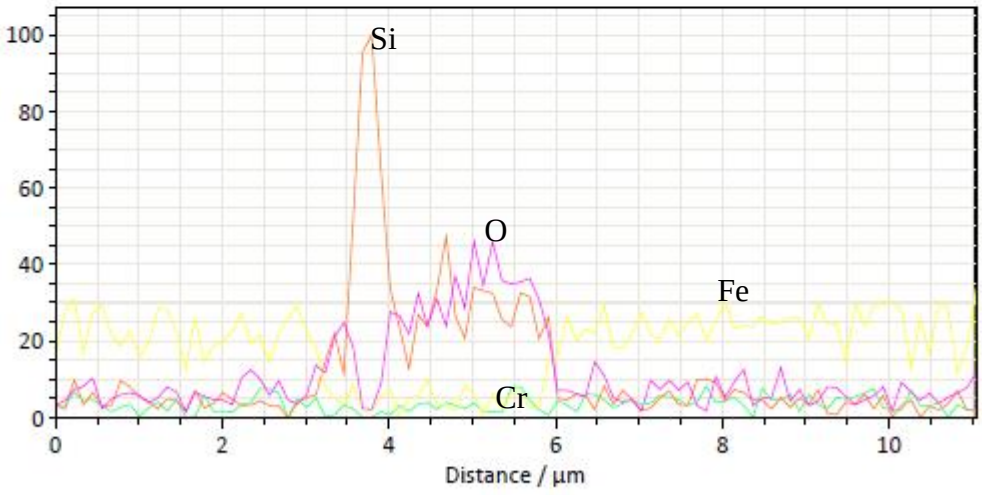

11 APPENDIX D- Scan Pattern

D1-Stripe Scan Pattern as portrayed by Yakout et al [52]